Chemical Reactions of Planetary Materials Under Extreme Redox Conditions

by

Harrison Allen-Sutter

A Dissertation Presented in Partial Fulfillment
of the Requirements for the Degree
Doctor of Philosophy

Approved May 2022 by the
Graduate Supervisory Committee:

Sang-Heon Shim, Chair
James Tyburczy
Kurt Leinenweber
Travis S.J. Gabriel
Mingming Li

ARIZONA STATE UNIVERSITY

August 2022

ABSTRACT

Hydrogen is the main constituent of stars, and thus dominates the protoplanetary disc from which planets are born. Many planets may at some point in their growth have a high-pressure interface between refractory planetary materials and a hydrogen-dominated atmosphere. However, little experimental data for these materials at the relevant pressure-temperature conditions exists. I have experimentally explored the interactions between planetary materials and hydrogen at high P-T conditions utilizing the pulsed laser-heated diamond-anvil cell.

First, I found that ferric/ferrous iron (as Fe_2O_3 hematite and $(Mg,Fe)O$ ferropericlase) are reduced to metal by hydrogen: $Fe_2O_3 + 4H_2 \rightarrow 2FeO + H_2O + 3H_2 \rightarrow 2FeH + 3H_2O$ and $\left(Mg_{1-x}Fe_x\right)O + \frac{3}{2}xH_2 \rightarrow xFeH + (1-x)MgO + xH_2O$ respectively. This reduction of iron by hydrogen is important because it produces iron metal and water from iron oxide. This can partition H into the core (as FeH) or mantle (as H_2O/OH^-) of a growing planet.

Next, I expanded my starting materials to silicates. I conducted experiments on San Carlos Olivine at pressures of 5-42 GPa. In the presence hydrogen, I observed the breakdown of molten magnesium silicate and the reduction of both iron and silicon to metal, forming alloys of both Fe-H and Fe-Si: $Mg_2SiO_4 + 2H_2 + 3Fe \rightarrow 2MgO + FeSi + 2FeH + 2H_2O$.

Similar experiments using natural fayalite (Fe_2SiO_4) as a starting material at pressures of 5-21 GPa yielded similar results. Hydrogen reduced iron to metal as it did in experiments with iron oxides. Unlike with San Carlos olivine, above 10 GPa silicon remained oxidized, implying the following reaction: $Fe_2SiO_4 + 3H_2 \rightarrow 2FeH + 2H_2O + SiO_2$. However, below 7 GPa, silicon reduces and alloys with iron. The formation of Fe-Si alloys from silicates facilitated by hydrogen could have important effects for core composition in growing planets. I also observed at low pressures (<10

GPa), quenched iron melt can trap more hydrogen than previously thought (H/Fe nearly 2 instead of 1). This may have important effects for the chemical sequestration of a hydrogen atmosphere at shallow depths in an early magma ocean.

All of the experimental work presented herein show that the composition, chemical partitioning, and phase stability of the condensed portion of growing planets can be modified via interaction with overlaying or ingassed volatile species.

ACKNOWLEDGEMENTS

TABLE OF CONTENTS

iv

LIST OF TABLES

LIST OF FIGURES

Chapter 1

INTRODUCTION

Since the earliest recorded human history, humans have gazed at the sky above wondering what exists beyond the Earth. By tracking the movements of "stars" ancient astronomers discovered some bodies did not move with the rest of the sky. In 1543, Copernicus proposed the heliocentric model of the solar system (Copernicus, 1543) paving the road for the Scientific Revolution (Valdez, 2014) and more specifically, planetary science. Over the coming centuries many discoveries were made revealing that that far off planets in our solar system may not be so different from our home world. Over the coming centuries extraterrestrial moons (Galilei, 1610), ice caps (Miraldi, 1719), and water channels (Schiaparelli, 1878; Lowell, 1895) sparked the imagination of generations as to what makes Earth habitable and where else in our solar system and beyond life may exist.

To answer the question of what makes a planet habitable, scientists looked to the one planet we know with absolute certainty is: Earth. While it is superficial properties such as atmospheric composition and availability of liquid water that allow life to thrive, these properties are intrinsically linked to both the interior and formation history (Lammer *et al.*, 2009). The obvious challenge when studying the structure, composition, dynamics, and material properties of the deep interior of Earth or other planets is that we cannot go there. Therefore, scientists must use other methods such as indirect measurement via seismic waves which travel through the interior (Gilbert and Dziewonski, 1975; Dziewonski and Anderson, 1981), computational methods/simulations (McKenzie *et al.*, 1974), or recreating the conditions of planetary interiors in the lab where direct measurements are possible (Jamieson *et al.*,

1959; Van Valkenburg, 1962; Jayaraman, 1983). Seismology can tell you the speed of waves through the material and density of different structures within the planet. The composition the interior can be inferred from a number of lines of evidence. Firstly, volcanic eruptions (or other dynamic processes) bring to the surface mantle material which we can directly study. Secondly, meteorites represent the primitive building blocks of planets so one can infer the bulk composition of planets to be a combination of different types of meteorite (e.g. Ringwood, 1977). Lastly, mineral physics experiments in a laboratory can explore the material properties of different planetary materials and align those properties to the observed properties of the planet. This last method is the tool I use to explore the interiors of planets.

Seismological observations have shown that the Earth has a layered structure consisting of a metallic core, silicate mantle, and crust (as is also likely the case for most rocky planets) (Oldham, 1906; Lehmann, 1936; Dziewonski and Anderson, 1981). Earth's core is composed predominately of metallic iron alloyed with about 6% nickel based on meteoritic abundances (Birch, 1952; Ringwood, 1977). However, the density of Earth's outer core exhibits a deficit ($\sim$10%) compared to pure iron (Birch, 1964; Jeanloz, 1979; Mao et $al.$, 1990) which suggests additional light elements. Many candidates have been explored over the years such as sulphur, oxygen, silicon, carbon, and hydrogen (Brett, 1976; Poirier, 1994; Hirose et $al.$, 2021). Hydrogen is the most abundant element in the universe, the main constituent of gas giant planets, and omnipresent in protoplanetary disks. However, after Kronig et $al.$ (1946) suggested hydrogen as a light element candidate for the Earth's core, it was not favored as a probable candidate for many years (Ringwood, 1966). The argument was that by the time terrestrial planetary embryos had grown to significant size — tens of Myrs (Lissauer, 1987) — the gas disk had dissipated (Lissauer, 1993; Haisch Jr et $al.$, 2001) preventing molecular H from being a major player in terrstrial planetary cores.

However, since high-pressure studies have demonstrated large hydrogen solubility in iron at the elevated pressures more relevant to core formation (Badding *et al.*, 1991; Yagi and Hishinuma, 1995; Pépin *et al.*, 2014; Umemoto and Hirose, 2015) and studies have shown the highly siderophilic nature of hydrogen (Okuchi, 1997; Li *et al.*, 2020b; Tagawa *et al.*, 2021), hydrogen has gained traction as a strong candidate to at least partially explain the density deficit in Earth's outer core (Hirose *et al.*, 2021). Additionally, in the new paradigm of "pebble accretion" (Lambrechts and Johansen, 2012), planets can grow much faster (and thus hotter) allowing for significant ingassing of nebular H into magma oceans (Olson and Sharp, 2018).

Isotopic measurements of deep hydrogen reservoirs have shown a distinctly lighter D/H signature than the roughly chondritic proportions of Earth's surficial oceans, implying they were sequestered from the proto-solar nebula or a hydrogen-rich primary atmosphere (Genda and Ikoma, 2008; Hallis *et al.*, 2015; Wu *et al.*, 2018). Other studies have found evidence for the capture of nebular gas in noble gas isotopes (e.g. Williams and Mukhopadhyay, 2019). Experimental studies at lower pressures have found high solubility of hydrogen in silicate melts as H_2 and H_2O (Hirschmann *et al.*, 2012). Theoretical studies have also found that magma oceans on young terrestrial planets could ingas large amounts of hydrogen via dissolution (Olson and Sharp, 2018). In the event where large amounts of hydrogen are ingassed into a rapidly convecting magma ocean of a young planet undergoing differentiation, it is important to understand the impact that hydrogen could have on the evolution of the young planet. Of particular importance is the relationship between H_2 and H_2O and stability of the relevant minerals in the presence of said volatiles.

These relations are not only important on Earth, but also on other planets. Since the development of (mostly) reliable rockets, humans have sent scientific missions to all 8 planets in our solar system (as well as Pluto, comets, and asteroids!). The

terrestrial planets in our solar system are thought to have formed simultaneously via the same process (Morbidelli *et al.*, 2012), and thus relations explored in this work may apply to their formation, evolution, and structure in a similar manner to the ways discussed above for Earth. Beyond the terrestrial planets in the outer solar system lay the ice and gas giants.

With the discovery of the first exoplanet (planet orbiting a star other than our Sun) in 1992 (Wolszczan and Frail, 1992), a new era of planetary science began. Whereas for planets in our solar system, we can directly measure properties such as density structure (via gravitational moments and seismology), composition (via remote spectroscopy and sample collection), and other measurements made possible by being able to physically go to (or near) the planet, no such measurements are possible for exoplanets many light-years away. The only properties we can measure are mass (via the radial-velocity/Doppler spectroscopy method), radius (via the transit method), and *sometimes* rough atmospheric composition and/or elemental abundances of the host star. In the three decades since the discovery of the first exoplanet, we have found over 5,000 more (NASA Exoplanet Archive, 2019). This has allowed planetary scientists to answer new questions such as the following:

1. How typical or special is our planetary system?

2. How common is it for stars to have planets at all?

3. How common are "Earth-like" Planets?

4. What other types of planets exist in our galactic neighborhood?

The last point is of particular importance because we have discovered a huge variety in the types of planets, many of which have no direct analogues in our solar system. Planets are typically made of some combination of a metal core, overlain by a rocky

mantle, overlain by solid/liquid volatiles, overlain by a gaseous atmosphere. In our solar system, we have terrestrial planets (like Earth), gas giants (like Saturn and Jupiter), and ice giants (like Uranus and Neptune). Each type of planet has different relative amounts of each layer. Terrestrial planets are dominated by rock and metal and range in size from$\sim$0.055–1 $+M_\oplus$. Gas giants are dominated by H and ice giants by other H-bearing volatile species (i.e. H_2O, CH_4, NH_3...etc). Beyond our solar system, the distribution of planets defies such simple classification.

We cannot simply measure the composition of exoplanets because we cannot go there. However, we can use density as a proxy for composition. Different minerals have different densities, and thus we can make models about the composition of a planet from its bulk density. Figure 1.1 shows the density (or mass and radius, the ratio of which is density) of exoplanets compared to what their density would be if they were made entirely of metal (Fe), rock ($MgSiO_3$), or water (H_2O). As you may notice, many large planets are much less dense than any of the plotted density curves; these are gas giants like Jupiter or Saturn. More importantly, one should note the large number of planets for which there are no analogues. The two most common types of exoplanets we have observed are super-Earths–planets with a radius of $\sim$1.5–2 time that of Earth, thought to be compositionally and structurally similar to Earth–and sub-Neptunes–planets with a radius of 2.7–3 times that of the Earth thought to have rock/metal cores overlain by a thick H-dominated atmosphere. To understand the formation and structure of these planets, planetary scientists must turn to computer models. In order to accurately model the formation and evolution of planets, models need experimental data on the chemical partitioning, phase relations, and equations of state of various planet forming materials.

Given the fact that all planets are born in a H-rich disk, and many retain a H-rich atmosphere/envelope, it is clear the interactions between H and other planetary ma-

Figure 1.1: Mass - radius distribution of confirmed exoplanets compared to the density of various planet-forming materials.

terials is important for the modeling of planetary processes. Despite its importance, the role of hydrogen (as opposed to H_2O or OH^-) in planetary formation processes is largely understudied in experiments due to difficulties working with hydrogen at high-pressure (Section 2.3; Deemyad *et al.*, 2005). In this work, I aim to address this problem.

The following are key questions I hope to address through this work:

- How does H affect the stability of major rocky mineral phases at the high P-T conditions of the deep interior?

- How does H affect the elemental partitioning/phase relations in a planet undergoing differentiation?

- What reactions drive the exchange of H and O at the high pressure interface between a H envelope and rocky magma ocean in sub-Neptunes or other growing planets with a magma ocean overlain by a H-dominated atmosphere?

- In what high-pressure phases can H be sequestered and stabilized in the interiors of planets?

Chapter 2

METHODOLOGY

2.1 Phase Identification

2.1.1 Synchrotron X-RAY DIFFRACTION
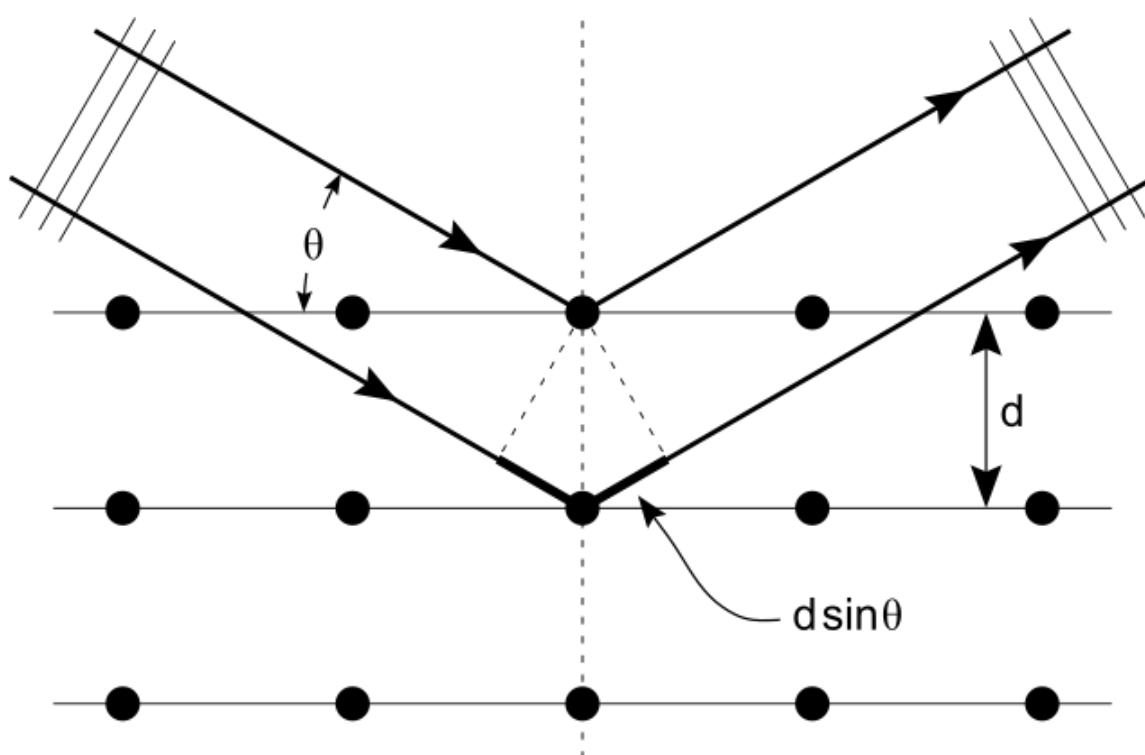
Figure 2.1: Schematic diagram showing the Bragg condition for constructive interference in a crystal lattice with plane spacing d (Hydrargyrum, 2011).

X-ray diffraction (XRD) is the primary technique I use to identify crystalline phases at high-pressure. This is achieved, because as the synchrotron X-ray beams pass through the sample they are scattered by the atoms in the sample. This scattering is spherical in nature and on its own would not carry information about the structure in which the atom that scattered it resides. However, due to the repeating

nature of crystalline structures, the sum of the scattered spherical waves of light cause constructive and destructive interference. The scattering angles at which constructive interference is achieved can be related to the spacing between planes of atoms in the crystal by a simple mathematical relation called Bragg's Law (Bragg and Bragg, 1913):

$$2d \sin \theta = n\lambda \tag{2.1}$$

where d is the spacing between crystalligraphic planes, θ is the diffraction angle relative to the lattice plane, n is an integer (1, 2, 3...), and λ is the wavelength of the incident X-ray. In my experiments, λ is known and θ is measured, meaning I can use this technique to determine the d-spacing. If one knows the spacing between enough planes in a crystal, then one can know the crystal symmetry and unit cell volume. This can be compared to the volumes and symmetry of known materials for phase identification.

2.1.2 Spectroscopic Techniques

While XRD is a powerful tool for the determination and refinement of crystal structures, it is not the only tool in the materials characterization tool belt. The electromagnetic radiation in XRD is monochromatic and scattered elastically, a technique that only gives you information about the positions of atoms (and the volume of said atoms). It does not give information about what element those atoms are or how they are bonded. It also does not detect amorphous or trace elements. These shortcomings can be addressed with complementary spectroscopic techniques.

One technique which I have used extensively throughout this work is Raman Spectroscopy. With Raman spectroscopy, an incident light source (in my case a green 532 nm laser) illuminates the sample. This monochromatic light (photons) interacts with bonded molecular vibrations (phonons), causing them to be scattered inelasti-
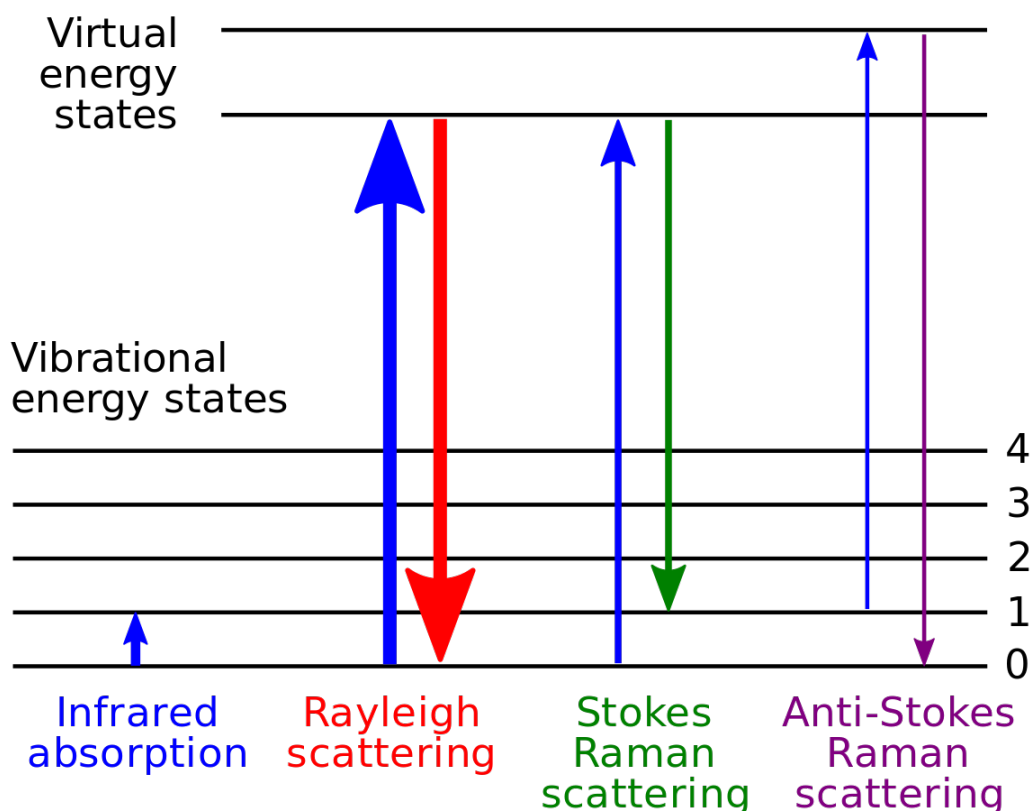
Figure 2.2: Visualization of the phonon energy transitions in Raman Spectroscopy (Moxfyre, 2009). The incident electromagnetic radiation that drives these transitions gain or lose energy equal to the difference in the energy states of the phonons resulting in a wavelength shift.

cally (with a different energy than they started with, as shown in figure 2.2). These energy shifts can be measured with a spectrometer and are diagnostic of different types of bonding vibrational modes. In this work I primarily used Raman spectroscopy to detect vibrational modes of H_2 and OH. These are important volatile species and can be present both as their own phase in the sample medium and bound in the crystalline structure of other phases but may not be seen in XRD due to small X-ray cross-sections, low concentrations, or peak overlap with more strongly scattering materials like Fe metal.

Another spectroscopy technique that complements the abilities of both Raman
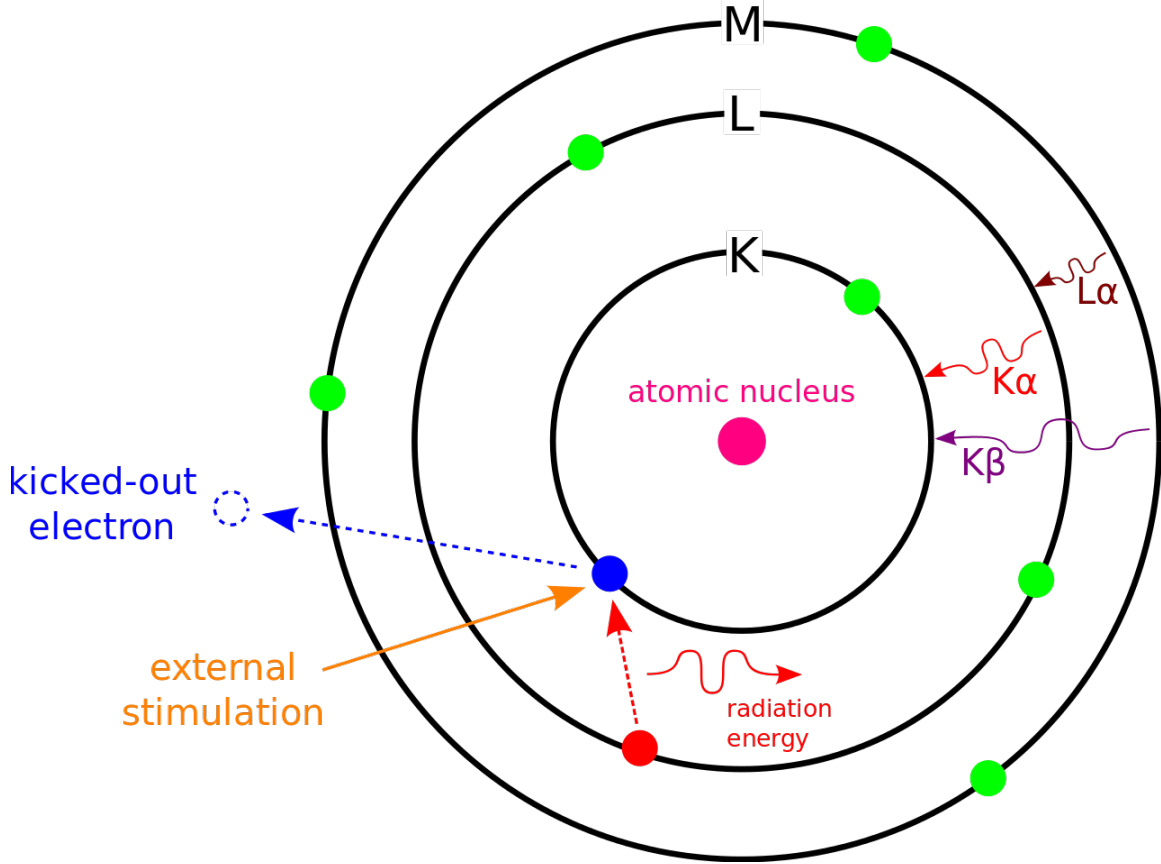
Figure 2.3: Schematic showing the operating principle of EDS (Muso, 2007). External stimulation (an electron beam) kicks out an electron, and as higher-energy electrons fall to lower energies to replace it, they emit photons of a charictaristic wavelength (Kα, Kβ, Lα...).

spectroscopy and XRD is X-ray spectroscopy (EDS - energy dispersive spectroscopy). I have used EDS on recovered samples to map the distribution of elements in the sample. This is useful because unlike the previously mentioned methods that measure structural properties (crystal structure, bonding vibrations...), EDS measures actual chemical composition directly. It does this by bombarding the sample with electrons which knocks core electrons in the atoms out. As electrons transition from higher-energy orbits to lower-energy ones, they release photons (Fig. 2.3). These photons are diagnostic of various elements and allow chemical mapping of the distribution of elements in the recovered sample (e.g., Fig. 2.8). One drawback of this technique is that

it cannot be performed *in-situ*. Whilst Raman and XRD both rely on illumination of the sample with electromagnetic radiation (which the diamonds are transparent to, thus allowing characterization while under pressure in the diamond-anvil cell), EDS requires bombardment with an electron beam (which cannot penetrate the diamonds).

2.2   LASER-HEATED DIAMOND-ANVIL CELL (LHDAC)

The laser-heated diamond-anvil cell (or LHDAC/DAC) is the main tool I use to generate the high pressure-temperature (P-T) conditions relevant to planetary interiors. Pressure is defined as force per unit area. In order to achieve higher pressures you either need higher force or smaller area. The basic principle behind the DAC is to make as small an area as possible and then maximize the force across that area. This is done using diamonds because they are the strongest material humans have access to. It is a fairly simple device with two halves: a piston and a cylinder, each with a centered diamond (Fig. 2.4. These two halves are brought together so the tips of the diamonds come together with a sample between. These are then squeezed together using screws and can generate pressure beyond that at the core of the Earth.

Because diamonds are optically transparent, X-rays (for XRD) and near-IR lasers (for laser heating) can be co-axially aligned and shone onto the sample material through the diamonds, enabling XRD measurements of materials at simultaneous high pressure and high temperature. This is important because it allows the study of materials at the same P-T conditions they experience deep in planetary interiors.
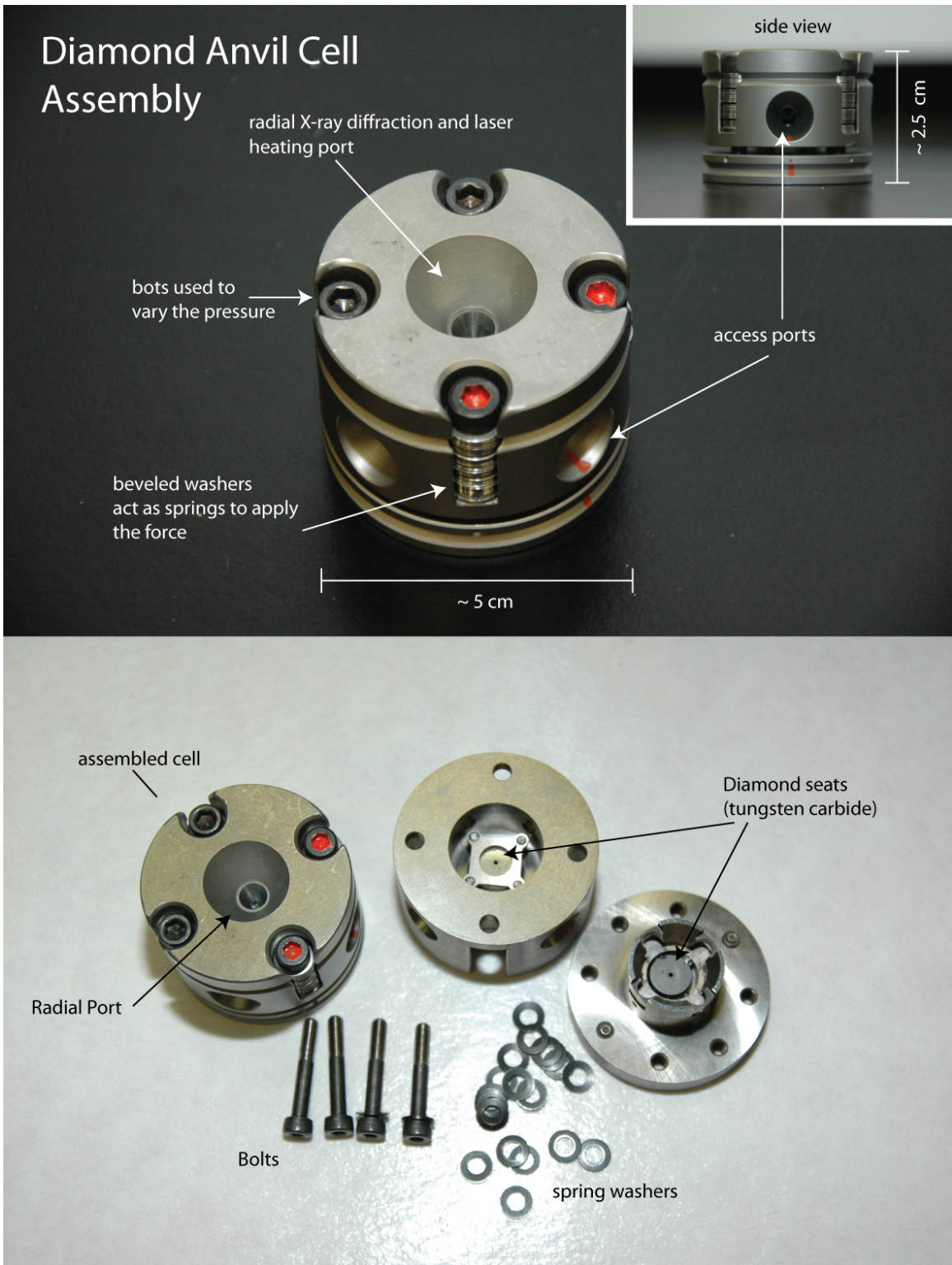
Figure 2.4: Annotated image of a DAC showing its components and assembly
Source: Lavina and Burnley, UNLV
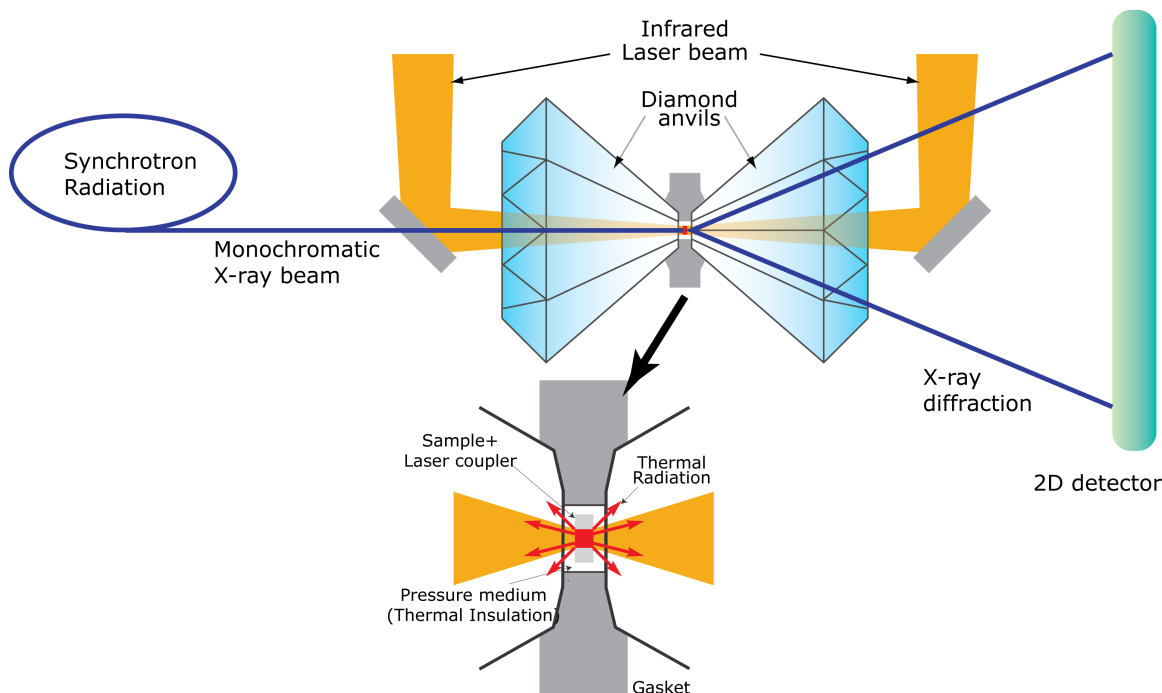
Figure 2.5: Diagram showing the basic setup of a synchrotron XRD experiment in the LHDAC. Image Credit: Sang-Heon Dan Shim, ASU.

2.3 Challenges and Techniques Working with Hydrogen in the LHDAC

2.3.1 Loading Pure Hydrogen in the Diamond Anvil Cell

Throughout this section, one recurring theme will appear: Hydrogen is difficult to work with because it is extremely reactive and extremely mobile. When loading hydrogen in a diamond-anvil cell these core problems crop up in a number of ways. First and foremost, hydrogen is difficult to contain and capture. In order to capture enough hydrogen to hydrostatically balance the inward pressure from the compressed rhenium gasket at high-pressure, hydrogen must be loaded into the cell at a pressure exceeding 1000 bar. To safely contain hydrogen at such pressures during loading (beyond the experimental challenges associated with H, it can also be explosive when mixed with atmospheric oxygen), I utilized a Sanchez GLS 1500 (Fig. 2.6). This device works by filling an enclosed chamber (the "bomb") with pressurized hydrogen

14

($\sim$110-150 bar), and then decreasing the volume of the enclosed chamber until the pressure reaches the loading pressure of 1000-1500 bar. Once at the loading pressure, an external motor is engaged mechanically, closing the cell via its standard screw tightening (Fig. 2.4). The fact that not only the sample, but the whole DAC is exposed to up to 1500 bar of H also poses additional challenges. The clay typically used to mount the gasket on the anvils reacts with H and can contaminate the sample loading. To combat this, I use a different kind of clay (wall mounting putty). Additionally, the stainless steel the DAC itself is made of can interact with the H gas. At ambient pressure, H can penetrate the structure of steel altering its material properties (Marchi and Somerday, 2007). In our case, the tight precise fit between the piston and cylinder of the diamond-anvil cell can be disrupted by the H infiltration, preventing the cell from closing under H pressure in the gas loading system. To combat this, I used only very loosely fitting cells, however the looseness of the fit also has the trade-off of lower mechanical stability under stress when conducting experiments, which can sometimes lead to alignment issues.

2.3.2 Laser-Heating Experiments

Once the sample has been loaded, the challenges of working with hydrogen do not end. Its extreme mobility and reactivity are exacerbated at the high temperatures associated with laser heating in the diamond-anvil cell. When heated, the H-medium melts (at the P-T conditions explored in my experiments, see Figs. 3.1, 4.1, and 5.1). This hot dense fluid hydrogen readily diffuses into the diamond anvils, causing embrittlement and eventually failure (Fig. 2.7).

To mitigate this issue, instead of traditional continuous wave (CW) heating, I utilized the pulsed laser-heating system at beamline 13-IDD (Deemyad *et al.*, 2005; Goncharov *et al.*, 2010). While with pulsed heating the medium still melts and H

Figure 2.6: Sanchez GLS 1500 system I utilized for loading pure H_2 gas in diamond anvil cells. Image from corelab/sanchez technologies.

still diffuses into the anvils, which can sometimes still lead to anvil failure, the short timescale of each heating pulse mitigates the effect allowing me to successfully perform experiments exploring the interactions between planetary materials and pure H at high P-T conditions. Although limiting the total heating time may present kinetic issues in some chemical systems whereby not enough time is spent at high-temperature for a chemical reaction to reach equilibrium, H is so reactive that this is not a major issue in my research. In some cases chemical reactions fully complete in as little as one heating event (such "fast" reactions will be presented in later chapters).

In addition to diffusion into the diamond anvils, H also has a propensity to diffuse into the rhenium gaskets, again leading to embrittlement and failure. To mitigate this, I coat my gaskets in $\sim$800 nm of gold prior to sample loading (Pépin *et al.*, 2014). The gold layer is (relatively) inert in the presence of hydrogen (although gold hydride is
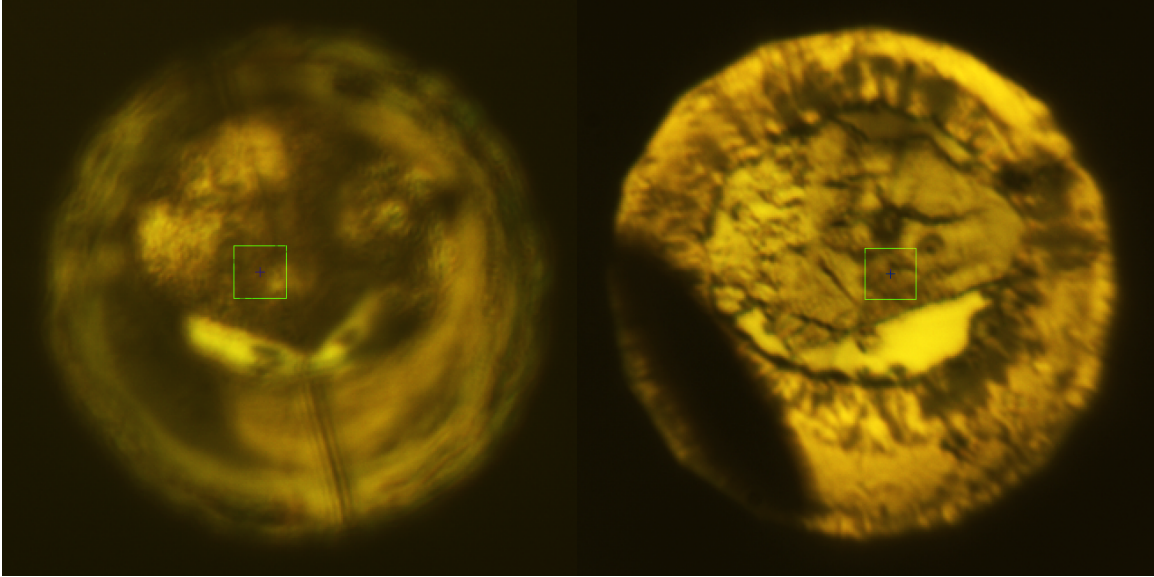
Figure 2.7: Two examples of failing anvils from experiments in chapter 3. On the left a planar fracture parallel to the optical axis can be seen splitting the anvil in half. On the right another planar fracture can be seen at an angle to the optical axis creating a dark shaded region were light internally reflects from the sample away from the camera along the fracture plane. In both cases high P-T data collection was successful but the diamonds failed and the sample was lost prior to decompression and sample recovery.

still possible (Wang and Andrews, 2003)) and thus inhibits the diffusion of H into the gasket allowing the rhenium to maintain its structural integrity under high-pressure.

Beyond the problems of mechanical failure cause by H infiltration into the anvils and gasket, H can cause additional issues with laser heating. San Carlos Olivine contains ~ 10 mol $\%$ Fe in its octahedral site. This should be adequate to couple efficiently with the near-IR laser for high-T heating. However, in a sample of San Carlos Olivine loaded with hydrogen this was not the case. When heating was attempted, no stable heating could be achieved. There was no thermal response from the sample until very high laser power under which the sample suddenly coupled very intensely, resulting in a very high heating temperature and the sample in the heating spot melting and convecting away, leaving only a silica-rich amorphous solid (Fig. 2.8 E) in the heating center and an MgO rich rim (Fig. 2.8 D) after temper-

ature quenching. This behavior seems to imply that even at 300 K, H infiltrates the structure of olivine and changes its optical properties. This hypothesis is supported by the fact that I loaded another DAC with powder from the same olivine sample, after subjecting it to the same laser conditions, found that it coupled very stably and exhibited normal heating behavior with temperature proportionally increasing with increasing laser power (as was not the case when loaded with a H-medium). It is also supported by the fact that throughout this study, pre-heating diffraction patterns of the samples loaded with hydrogen exhibit broad weak diffraction peaks, implying structural modification/weakening by hydrogen.

2.3.3 Sample Recovery

It is extremely useful to be able to recover samples from the DAC after decompression to 1 bar for further analysis, such as imaging in electron microscopy or EDS chemical mapping. However, two factors make this difficult when working with H. The first and most obvious is failure of the diamonds or gasket material. The diamonds and gasket contain the sample and when they fail, the sample is lost. The second factor is that samples that have undergone heating in the presence of hydrogen tend to have a very crumbly texture (Fig. 2.8 F and 2.9), possibly due to hydrogen infiltration at high pressure and subsequent loss upon decompression.

I have managed to overcome these problems in some cases with a combination of luck and technique. In cases where the sample crumbles, I have managed to capture the sample material in pressed indium. I achieve this by placing a small amount of indium over the sample, then closing the DAC and gently pressing. The indium is malleable and flows around the sample capturing it and allowing it to be lifted out on the pressed indium foil. Indium is used for its combination of malleability and Raman-inactivity. In some samples with higher structural integrity, I have also managed to
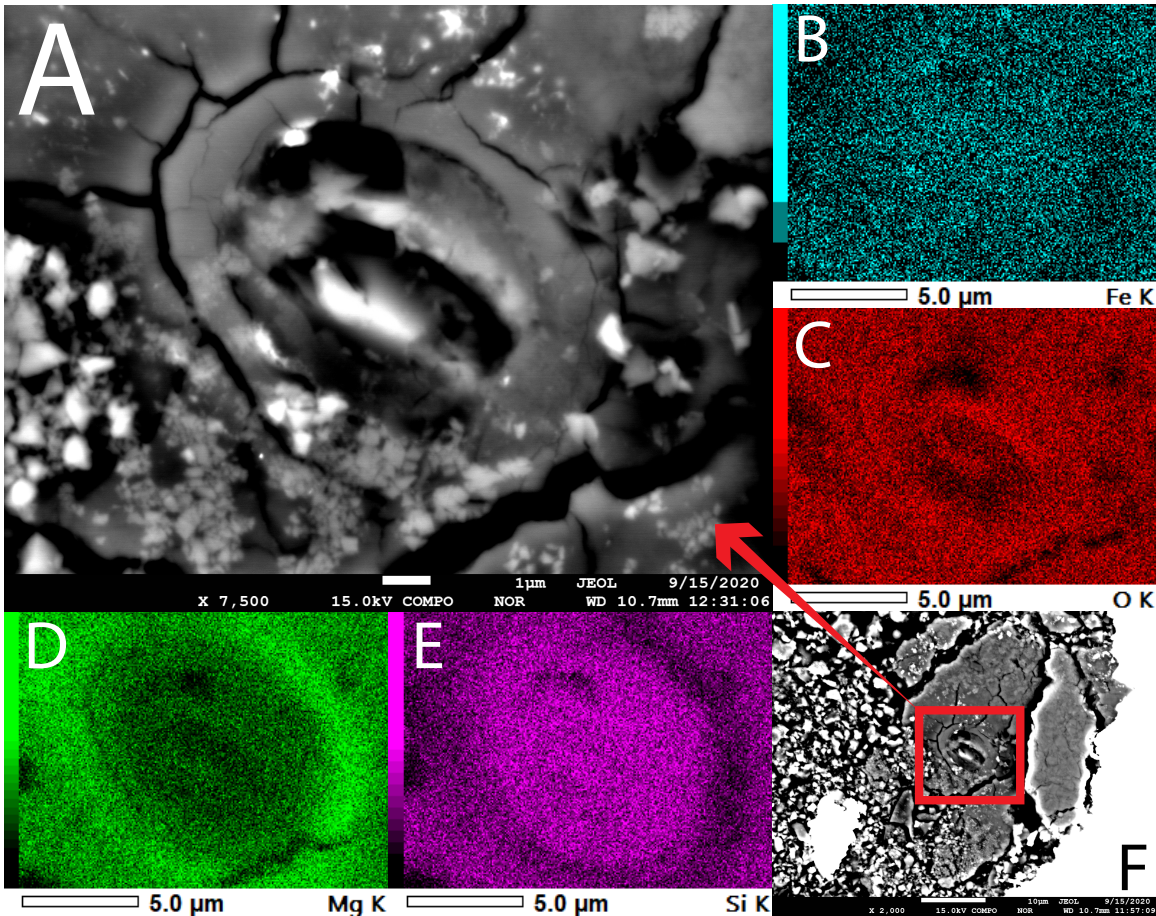
Figure 2.8: EPMA (SEM) image of San Carlos Olivine after attempted laser heating as described at the end of section 2.3.2 along with EDS maps of the elements present in the starting material. Note that Mg and Si are anti-correlated with silica existing in the amorphous (as detected by XRD) center region which underwent higher temperature heating. Also note the texture of the recovered sample which will be discussed in section 2.3.3.

recover the sample from the cell by opening the cell to release the pressure medium, then closing and re-compressing. The compression with no medium to hydrostatically oppose the rhenium gasket causes the gasket to collapse around the sample, trapping it so it can be lifted out.

mag ⊞	det	4/28/2022	HV	HFW	WD	├──────40 µm──────┤
1 750 ×	ETD	5:21:17 PM	2.00 kV	118 µm	4.1 mm	Helios
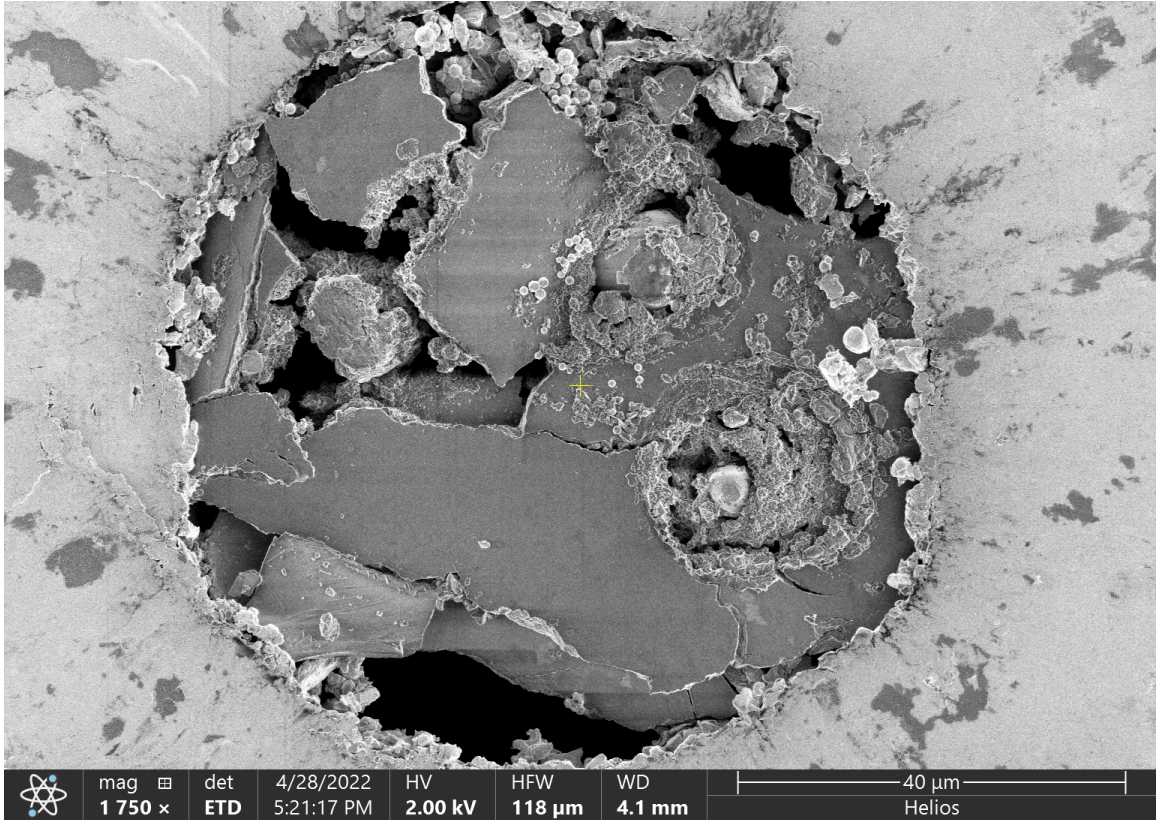
Figure 2.9: SEM sample of a recovered fayalite sample (chapter 5). Note the crumbly nature of the sample, especially around the three heated spots (at 1:00, 4:00, and 10:00). This sample crumbling after reaction with hydrogen has proved detrimental to sample recovery efforts.

Chapter 3

REACTION BETWEEN HYDROGEN AND FERROUS/FERRIC OXIDES AT HIGH PRESSURES AND HIGH TEMPERATURES – IMPLICATIONS FOR SUB-NEPTUNES AND SUPER-EARTHS

3.1 Abstract

Sub-Neptune exoplanets may have thick hydrogen envelopes and therefore develop high-pressure interfaces between hydrogen and the underlying silicates/metals. Some sub-Neptunes may convert to super-Earths via massive gas loss. If hydrogen chemically reacts with oxides and metals at high pressures and temperatures (P-T), it could have impact for the structure and composition of the cores and atmospheres of sub-Neptunes and super-Earths. While H_2 gas is a strong reducing agent at low pressures, the behavior of hydrogen is unknown at the P-T expected for the sub-Neptunes' interiors where hydrogen is a dense supercritical fluid. Here I report experimental results of reactions between ferrous/ferric oxides and hydrogen at 20–40 GPa and 1000–4000 K utilizing the pulsed laser-heated diamond-anvil cell combined with synchrotron X-ray diffraction. Under these conditions, hydrogen spontaneously strips iron off the oxides, forming Fe-H alloys and releasing oxygen to the hydrogen medium. In a planetary context where this reaction may occur, the Fe-H alloy may sink to the metallic part of the core, while released oxygen may stabilize as water in the silicate layer, providing a mechanism to ingas hydrogen to the deep interiors of sub-Neptunes. Water produced from the redox reaction can also partition to the atmosphere of sub-Neptunes. Therefore, water could be common among sub-Neptunes with thick hydrogen atmosphere over a rocky/metallic core, which has

important implications for understanding the composition of their atmospheres. In addition, super-Earths converted from sub-Neptunes may contain a large amount of hydrogen and water in their interiors, distinct from smaller rocky planets which were formed dry.

3.2   Introduction

A large number of exoplanets have been discovered at sizes between Earth and Neptune (3.8 Earth radii, $R_\oplus$) from the Kepler mission (Bean *et al.*, 2021). Demographics of these close-in orbiting exoplanets show some important features. For example, much smaller number of planets have been found at 1.5–2.0$R_\oplus$, which is called "radius gap" (Fulton *et al.*, 2017; Fulton and Petigura, 2018). The gap appears to divide the exoplanets into low-density, larger-sized planets with thick atmospheres, called sub-Neptunes, and higher-density, smaller-sized planets with thin atmospheres, called super-Earths. The dataset also reveals that the planets of 2.7–3$R_\oplus$ size are 4–10× more abundant than planets just 20% larger, a phenomenon known colloquially as the "radius cliff" (Fulton and Petigura, 2018; Kite *et al.*, 2019).

These features in demographics are likely linked to the formation and evolution of these planets (Bean *et al.*, 2021). In particular, sub-Neptune type planets, with rocky/metallic cores and H-rich atmospheres, do not exist in our solar system and therefore explaining their formation and evolution is an important challenge in planetary science (note that "core" in this paper refers to a dense heavy element layer with silicates/oxides and metals following the sub-Neptune literature rather than the metallic core at the center of rocky planets generally discussed in the rocky planet literature). As planets grow appreciably larger than Earth, their increased mass allows them to more efficiently accrete and retain nebular gas (Pollack *et al.*, 1996). However, the noticeably smaller population of planets greater than 3$R_\oplus$ (radius cliff)

requires some other processes to explain the observation. Studies have shown that sub-Neptunes at $2 \leq R_{\oplus} \leq 3$ have likely interiors with the silicate/metal core overlain by thick hydrogen-dominated envelope (e.g. Rogers *et al.*, 2011). Based on extrapolation of low-pressure experimental data (Hirschmann *et al.*, 2012), Kite *et al.* (2019) suggests that the radius cliff is due to the increasing solubility of H_2 from the H envelope into the magma ocean (molten core) at pressures greater than a few GPa's of pressure which is achieved at the atmosphere-core interface of sub-Neptunes that reach $3R_{\oplus}$ while undergoing runaway accretion of nebular gas. Such ingassing could prevent further growth of H atmosphere and therefore increase in radius of the planets, possibly explaining the lower abundance of planets with $> 3R_{\oplus}$.

It is important to consider that hydrogen is a strong reducing agent. At 1 bar and 1000 K, FeO can be reduced to Fe metal by gaseous hydrogen and the reaction produces H_2O (Sabat *et al.*, 2014):

$$\text{FeO (oxide)} + H_2 \text{ (gas)} \rightarrow \text{Fe (metal)} + H_2O \text{ (vapor)}. \tag{3.1}$$

Gibbs free energy for this reaction is 12.328 kJ/mol O_2 and therefore the reaction is endothermic. The kinetic effects for the reaction reduce with an increase in temperature and become very small when FeO is molten at 1 bar (Chipman and Marshall, 1940; Hayashi and Iguchi, 1994).

If reaction 3.1 continues to occur at higher pressures, it may play an important role for the structure and evolution of sub-Neptunes. For example, the reaction could enable chemical exchange between the core and the atmosphere of sub-Neptunes. In addition, water can be produced and partition into atmosphere and core. Despite the importance, to our knowledge, there is no experimental data examining the possibility of reaction 3.1 at the *P-T* conditions estimated for the interface between a hydrogen-rich atmosphere and magma ocean (or the solid silicate/metal core) of sub-Neptunes

and the upper part of magma oceans where hydrogen physically is mixed with silicate. Under those conditions, hydrogen is a dense molecular fluid, not a gas (Trachenko *et al.*, 2014) and H_2O is a dense molecular ionic fluid, not a vapor (Prakapenka *et al.*, 2021), which can affect the energetics of reaction 3.1. For example, the reaction becomes strongly exothermic if H is an atomic gas instead of molecular gas at 1 bar and 1000 K (Sabat *et al.*, 2014). It is also of interest if similar reduction can occur for Mg^{2+}, main cation of planetary silicates/oxides, by hydrogen. Gibb's free energy of $MgO + H_2 \rightarrow Mg + H_2O$ reaction decreases dramatically from 284.092 kJ/mol O_2 (endothermic) to -15.632 kJ/mol O_2 (exothermic) at 1 bar and 1000 K if atomic hydrogen (2H vs. H_2) is considered instead of molecular hydrogen (Sabat *et al.*, 2014). However, there are no experimental results examining such chemical reactions at high *P-T*.

The main reason for lack of such data is the difficulties working with hydrogen at high pressure (Deemyad *et al.*, 2005). Being the smallest atom, hydrogen can diffuse into diamond anvils and make them extremely brittle, resulting in anvil damage or break. The problem becomes even more severe with laser heating. Technical advancements such as pulsed laser heating (Deemyad *et al.*, 2005; Goncharov *et al.*, 2010) and inert gasket coatings (Pépin *et al.*, 2014) enable us to perform experiments at elevated *P-T* conditions. In this work, I experimentally explore the possibility of iron-bearing oxides interacting with hydrogen at the *P-T* conditions expected for the hydrogen-oxide/metal interface in sub-Neptunes. I also discuss implications of this interaction on sub-Neptunes.

Table 3.1: Experimental runs performed in this study. H.E.: # of heating events (10^5 laser pulses at 10 kHz; for more information see section 3.3.2). S.M.: starting material. Temperature, T, is given as the average T recorded from 20 measurements (10 each up and down stream) over 1 H.E. and the uncertainty is the standard deviation of those 20 measured temperatures. I estimate 10% uncertainty for the pressure values presented here (see related discussions in the method section). fcc: face-centered cubic. dhcp: double hexagonal close packed.

[1] below detection threshold of the spectroradiometry

Run #	S.M.	P (GPa)	T (K)	H.E.	Result
Hem-1	Fe_2O_3	26	3400±200	2	FeO + fcc FeH_x
Hem-2	Fe_2O_3	26	1600±300	6	fcc FeH_x
Hem-3	Fe_2O_3	38	2000±1000	3	FeO + fcc FeH_x
Hem-4	Fe_2O_3	38	1850±250	5	fcc FeH_x
Mg50-1	$(Mg_{0.5}Fe_{0.5})O$	23	3200±400	4	(fcc+dhcp) FeH_x + $Mg(OH)_2$ + MgO
Mg50-2	$(Mg_{0.5}Fe_{0.5})O$	23	2450±250	4	(fcc+dhcp) FeH_x + $Mg(OH)_2$ + MgO
Mg50-3	$(Mg_{0.5}Fe_{0.5})O$	22	2550±500	2	(fcc+dhcp) FeH_x + MgO
Mg50-4	$(Mg_{0.5}Fe_{0.5})O$	23	2600±200	2	dhcp FeH_x + MgO
Mg90-1	$(Mg_{0.9}Fe_{0.1})O$	30	3000±350	2	fcc FeH_x + MgO + $Mg(OH)_2$
Mg90-2	$(Mg_{0.9}Fe_{0.1})O$	30	3900±800	2	$(Mg_{0.9}Fe_{0.1})O$
Mg90-3	$(Mg_{0.9}Fe_{0.1})O$	31	<1000[1]	1	$Mg(OH)_2$ + fcc FeH_x + MgO
MgO-1	MgO + Fe	27	2900±150	2	MgO + (fcc+dhcp) FeH_x
MgO-2	MgO + Fe	40	2700±100	2	MgO + (fcc+dhcp) FeH_x
MgO-3	MgO + Fe	40	2800±100	1	MgO + (fcc+dhcp) FeH_x
MgO-4	MgO + Fe	40	2500±100	1	MgO + (fcc+dhcp) FeH_x
MgO-5	MgO + Fe	40	2950±100	1	MgO + (fcc+dhcp) FeH_x
MgO-6	MgO + Fe	40	3100±100	1	MgO + (fcc+dhcp) FeH_x

3.3 Materials and Methods

3.3.1 Materials

Fe_2O_3 and MgO were 99.9% and 99.95% pure, respectively, synthetic powders from Alfa Aesar. Fe metal was a 99.9% pure powder from Aldrich. $(Mg_{0.5}Fe_{0.5})O$

was synthesized at ambient pressure by wet chemistry producing a mixed (Mg,Fe) oxalate, then decomposed at 1100 K under an $f_{O_2} = 10^{-17}$ atmosphere for 10 hours. $(Mg_{0.9}Fe_{0.1})O$ was prepared by reaction of Fe_2O_3 with MgO and Fe in an Fe crucible at 1300 K for 10 hours in an evacuated silica tube. The powder was cold-pressed into foils with approximately $10\,\mu$m of thickness. All the samples were loaded without mixing with metallic Fe except for the MgO runs because MgO does not directly couple with near IR lasers. The foils were loaded into a $125\,\mu$m hole drilled in a rhenium gasket which had been indented by diamond anvils with $200\,\mu$m diameter culets, then coated with $\sim$800 Å of gold to hinder hydrogen diffusion into the gasket material. Small grains of ruby and gold were loaded at the edge of the sample chamber away from the sample foil for pressure calibration during gas loading and synchrotron experiments, respectively. The cells were then placed in a Sanchez GLS 1500 gas loading system and loaded with pure H_2 gas at a pressure of 1000–1500 bar. The samples were compressed to pressures between 20 and 40 GPa at 300 K before synchrotron laser-heating experiments.

3.3.2 Synchrotron Experiments

Synchrotron X-ray diffraction (XRD) images were collected at high P-T in double-sided laser-heated diamond-anvil cell (LHDAC) at the 13-IDD beamline of the GeoSoilEnviroConsortium for Advanced Radiation Sources (GSECARS) sector at the Advanced Photon Source (APS). Monochromatic X-ray beams of wavelength 0.4133 Å or 0.3344 Å were focused on the sample in LHDAC. Near-infrared laser beams were coaxially aligned and focused with the X-ray beams for in-situ laser heating. To reduce the amount of hydrogen diffusion into the anvils and the gasket material, I utilized the pulsed laser heating system at the GSECARS 13ID-D beamline at the APS (Deemyad *et al.*, 2005; Goncharov *et al.*, 2010). "Heating events"

consisted of 10^5 pulses at $10\,\mathrm{kHz}$. This gives a time of $10\,\mathrm{s}$ for each heating event, but the pulse width of $1\,\mu\mathrm{s}$ gives an integrated laser exposure time of $0.1\,\mathrm{s}$. The laser heating spot size is approximately a $25\,\mu\mathrm{m}$-diameter circle and the X-ray spot size is $3{\times}4\,\mu\mathrm{m}$. The heating events were synchronized with gated synchrotron X-ray beams such that diffraction measurements can take place only when the sample reaches the highest temperature during heating. Multiple heating events were conducted to accumulate enough diffraction peak intensities from the sample during high temperature heating. The X-ray beam was co-axially aligned with the laser beams in order to obtain diffraction patterns at the center of the hot spot. The sufficiently smaller X-ray beam-size also reduces the impact from radial thermal gradients in the hot spot. Previous studies have shown that the laser heating system provides a flat top laser beam intensity profile which is useful to further reduce thermal gradients in the hot spot (Prakapenka $et\ al.$, 2008).

Temperatures were estimated by fitting thermal spectra from both sides to the gray-body equation (Prakapenka $et\ al.$, 2008). 2-D diffraction images, collected from a Dectris Pilatus 1M CdTe detector, were integrated into 1-D diffraction patterns using DIOPTAS (Prescher and Prakapenka, 2015). Using the CeO_2 and LaB_6 standards, I determined the sample to detector distance and corrected for tilt of the detector. Pseudo-Voigt profile functions were fitted to the diffraction peaks to determine the unit-cell parameters in PeakPo (Shim, 2019). The unit-cell parameter fitting was conducted based on the statistical approaches presented in Holland and Redfern (1997) in PeakPo. During synchrotron experiments, pressure was calculated by combining the measured unit-cell volume of gold with its equation of state (Ye $et\ al.$, 2017) using Pytheos (Shim, 2018). Pressure calibrants were placed at the edge of the sample chamber to avoid reactions/alloying with the sample material at high temperature, and thus pressure could not be measured during heating. Laser heating
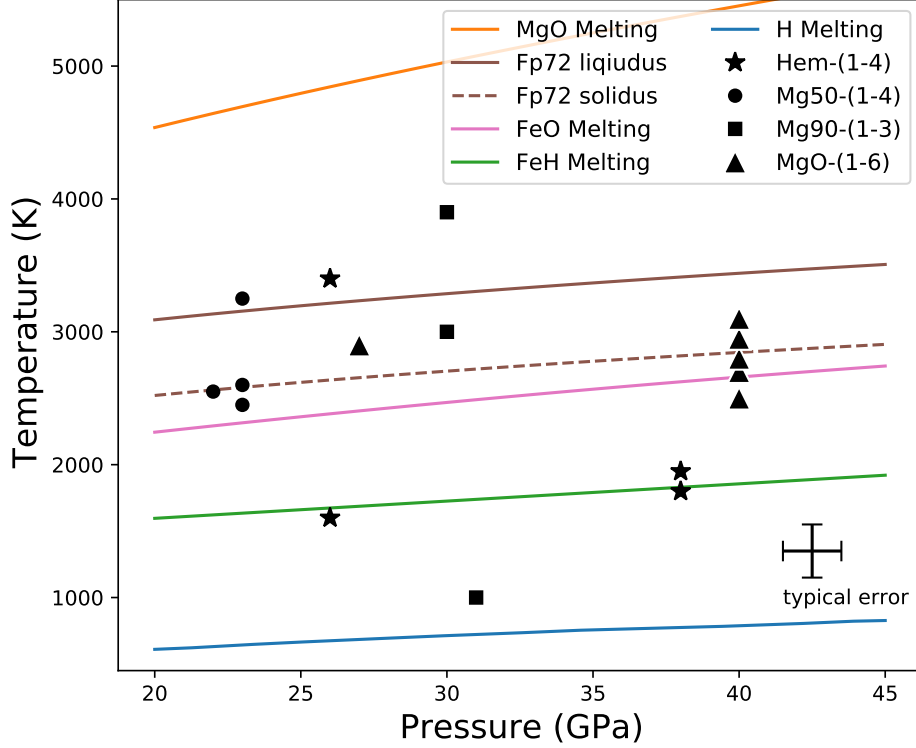
Figure 3.1: Pressure-temperature (*P-T*) conditions of the LHDAC experiments in this study (data points) shown with the melting curves of relevant materials: MgO: Kimura *et al.* (2017); ($Mg_{0.72}Fe_{0.28}$)O: Fu *et al.* (2018); FeO: Boehler (1992); FeH$_x$: Sakamaki *et al.* (2009a); H: Gregoryanz *et al.* (2003). No experiment in this study exceeded the melting temperature of MgO, while most were near or above the melting temperature of FeO and FeH$_x$. All experiments were conducted above the melting temperature of hydrogen.

in a diamond-anvil cell can result in a pressure increase during heating (i.e., thermal pressure). Previous calculations have shown that thermal pressure of a liquid medium (Ar) at temperatures of 1000–4000 K is approximately 0.5–2.5 GPa (Dewaele *et al.*, 1998). However, the pressure change is difficult to predict because it is sensitive to the properties of medium used (Goncharov *et al.*, 2007). The experiments presented here were conducted in a hydrogen medium which is more compressible than Ar. Furthermore, the hydrogen medium around the heating spot should be fluid during heating

as the temperatures were well above the expected melting of hydrogen (Fig. 3.1). Therefore, thermal pressure may not have been severe in our case. However, I assign a conservative estimate of 10% for the pressure uncertainty to reflect the fact that I did not measure pressure during laser heating.

3.4   Results

3.4.1 Fe_2O_3

At 38 GPa, after a single heating event at 1500 K, all Fe_2O_3 peaks disappeared and Fe_2O_3 transformed into FeH_x and FeO through reaction with H (Fig. 3.2a,b). FeH_x was in the face-centered cubic structure (fcc) as expected for these P-T conditions (Pépin *et al.*, 2014), which can be distinguished from fcc Fe by its significantly expanded unit-cell volume of $47.00\,Å^3$ at high-pressure and 300 K after heating, in line with the expected unit-cell volume for stoichiometric (x=1) fcc FeH_x (Narygina *et al.*, 2011b), compared to the expected unit-cell volume of pure (hydrogen free) fcc Fe, $40.59\,Å^3$ (Fig. 3.3) (Boehler *et al.*, 1990). Upon further heating (4 more heating events) between 1600 and 2000 K, it transformed completely to fcc FeH_x, making it the sole phase remaining. All heating events occurred above the melting temperature of H_2 (Gregoryanz *et al.*, 2003), below the melting temperature of FeO (Boehler, 1992), and near the liquidus of FeH_x (Sakamaki *et al.*, 2009b) (Fig. 3.1).

At 26 GPa, after a single heating event at 1300 K, Fe_2O_3 transformed into FeH_x and FeO through reaction with H, consistent with the experiment at 38 GPa. As in the higher pressure experiments, the unit cell expansion of the iron metal phase is consistent with stoichiometric fcc FeH (Narygina *et al.*, 2011b). Upon further heating (5 more heating events) between 1300 and 1600 K, it transformed completely to fcc FeH_x, making it the sole phase remaining. This observation is also consistent
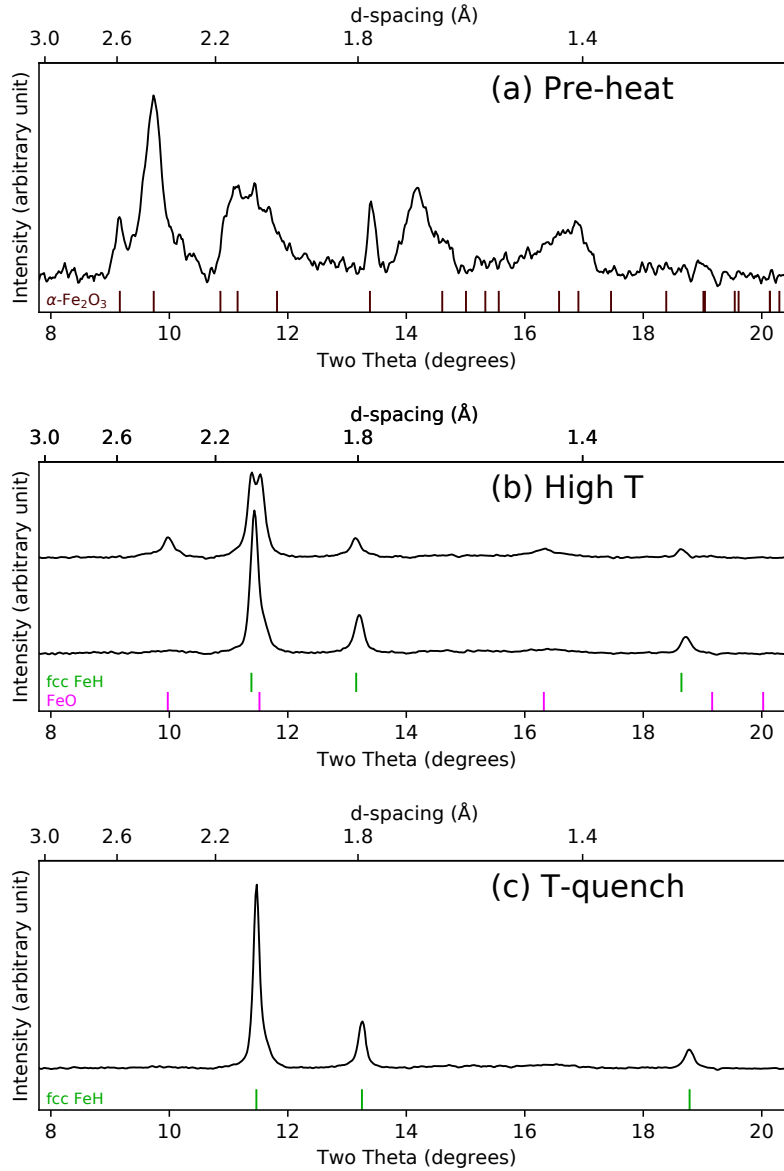
Figure 3.2: X-ray diffraction patterns from run Hem-4 (Table 3.1) taken at 38 GPa before heating (a), during heating ($\sim$1850 K) (b), and after heating (c). The upper high-T pattern in (b) is during the first heating event, and the lower is during the final heating event. The vertical tick marks below each integrated diffraction pattern represent the diffraction peak positions of the various observed mineral phases. Initially both FeO and FeH$_x$ were formed but after 4 heating events only FeH$_x$ was observed in diffraction patterns.

with the higher pressure results. All heating events in this run (Hem-2) were conducted above the melting temperature of H but below the melting temperature of
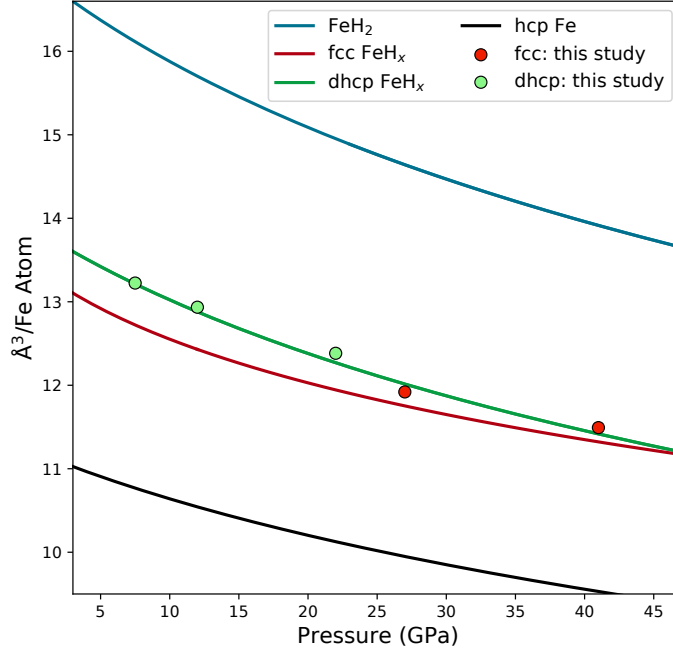
Figure 3.3: Comparison of the unit-cell volumes per Fe atom (V/Z) of Fe and Fe-H phases observed in our experiments and the volume previously reported. Both the fcc and dhcp FeH_x phases observed in this study (red and green circles respectively) show V/Z consistent with 1:1 stoichiometric FeH. Equations of state for hcp Fe, fcc FeH, dhcp FeH, and FeH_2 are from Dewaele *et al.* (2006), Narygina *et al.* (2011b), Pépin *et al.* (2014), and Pépin *et al.* (2014), respectively.

FeO (Fig. 3.1). While FeO persisted, it maintained its cubic structure at high temperatures, but converted to the distorted rhombohedral structure (Yagi *et al.*, 1985; Fei and Mao, 1994; Ono *et al.*, 2007) upon temperature quench to 300 K. However, experiment Hem-1 was conducted above the melting temperature of all materials involved and yielded the same results (although complete transformation of FeO to FeH was not achieved because heating was stopped after 2 events due to instability during heating in order to preserve the integrity of the sample and diamond anvils).

The XRD observations can be explained by the following chemical reaction:

$$Fe_2O_3 + 4H_2 \rightarrow 2FeO + H_2O + 3H_2 \rightarrow 2FeH + 3H_2O \tag{3.2}$$
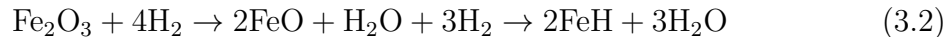
I have direct observation of diffraction peaks from Fe_2O_3, FeO, and FeH_x. The existence of H_2O is inferred from stoichiometry because it is not seen in the X-ray

diffraction patterns. This is likely due to the small X-ray scattering cross-section of water compared to iron-hydrogen alloy. I also found that the main diffraction peak of H_2O ice-VII 011 exists at nearly the same d-spacing as the fcc FeH_x 111 reflection, as well as the FeO 200 reflection at this pressure. The diamond anvils failed during the experiments and therefore I could not decompress the sample for further X-ray diffraction measurements.

3.4.2 $(Mg_{1-x}Fe_x)O$

$(Mg_{0.5}Fe_{0.5})O$

At 23 GPa, after laser heating at 2500–3200 K, XRD patterns showed diffraction peaks from FeH_x (Fig. 3.4(b)). The observation suggests that H reduces Fe^{2+} in the (Mg,Fe)O starting material and induces the formation of iron-hydrogen alloy. This is supported by the fact that the unit-cell volume of the reacted ferropericlase was smaller than that of the starting $(Mg_{0.5}Fe_{0.5})O$ after laser heating at 300 K shrinking to nearly that as expected for Fe-free MgO. From the observations, I infer that no more than 10 mol% of Fe remains in the (Mg,Fe)O after laser heating in a H medium. Both the face-centered cubic (fcc) and double hexagonal-close packed (dhcp) phases of iron-hydrogen alloy formed. The unit-cell volumes of the fcc and dhcp phases of FeH_x again suggest a 1:1 stoichiometry of iron and hydrogen (or $x \approx 1$), based on comparison with the previous reports (Fig. 3.3) (Narygina *et al.*, 2011b; Pépin *et al.*, 2014). These XRD observations indicate:

$$(Mg_{1-y}Fe_y)O + \frac{3}{2}yH_2 \rightarrow yFeH + (1-y)MgO + yH_2O, \qquad (3.3)$$
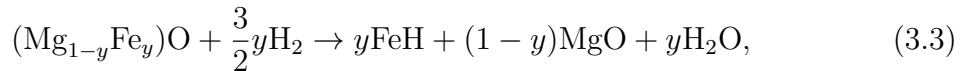
where y is the amount of Fe^{2+} reduced from the oxide to FeH_x alloy. The reaction predicts formation of water, which can be supported by our observation of brucite later discussed in this section.
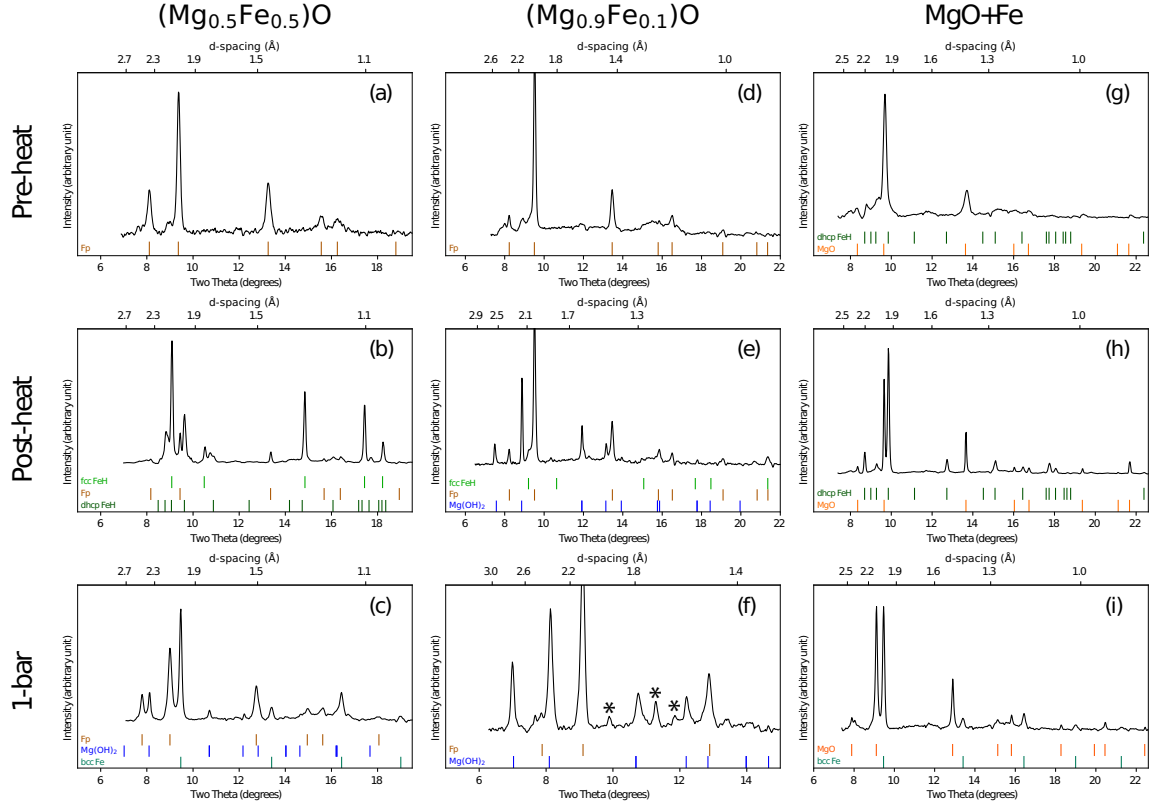
Figure 3.4: X-ray diffraction patterns showing starting materials (first row), materials after heating (second row) and materials after decompression to 1 bar (third row). Patterns shown along columns and their respective heating temperatures are from experiments Mg50-2 (2450K), Mg90-1(<1000K), and MgO-2 (2700K) respectively (Table 3.1). Phases marked "Fp" represent any phase of composition $Mg_{1-x}Fe_x)O$ as in many cases after heating the exact composition is unknown as the sample has reacted with hydrogen and lost some amount of Fe through reduction. The starred peaks in pattern (f) are unassigned. These peaks did not exist after heating at high pressure but appear when the sample was pressure quenched to 1 bar.

The coexistence of the high-temperature phase fcc FeH_x (Narygina *et al.*, 2011b) and the low-temperature dhcp FeH_x phase (Badding *et al.*, 1991) can likely be attributed to either thermal gradients during laser heating (Shen *et al.*, 1998; Fiquet *et al.*, 1996), or formation of the low temperature phase upon temperature quenching (particularly from temperatures above the melting temperature of FeH_x). Though either explanation could explain this observation, the latter is supported by the fact that in experiment Hem-2 where heating was performed below the melting tempera-

ture of FeH, exclusively fcc FeH_x was observed despite the fact the temperature was lower than the heating performed on all $(Mg_{0.5}Fe_{0.5})O$ samples where both the high-T fcc and Low-T dhcp phases were observed. This is possible because during rapid temperature quenching Fcc FeH_x forms at high temperature but does not fully crystallize before the temperature falls bellow the fcc-dhcp phase boundary. Once below that phase boundary, any remaining FeH_x crystallizes in the dhcp structure. Upon decompression to 1 bar, iron converts to the body-centered cubic (bcc) phase. The unit cell parameter of the bcc phase matches well with the known value of 2.8667 Å (Rotter and Smith, 1966), suggesting no hydrogen or other elements persist in iron metal after pressure-quench to ambient pressure.

After heating, there were sometimes a few weak diffraction spots in the diffraction images at high pressure well indexed with $Mg(OH)_2$ (brucite), however, its diffraction intensity was not high enough to appear in the integrated 1D diffraction patterns. Brucite cannot have formed at high-temperature during heating because it decomposes at temperatures of 1000–1400 K in our pressure range (Fei and Mao, 1993). Therefore, brucite should have formed during the temperature quench after heating or along the cooler rim of the heating spot at high pressure. However, the brucite diffraction peaks became much stronger at 1 bar (Fig. 3.4c). Such an increase in the peak intensity of brucite was also observed in $(Mg,Fe)O + H_2O$ experiments during decompression (Kim *et al.*, 2021). The study showed that Mg is highly soluble in H_2O at 20–40 GPa and high temperatures. They also found a reduction in the solubility of Mg in a H_2O medium resulting in the precipitation of brucite during decompression to 1 bar. Therefore, our observation can be interpreted as the result of precipitation of brucite from Mg dissolved in H_2O generated by the redox reaction (Eq. 3.3). The unit-cell parameters of brucite measured at 1 bar are in agreement with the known values (Zigan and Rothbauer, 1967) indicating it is likely the pure

magnesium endmember hydroxide.

$(Mg_{0.9},Fe_{0.1})O$

After one heating event at 1000 K (Tab. 3.1 Mg90-3), strong diffraction peaks of brucite are present (Fig. 3.4e). The observation is in contrast with Mg50 runs where the temperature was too high for brucite formation at high pressure. There are also a few weak diffraction spots consistent with fcc FeH_x. In another run with this composition (Mg90-2), the temperature exceeded 4000 K. During this run, no brucite was formed. Instead, all that was observed after heating was ferropericlase with possibly a small amount of fcc and dhcp FeH_x. These results are consistent with those in the $(Mg_{0.5}Fe_{0.5})O$ experiments with two important differences both of which can be attributed to the lower Fe concentration in the starting material. Firstly, less FeH_x is observed due to the simple fact less Fe^{2+} is present in the starting material to be reduced to Fe metal. Secondly, at high pressure (30 GPa) more brucite was observed in this starting material than in the Mg50 experiments despite the fact that less Fe was present to reduce and release H_2O in $(Mg_{0.9}Fe_{0.1})O$ than in $(Mg_{0.5}Fe_{0.5})O$. This is because the lower Fe content facilitated less efficient laser coupling and therefore lower temperature heating in run Mg90-3 (however in runs Mg90-1 and Mg90-2 such high laser power was needed to achieve coupling that the temperature was very high) within the stability field of brucite (Fei and Mao, 1993). As in the $(Mg_{0.5}Fe_{0.5})O$ runs, it is unlikely the remaining MgO underwent melting during heating.

In the diffraction patterns measured at 1 bar after pressure quench, some new diffraction peaks appeared together with the peaks of (Mg,Fe)O and brucite (Fig. 3.4f). The main unknown peak is at $d_{sp} = 1.703$ Å with possible minor peaks at 1.602 and 1.940 Å (denoted with stars). The peaks could not be indexed with any expected iron or magnesium metal/hydride/hydroxide phases. I do not rule out a possibility

of formation of a new Fe or Mg-bearing phase (metal, hydride, or hydroxide) during decompression in the presence of H_2 and H_2O. The unit cell of ferropericlase is expanded by about 0.5% with respect to pure MgO, corresponding to $\sim$7.5 mol% Fe, marginally less than the starting material (10 mol% Fe). For each mole of iron that is reduced from (Mg,Fe)O, 1 mole of H_2O is produced which can then react with MgO to form brucite.

$$MgO + H_2O \rightarrow Mg(OH)_2. \qquad (3.4)$$

Little change in the Fe content of ferropericlase implies that nearly all H_2O produced reacted with MgO to form brucite. At 1 bar, brucite shows $\sim$1.3% smaller unit cell volume (Zigan and Rothbauer, 1967). At nanometer scale, thermally dehydrated brucite showed the existence of MgO layers, resulting in lower water content (Kumari et al., 2009). Although I do not have direct evidence, such partially dehydrated form of brucite could have smaller unit cell volume.

MgO

MgO was mixed with metallic iron, loaded with pure hydrogen and compressed to 27 GPa. At high pressure before heating, iron metal was in the hydrogenated dhcp structure (Badding et al., 1991). After heating to 2500–3000 K, no change was observed other than a few diffraction spots of fcc FeH_x formed from dhcp FeH_x, consistent with the formation of FeH_x structures from melt seen in the (Mg,Fe)O experiments. The transformation of iron to dhcp FeH_x and then fcc FeH_x with high temperature is the expected behavior of the pure Fe-H binary system (Badding et al., 1991; Pépin et al., 2014; Umemoto and Hirose, 2015). Upon decompression, FeH_x reverted to bcc Fe metal with a unit cell parameter of 2.864±0.002 Å, in agreement with the parameter for pure iron of 2.866 Å (Rotter and Smith, 1966; Kohlhaas et al., 1967). I did not find any evidence of MgO reacting or interacting in any way

with iron metal or hydrogen. The MgO unit-cell volume measured at ambient pressure after heating and decompression was 74.56 Å, consistent with the known value (Fiquet *et al.*, 1996). This observation demonstrates that in the experiments with $(Mg_{1-x}Fe_x)O$ the formation of brucite was a secondary reaction between H_2O (produced by the reduction of FeO to FeH_x) and MgO (Eq. 3.4), not a direct reaction between MgO and H_2.

3.5   Discussion

Our experiments have shown that molecular hydrogen fluid at pressures of 20–40 GPa and temperatures up to 4000 K reduces iron oxides to iron-hydrogen alloys and releases water. From the phase diagrams, our *P-T* conditions likely yielded FeO-rich partial melt from (Mg,Fe)O. Therefore, Fe metal may be formed from partial melt. FeH_x should form as melt and H_2O should form as dense ionic fluid at the *P-T* conditions of our experiments. At the *P-T* conditions expected for the interface between H envelope and oxide/metal core, and for the upper part of the magma ocean where H is dissolved, the reaction opens up a possibility of large H ingassing to the metallic part of the sub-Neptunes' cores and large H_2O ingassing to the silicate/oxide part of the sub-Neptunes' cores (Fig. 3.5). I found no sign of reduction of Mg^{2+} to metal by hydrogen fluid. Therefore, after reaction with hydrogen, the rocky portion of the core will be deficient of FeO (or MgO rich).

Our experiments found brucite from the reaction between MgO and water. While brucite is unlikely to form during heating (but likely during temperature or pressure quenching) and therefore would not exist in sub-Neptunes, its appearance indicates that H_2O can be incorporated as OH in the silicate-oxide part of sub-Neptunes' solid body. Our experiments show that H_2O produced from the reaction does not affect the siderophile behavior of H and its alloying with Fe metal to produce FeH_x.
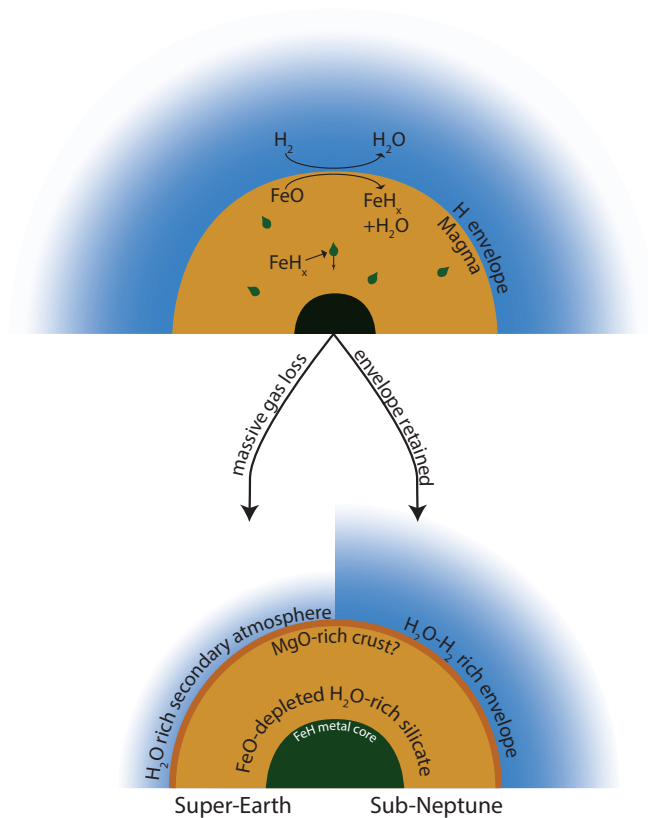
Figure 3.5: Cartoon demonstrating possible implications of the chemical reactions explored in this work. Of particular importance is the link between the atmosphere and interior showing that in large exoplanets the oxidation of the atmosphere may stem from the reduction of the interior. It also demonstrates how super-Earths formed through atmospheric loss from a sub-Neptune may retain significant amounts of its primordial hydrogen stored in their core as an alloy component or its mantle as H_2O.

Water partitioned in the magma ocean would decrease the melting temperature (Litasov and Ohtani, 2002) and therefore extend the magma ocean stage for the cores of sub-Neptunes. However, at the same time the removal of FeO from magma from reaction 3.1 would increase the relative amount of MgO, thus increasing the melting temperature of magma and hastening its solidification. If FeO-depleted layer forms quickly at the topmost part of the oxide magma ocean where magma reacts with dense hydrogen fluid, it can crystallize and form solid crust, which could shutdown reaction 3.3 and therefore limit the ingassing of H (Fig. 3.5). However, such a process

can be also affected by convectional vigor of the magma ocean system and the strength of the FeO-depleted ultra-mafic layer at high P-T, which requires further study.

Studies have suggested that the cores of the sub-Neptunes are not volatile rich (Rogers and Owen, 2021). For Earth-like to Mars-like compositions, if all mantle FeO is reduced, it will produce about 2–4 wt% H_2O in the mantle if all H_2O remains in the silicate part. For the Earth-sized planets, this would amount to 50–100 ocean mass of water stored in the silicate/oxide part. Because H_2O can partition into the H atmosphere and metallic part of the core, this estimation should be regarded the upper bound of H_2O content in the silicate part of the core. Reduction of FeO in silicate can increase the mass of the metallic part of the core. In the upper bound case I discuss here, for a planet with an Earth-like composition and core-mantle ratio, the mass of metallic part would increase by 12–24%, offsetting the mass loss of the silicate part (6–12%). In this case, about 0.2–0.4 wt% of H will be ingassed to the interior as both H_2O and H_2. Again from the reasons I discussed above, this amount should be regarded as the upper bound. Therefore, the amount of ingassed hydrogen I discuss here is far less than the amount considered for the possibility of a significant "ice" component in the cores of sub-Neptunes. In fact, the amount of ingassed hydrogen I discuss here may not be detectable from the analysis of the mass-radius data of exoplanets in current data sets considering the significant uncertainties involved in those properties. While the dissolved H would further enhance the reduction of FeO in the interiors of magma oceans of sub-Neptunes, the redox reaction alone would not ingas sufficient H to explain the "radius cliff".

On the other hand, if such a large amount of H_2 can be indeed ingassed into the silicate/oxide magma ocean through physical mixing, the amount would be enough to reduce all FeO for Earth-like and Mars-like compositions. One source of uncertainty for applying our results to sub-Neptunes, is that the pressure in the deeper part of

magma ocean would be much higher than I studied in this paper. Above 100 GPa, hydrogen fluid undergoes a change from a molecular to a mono-atomic form (Cheng *et al.*, 2020). H_2O would likely be an ionic fluid within the pressure range I studied here and likely at the *P-T* conditions of sub-Neptunes interface (Millot *et al.*, 2019). However, H_2O could be a conducting fluid at pressures over 100 GPa. Such a fundamental change in the properties of reactant and product in reaction 3.1 could change the behavior of the system. If such changes can lead to different redox behavior of the system in the core, it would have important implications for the storage of volatiles and the structure of the very deep interiors of larger sub-Neptunes.

To explain the "radius gap", models have suggested that a large loss of thick hydrogen envelope of sub-Neptunes, either through photoevaporation (and migration) or core-powered loss, could result in a conversion to super-Earths (Owen and Wu, 2013; Schlichting, 2014; Bean *et al.*, 2021). Our experiment shows that through reduction of FeO and alloying of H and Fe, a large amount of hydrogen can be ingassed to the metallic part of the sub-Neptunes' core which then will remain in the metallic core of super-Earths after conversion. Our results also found some H_2O produced by the reduction of FeO can hydrate the silicate/oxide part of the sub-Neptunes' cores. Therefore, from these, I can conclude that super-Earths converted from sub-Neptunes likely have interiors rich in water and/or hydrogen. With cooling of magma ocean, an MgO-rich crystalline layer could form at the topmost part while the deeper part may still be molten. If the structure can be preserved during gas loss, super-Earths converted from sub-Neptunes could have an ultra-mafic crust unlike Earth (Fig. 3.5).

It is also interesting to point out that the cores of sub-Neptunes will experience a few to a few tens of GPa's of pressure decrease during gas loss. The magnitude of the decrease is small compared with very large pressure expected for the deep interiors of sub-Neptunes (or super-Earths) cores. However, the topmost layer can be affected

40

by such a pressure decrease. If the solubility of H_2O and H_2 in silicate increase with pressure, the topmost layer could experience a loss of these volatiles during decompression. The released H_2O and H_2 could be incorporated into the atmosphere and ultimately removed during conversion to super-Earths (Fig. 3.5). Yet, whether they would remain and form secondary atmosphere after the conversion to super-Earths or not is likely dependent on the rate of massive gas loss versus the rate of degassing from the interior, particularly if surface tectonics can control (or delay) the degassing. However, the H stored in the metallic core of former sub-Neptunes would unlikely be affected by the massive gas loss as the pressure decrease would not be enough to change the alloying behavior of H at such high pressures, more than 1 Mbar.

If the water formed from FeO reduction by hydrogen could be outgassed to form H_2O rich secondary atmospheres (Kite and Schaefer, 2021), it can provide a pathway for endogenic high molecular weight atmospheres without relying on delivery of solid-derived volatiles (Ikoma and Genda, 2006). However, this does not mean to explain the oceans on Earth. Despite the Earth's depletion of FeO, and perceived deep reservoirs of nebular hydrogen (Genda and Ikoma, 2008; Hallis *et al.*, 2015; Wu *et al.*, 2018), nearly 50 oceans of hydrogen would need to be reacted with FeO to explain the depletion, far exceeding even the most generous estimations for nebular gas interaction and hydrogen in the core. Instead, this reaction may play an important role in the formation of sub-Neptunes which would grow large enough to accrete large primary H-dominated envelopes.

It is important to point out that the formation of FeH_x alloy instead of Fe metal expected for sub-Neptunes as shown by experiments could make an important contrast for the composition of the metallic cores of super-Earths which are converted from sub-Neptunes as opposed to overgrown terrestrial planets. If a significant amount of

H is ingassed through physical mixing, sinking Fe metal blobs in the magma ocean can alloy with H, i.e., chemical ingassing. As H solubility in Fe metal increases with pressure (Pépin *et al.*, 2017; Piet *et al.*, 2021), such direct alloying of H to iron metal can result in large hydrogen ingassing to the cores of these larger planets. An interesting consequence would be that the larger rocky planets' metallic and oxide parts of the cores generally contain more hydrogen than smaller rocky planets. It is also likely that larger rocky planets' silicate mantle is depleted in FeO but rich in water and hydrogen which could alter the viscosity and therefore impact the vigor of mantle convection and thermal evolution.

3.6   Conclusion

I found that at high pressure-temperature conditions relevant for the interface between H and the cores of sub-Neptunes iron-bearing oxides react with hot dense hydrogen to form iron-hydrogen alloys and water. The chemical sequestration of hydrogen as H_2O as a result of the reduction of FeO, as well as the subsequent formation of FeH_x provide a chemical pathway to supplement physical mixing and enhance the solubility of H in a global magma ocean. Although physical mixing of H could still be important, these chemical reactions support the theory that the super-abundance of sub-Neptunes can be explained by the sharp increase in H in the condensed planetary core as pressure at the base of the H envelope exceeds 10^9 Pa, whereby additional accreted H is partitioned to the interior rather than the atmosphere. These reactions also have implications for the chemical partitioning of growing large planets. Due to the significant amount of H that can alloy with molten Fe, cores on sub-Neptunes (or super-Earths that formed via atmospheric loss from sub-Neptunes) may be rich in H. Additionally the formation of H_2O from the released oxygen may enrich mantles and atmospheres with water; even without direct delivery of H_2O rich materials. In ad-

dition to the support for existing models of planet formation, the chemical reactions explored in this work provide valuable data to build future models and theories. A forthcoming follow up paper will explore the effect of H on Si-bearing systems (Mg-Fe-Si-O-H), as well as lower pressures relevant to shallow magma oceans and magma ocean/envelope interfaces on early rocky planets.

3.7   Acknowledgments

Chapter 4

INTERACTIONS BETWEEN HYDROGEN AND OLIVINE–IMPLICATIONS
FOR VOLATILE STORAGE AND CHEMICAL PARTITIONING IN GROWING
PLANETS

4.1   Abstract

Hydrogen is the most abundant element in the discs of material from which solar/planetary systems form. As rock/metal planetary bodies form in the proto-planetary disk, they may interact with nebular hydrogen in a physical and chemical way. This is especially important for planets that accrete significant envelopes of nebular hydrogen gas. The most abundant type of observed planet with significant envelopes are sub-Neptunes. Sub-neptunes are planets with radii 1.75-3.5R$_\oplus$. This class of planets have a rocky mantle overlain by a thick hydrogen-dominated atmosphere. Interactions between the hydrogen envelope and silicate layer below may play an important role in many planetary processes such as core formation, atmospheric accretion and composition, and mantle mineralogy. However, despite the scientific importance, due to the experimental challenges associated with working with hydrogen there is a paucity of experimental data on the chemical interactions between hydrogen and rocky planetary materials.

In this work, I explore the chemical interactions between mixtures of San Carlos Olivine or silica with 20 wt% metallic iron and hydrogen at pressures of 6-42 GPa and temperatures of 1800–4350 K. These starting materials and experimental conditions are broadly applicable to planetary science but were specifically chosen as representative chemical and pressure-temperature conditions at the surface of a magma ocean

at the base of a thick H-envelope.

I find that when melted, silicate phases break down. Fe and Si are reduced to metallic alloys while the O to which they were bound is released reacting with H to form H_2O. MgO remains stable under these conditions and precipitates out of the melt as periclase. The water produced by these reactions can partition into the mantle or atmosphere possibly producing long-lived stable interior volatile reservoirs or water-rich atmospheres in planets that may have otherwise formed water-poor. The metal alloys produced (Fe-H alloy and Fe-Si) alloy may sink to the core enriching it in those light elements.

4.2   Introduction

Hydrogen is the predominant component of the gaseous disk in which all planets form, and yet is has long been understudied with regards to its chemical impact on planet formation and differentiation. One reason for this is the dearth of high P-T data on the interactions between H and planetary materials because the technical challenges of working with H made the experiments infeasible. Another reason was in classical planet formation models (e.g. Weidenschilling, 1977) rocky planetary cores form too slowly to accrete significant H-dominated primary atmospheres. However, in order to form gas giants via runaway gas accretion, an approximately 10-Earth-mass core must form within the lifetime of the gaseous disk: 10^6–10^7 year (Haisch Jr et al., 2001; Jayawardhana et al., 2006). Core formation by classical planetesimal accretion is believed to take more than 10^7 year beyond 5 AU in our solar system (Goldreich et al., 2004). To explain the existence of gas giants, a number of models have been proposed (e.g. Lambrechts and Johansen, 2012) which form solid planetary cores more rapidly. Not only does this help explain the existence of gas giants, it also results in the more rapid (and thus hot) formation of all kinds of planetary bodies.

The timing, chemistry, and other processes associated with planet formation are of the utmost importance for planetary science (Mordasini *et al.*, 2015) with core-mantle differentiation being one of the most important aspects (Rubie *et al.*, 2011). It is the process during accretion by which denser metal accumulates at the center of an accreting planet either by grain scale percolation or large scale (km-scale) sinking diapirs of liquid metal through crystalline silicates, or by separation of molten metal and silicate in a large scale magma ocean (Rubie *et al.*, 2007). The process by which the metal core forms is intimately linked to its formation timescale. If planets form more quickly, they will also form hotter thus favoring the existence of a global magma ocean. Older studies of both core formation (Lee and Halliday, 1995) and planet formation (Weidenschilling, 1977) favored longer formation timescales and later core formation (up to 100 Myr). However, updated chronometry data suggests a much earlier core formation timescale for the Earth (Kleine *et al.*, 2002) and new planet formation models suggest faster (and thus hotter) accretion (Lambrechts and Johansen, 2012), favoring core formation precipitation of metal from a silicate magma ocean. Beyond the original heat from the nebular materials from which planets form, giant impacts such as the one presumed to have form the moon (Daly, 1946; Hartmann and Davis, 1975) can also cause extensive heating and magma oceans (Tonks and Melosh, 1993; Gabriel and Allen-Sutter, 2021).

Core formation from a magma ocean is a critical time from the perspective of core-mantle chemical partitioning (Siebert *et al.*, 2011). Which elements partition into the core and mantle as the core forms will have long-lasting effects on the structure and dynamics of each. For example, the density of Earth's outer core is ($\sim$10%) less dense than a pure iron-nickel alloy (6% nickel from meteoritic abundances (Birch, 1952; Ringwood, 1977)) which suggests additional light elements must be present (Birch, 1964; Jeanloz, 1979; Mao *et al.*, 1990). Similarly, the Martian core (the only

other core for which we have seismic density measurements) exhibits a density deficit necessitating additional light elements Stähler *et al.* (2021). The main question in both cases is what are the additional light elements and how did they get there?

To answer this question, and understand planetary core formation on a broad level, experimental data is needed to determine if various elements are siderophilic or lithophilic (weather they prefer to exist in metal or rock). Various candidates including S, Si, O, C, and H have been explored over the years (Hirose *et al.*, 2013, and references therein). In this study, I have focused on the Mg-Fe-Si-O-H system.

Fe is the predominant component of the core and Mg the predominant cation in mantle silicates. Thus, the partitioning behavior of Si, O, and H between them at high P-T conditions is important experimental data for core formation models where H is present in magma oceans undergoing differentiation at pressures of 6–42 GPa. While the Earth did not grow large enough to attract a large H envelope to create a high pressure, magma ocean mixing may ingas hydrogen to the deep interior of the proto-Earth, with super-Earth's ingassing may be at least 10x more (Olson and Sharp, 2018). Because large amounts of H_2 are not expected to interface with silicates in Earth, from here onward the focus will be on the implications for the structure and evolution of sub-Neptunes and super-Earths. This is not because the reactions presented in this manuscript cannot occur in the Earth's deep interior, but rather that these larger planets may ingas many oceans of H (Olson and Sharp, 2018) and have a high-P interface between a H-envelope and silicate magma ocean (Kite *et al.*, 2019; Rogers *et al.*, 2011) and thus undergo major alteration by reaction with H_2.

Super-Earth's–rocky planets larger than earth ($\sim$1-1.75$R_\oplus$) (Fulton *et al.*, 2017) lacking large gaseous/fluid envelopes–and sub-Neptunes–planets of radius 1.75-3.5$R_\oplus$ (Fulton *et al.*, 2017) with a rock/metal core overlain by a thick H-dominated atmosphere (Rogers *et al.*, 2011)–appear to be the most abundant type of planets in

extrasolar systems. There is a gap in the frequency between these two populations colloquially known as the "fulton gap" (Fulton *et al.*, 2017). The decrease is frequency of planets of radius larger than $1.75R_\oplus$ likely due to the fact that the planets that would form within the gap undergoing massive gas loss, thus the alternative name: the Photoevaporation Valley (Owen and Wu, 2013; Fulton *et al.*, 2017). The explanation may explain the double-peaked distribution but it is not a complete explanation of the histogram. Planets of radius 2.7-$3R_\oplus$ are 4-10x more abundant than planets just 20% larger (a phenomenon known colloquially as the "radius cliff") (Fulton and Petigura, 2018; Hsu *et al.*, 2019). A leading hypothesis to explain the radius cliff is that due to the increasing solubility of H_2 from the atmosphere in in the magma ocean at pressures greater than 10^9 Pa–pressures achieved at the atmosphere-mantle interface of planets that reach $3M_\oplus$ while undergoing runaway accretion of nebular gas (Pollack *et al.*, 1996)–additional H accreted is partitioned into the interior rather than the atmosphere thus disrupting the radial growth of the planet (Kite *et al.*, 2019).

This model (and others) are extrapolated from lower pressure data (Hirschmann *et al.*, 2012). Kite and Ford (2018) explicitly state the need for higher pressure and temperature experiments on H-solubility and reactions at the conditions present in sub-Neptunes, which I present here.

The interactions between primordial H rocky planetary materials and their impact on the redox conditions and volatile budget of the growing planet have been explored experimentally (in Chapter 3 and by Hirschmann *et al.* (2012)) and theoretically (Ikoma and Genda, 2006; Kite *et al.*, 2019; Kite and Schaefer, 2021; Kite *et al.*, 2020; Lichtenberg, 2021). However, these studies center around the reduction of oxidized Fe by hydrogen:

$$FeO + H_2 \rightarrow Fe + H_2O \tag{4.1}$$

when in reality, planets should also contain not just iron oxides, but also Si in the form of silica/silicates.

A previous study on the possibility of reactions between forsterite and H found no chemical reaction or breakdown of Mg_2SiO_4 when heated to 1000 K at pressures of 10-15 GPa (Shinozaki *et al.*, 2012). While this seems to imply that Mg^{2+} and Si^{4+} to not interact with hydrogen in the same way $Fe^{2+,3+}$ does, it is possible for both to be reduced to metal if the temperature is sufficiently high for planetary interiors, over 2000 K. As shown in Chapeter 3, MgO (Mg^{2+}) is not reduced to metal (Mg^0) by H at high P-T conditions. Silicon can take the form of Si^{4+} or Si^0, and can be converted between the two at pressures of 2–3 GPa and temperature of 1500–1700 K via the following redox reaction (Shinozaki *et al.*, 2014; Futera *et al.*, 2017):

$$SiO_2 + 4H_2 \rightarrow SiH_4 + 2H_2O \tag{4.2}$$
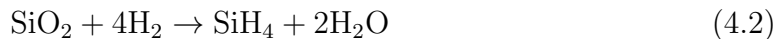
This exciting possibility shows that iron oxides may not be the only planetary material that can be altered by H to release water. However, in sub-Neptunes or other growing planets with high-P silicate magma-H envelope interfaces, as well as the deep interior where differentiation and core formation occur, the pressures and temperatures are appreciably higher than in the aforementioned previous studies. In this study, I present experiments on the chemical reactions and phase stability of San Carlos olivine or silica mixed with Fe under a H atmosphere at pressures of 6–42 GPa and temperatures of 1900–4500 K

4.3 Materials and Methods

4.3.1 Sample Materials and Preparation

Natural San Carlos olivine was used for the silicate sample. Synthetic powders of Fe metal (Aldrich 99.9%+ purity) and SiO_2 (Alfa Aesar 99.995% purity) were also

Table 4.1: Experimental runs performed in this study. H.E.: # of heating events (10^5 laser pulses at 10 kHz; for more information see section 4.3.2). S.M.: starting material. Temperature, T, is given as the average T recorded from 20 measurements (10 each up and down stream) over 1 H.E. and the uncertainty is ±100K for heating events where stable heating was achieved. When T changed over the course of the heating event the temperature is reported as a the range of values measured. I estimate <10% uncertainty for the pressure values presented here (see related discussions in the method section). FeH_x when present takes on both the face centered cubic (fcc) and double hexagonal close packed (dhcp) structures.

Run ID	S.M.	P	T	H.E.	Method	Result
SCO-1	Olv+Fe	7	2900	1	XRD+EPMA	MgO + B2 FeSi
SCO-2	Olv+Fe	6	2700	1	XRD+EPMA	MgO + FeH_x+ SiO_2
SCO-3	Olv+Fe	8	2900	1	XRD+EPMA	MgO + FeH_x+ B2 FeSi
SCO-4	Olv+Fe	7	2900	1	XRD+EPMA	MgO + FeH_x+ B2 FeSi
SCO-5	Olv+Fe	7	2750	1	XRD+EPMA	MgO + FeH_x+ B2 FeSi
SCO-6	Olv+Fe	17	2600-3500	1	XRD	Rw + Wd + B2 FeSi + Fe_5Si_3 + MgO + FeH_x
SCO-7	Olv+Fe	21	2300-2900	1	XRD	Rw + FeH_x + Fe_5Si_3 + SiO2 + MgO
SCO-8	Olv+Fe	21	2550-3200	2	XRD	FeH_x + Fe_5Si_3 + SiO2 + MgO
SCO-9	Olv+Fe	22	3000-3700	1	XRD	Rw + FeH_x+B2 FeSi + Fe_5Si_3 + SiO2 + MgO
SCO-10	Olv+Fe	30	4200	7	XRD+EPMA	MgO + FeH_x + B2 FeSi + $MgSiO_3$
SCO-11	Olv+Fe	37	3300-4500	1	XRD	MgO + FeH_x + B2 FeSi
SCO-12	Olv+Fe	42	2850	2	XRD+EPMA	MgO + FeH_x + $MgSiO_3$
SCO-13	Olv+Fe	42	2600-4350	6	XRD+EPMA	MgO + FeH_x + B2 FeSi
SIL-1	SiO_2+Fe	14	1900	1	XRD+Raman	SiO_2 + B2 FeSi+ FeH_x
SIL-2	SiO_2+Fe	14	2500-3300	1	XRD+Raman	SiO_2+ B2 FeSi
SIL-3	SiO_2+Fe	14	2000-3000	1	XRD+Raman	SiO_2+FeH_x
SIL-4	SiO_2+Fe	39	2250	1	XRD	SiO_2 + B2 FeSi
SIL-5	SiO_2+Fe	39	1800-3800	6	XRD	SiO_2 + B2 FeSi

used, depending on the desired composition. Powders were ground and mixed in an alumina mortar, then cold-pressed into foils with approximately $10\,\mu$m of thickness. Rhenium gaskets were indented by diamond anvils with $200\,\mu$m diameter culets and then drilled with $125\,\mu$m diameter holes. The rhenium gaskets were then coated with $\sim$800 Å of gold to inhibit hydrogen diffusion into the gasket material. The gaskets were placed back onto the diamond culets, followed by the sample foils and gold and ruby grains for pressure calibration. The cells were then loaded with 1000–1500 bar of pure H_2 gas in a Sanchez GLS 1500 gas loading system and then compressed to pressures between 10 and 40 GPa—measured using ruby fluorescence (Piermarini *et al.*, 1975)—at 300 K before synchrotron laser-heating experiments.

4.3.2   Synchrotron Experiments

I collected In-situ X-ray diffraction (XRD) images in the double-sided pulsed laser-heated diamond-anvil cell (LHDAC) at the 13-IDD beamline of the GeoSoilEn-viroConsortium for Advanced Radiation Sources (GSECARS) sector at the Advanced Photon Source (APS) synchrotron facility. Near-infrared laser beams and monochromatic X-ray beams of wavelength 0.4133 Å or 0.3344 Å were coaxially aligned and focused on the sample in the LHDAC for in-situ laser heating and XRD. Standard continuous-wave laser heating of H-loaded samples in the DAC results in diamond embrittlement and failure of the anvils (Deemyad *et al.*, 2005). This problem has prevented researchers from obtaining important data on hydrogen-silicate reaction at the pressure-temperature conditions expected for the planetary interiors. To enable these measurements, I utilized a pulsed laser heating system (Deemyad *et al.*, 2005; Goncharov *et al.*, 2010) to mitigate the amount of hydrogen diffusion into the anvils and the gasket material. Each pulsed heating event (H.E.) consisted of 10^5 pulses at 10 kHz and 20 streak spectroradiometry measurements. The pulse width was $1\,\mu$s

which for 10^5 pulses gives a total laser exposure time of 0.1 s. The X-ray spot size is 3×4 μm and laser-heating spot size is an approximately 25 μm-diameter circle. The laser pulses were synchronized with synchrotron X-ray beams such that diffraction measurements can take place only when the sample reaches the highest temperature during heating. The small X-ray beam size and large laser-heating spot size help mitigate thermal gradients in the high-temperature diffraction patterns. Additionally, Prakapenka *et al.* (2008) showed that the laser heating system provides a flat top laser beam intensity profile which further reduces thermal gradients in the hot spot. While the heating duration is short, I found hydrogen is extremely reactive with molten silicates at high temperatures, overcoming this limitation. Additionally, the use of short pulsed heating to mitigate H-diffusion into the anvils, also reduces the chemical diffusion issues during laser heating typically observed for CW heating (Sinmyo and Hirose, 2010). At no point in any experiment did I note diffusion of MgO with or against thermal gradients as was seen in the H-free system studied by Sinmyo and Hirose (2010).

Thermal emission spectra from both sides of the LHDAC were fitted to the grey-body equation to estimate the temperatures of the double-sided laser-heating (Prakapenka *et al.*, 2008). A Dectris Pilatus 1M CdTe detector was used to collect 2-D diffraction images which I integrated to 1-D diffraction patterns using the DIOPTAS package (Prescher and Prakapenka, 2015). I used the CeO_2 and LaB_6 standards to correct for tilt of the detector and determine the sample to detector distance. Unit-cell parameter fitting was conducted by fitting the diffraction peaks with a pseudo-Voigt profile functions in the PeakPo package (Shim, 2019), proceeding with the statistical approaches presented in Holland and Redfern (1997). Pressure was calculated by comparing the unit-cell volume of a gold grain at the edge of the sample chamber with the equation of state of gold (Ye *et al.*, 2017) before and after

heating. Gold was placed away from the sample rather than mixed with it to prevent reactions/alloying with the sample material, and thus pressure could not be measured at high temperatures. Dewaele *et al.* (1998) showed that thermal pressure in a liquid medium at temperatures of 1000–4000 K is $\sim$ 0.5–2.5 GPa. However, liquid H (all our experiments exceed the melting temperature of H as shown in Fig. 4.1) is more compressible than liquid Ar (the medium studied by Dewaele *et al.* (1998)). Therefore, thermal pressure is likely smaller than the estimation above in our experiments. However, I still assign a conservative pressure uncertainty of $\sim$10% during laser heating due to the fact thermal pressure was not measured. Note that this method does not introduce a severe error for the purpose of this study, which is to explore redox reactions between hydrogen and olivine at high pressures. Raman measurements were conducted for the identification of OH vibrations after heating in runs SIL-1, SIL-2, and SIL-3 utilizing the Raman spectroscopy system at GSECARS (Holtgrewe *et al.*, 2019).

4.4   Results

4.4.1   San Carlos Olivine

Olivine Stability Field

At 8 GPa, after 1 heating event at 2900 K (SCO-3), all diffraction peaks of olivine disappeared (Fig. 4.2). Fe metal is present in both the fcc and dhcp structures, implying alloying with H as these structures are not stable at this pressure in the pure iron system, but can be stabilized by H at this pressure with an expanded unit cell volume (Badding *et al.*, 1991; Narygina *et al.*, 2011b). Fcc Fe has a unit-cell volume of 45.91 Å^3 compared to the expected value from the equation of state of pure Fe of 42.94 Å^3 at this pressure (Dewaele *et al.*, 2006), an expansion of 6.9%. However,
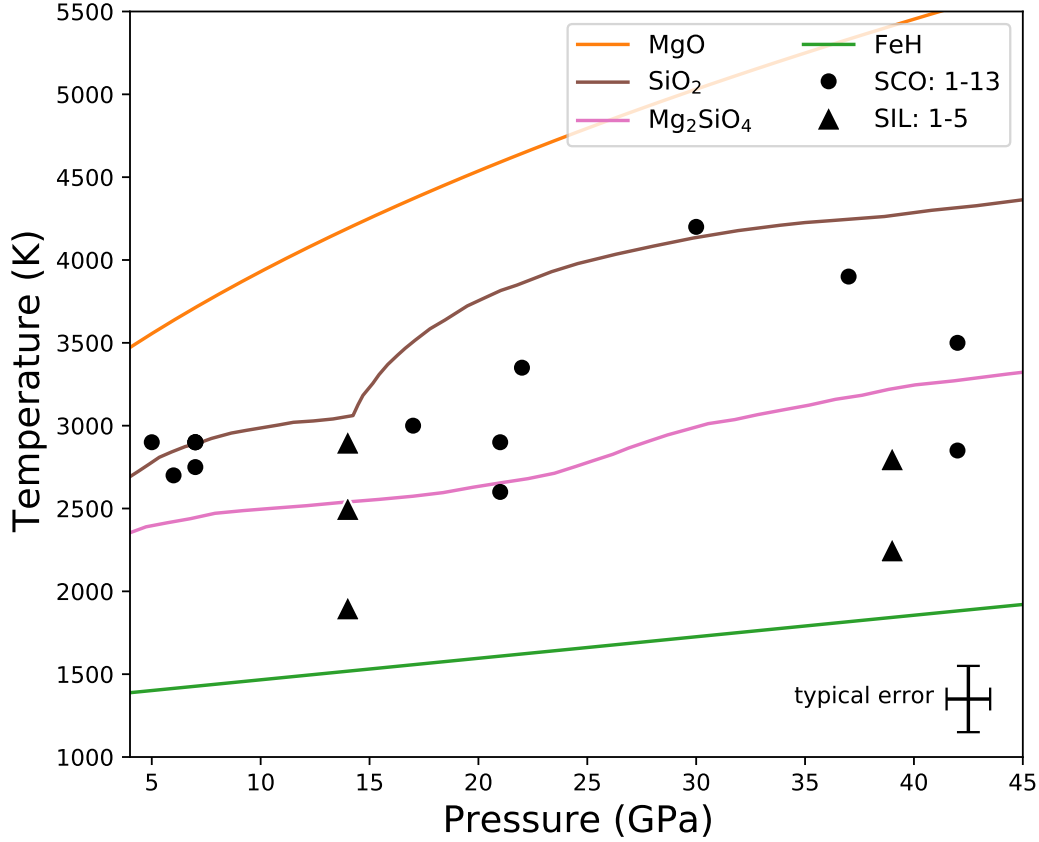
Figure 4.1: Pressure-temperature (*P-T*) conditions of the LHDAC experiments in this study (data points) shown with the melting curves of relevant materials: MgO: Kimura *et al.* (2017); SiO$_2$: Andrault *et al.* (2020); Mg$_2$SiO$_4$: Mosenfelder *et al.* (2007); and FeH$_x$: Sakamaki *et al.* (2009a). Most were near or above the melting temperature of FeO and FeH$_x$. All experiments were conducted above the melting temperature of hydrogen. Most experiments were near or below the melting temperature of silica. All olivine experiments except one likely underwent at least partial melting.

the observed volume is substantially lower than the expected unit-cell volume for fcc FeH$_x$ with $x \approx 1$ of 56.42 Å^3 at this pressure (Narygina *et al.*, 2011b), indicating substoichiometric alloying (FeH$_x$ with $x \approx 0.22$). Dhcp FeH$_x$ has a unit-cell volume of 46.32 Å^3 compared to the expected unit-cell volume of dhcp FeH$_x$ with $x \approx 1$ of $\sim$52.5 Å^3 (Hirao *et al.*, 2004) (but expanded by 9.6% compared to a H-free Fe dhcp
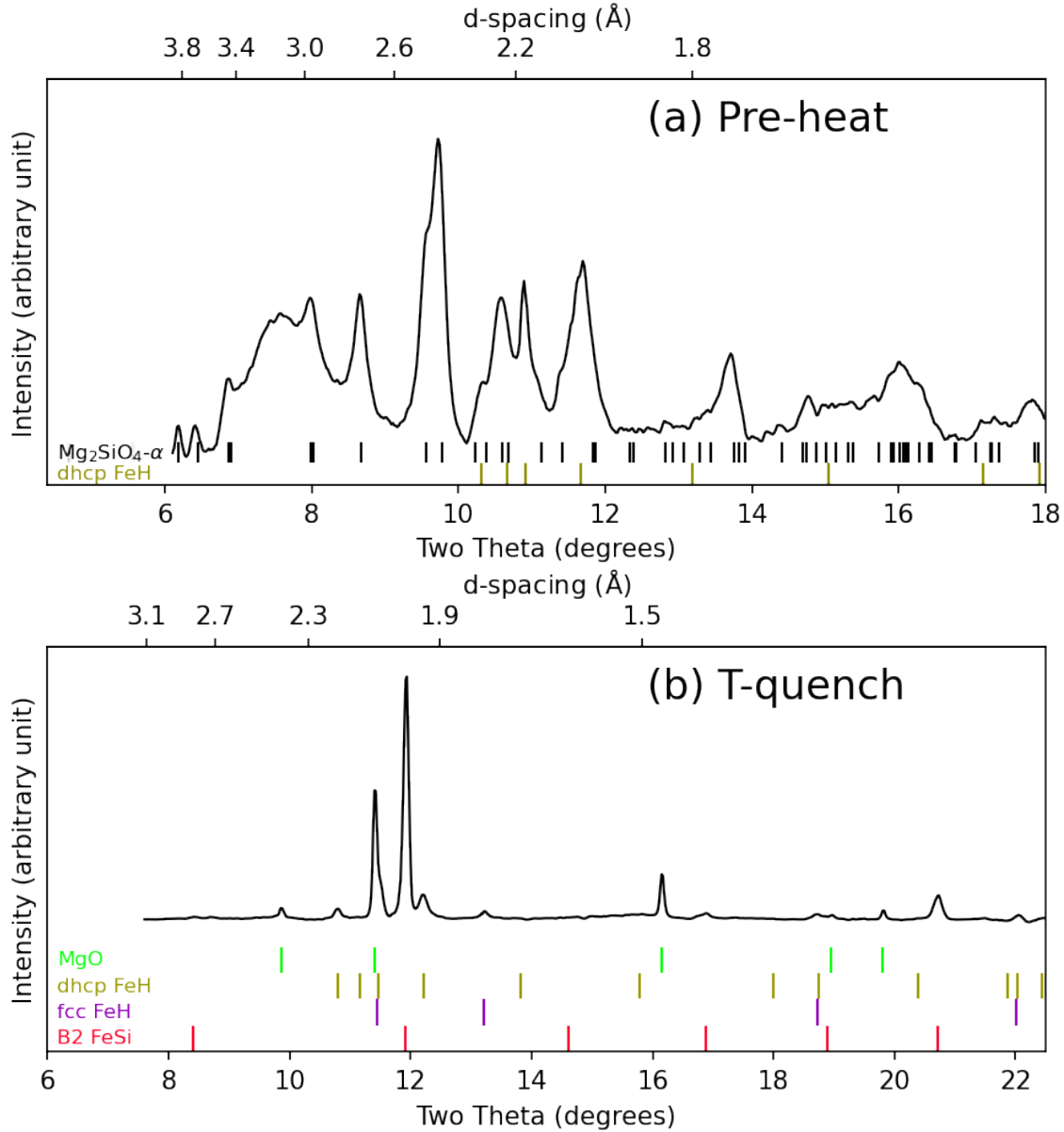
Figure 4.2: XRD patterns before and after heating a mixture of San Carlos Olivine and iron metal to 2900 K at 5 GPa in a hydrogen medium. Before heating the broadness of the olivine peaks may be attributed to the diffusion of H into the crystal structure similar to that seen by similar sized helium at similar pressures (Cherniak and Watson, 2012). After heating, olivine breaks down with Mg remaining oxidized as MgO, Fe and Si present as metals (FeH$_x$ and FeSi), and O released to the medium as H$_2$O (not seen due to weak scattering and peak overlap with fcc FeH.

structure (Jain *et al.*, 2013)), again indicating substoichiometric alloying ($x \approx 0.40$).

Upon decompression, Fe-H alloys are known to convert to H-free bcc Fe (Badding

et al., 1991) and I observe the same here. The bcc iron shows an anomalously small unit-cell parameter of 2.843±0.003 Å compared to the expected value of pure iron: 2.867 Å (Rotter and Smith, 1966). Because the bcc phase should be from the dehydration conversion of the fcc and the dhcp FeH_x phases observed at higher pressures, the observed small volume of the bcc phase implies that the small volumes of the fcc and dhcp FeH_x phases were due to a combination of substoichiometric alloying with hydrogen and some amount of Si incorperated in the structure. I attempted to confirm this with electron probe micro analyzer (EPMA) but the grain size of the mixture of Fe metal phases (bcc iron) and FeSi from the rapidly quenched melt was below the resolution of the system and the sample was lost preventing further exploration with TEM.

The only known Si bearing phase left in the post heating diffraction pattern is the B2 phase of Fe-Si alloy. Therefore all Si has been reduced to metal and alloyed with Fe metal which was mixed with the starting material. No iron-free separate silicon metal phase was observed. It should be noted that all Fe-Si alloy was in the B2 structure and the B20 structure was not observed in this pressure range as it was by Fischer *et al.* (2014). The unit-cell volume of the B2 phase is 22.30 $Å^3$, ~8.5% larger than the expected volume from the equation of state of B2 FeSi with Si/Fe = 1 (Fischer *et al.*, 2014). This could be either due to hydrogen incorporation or a lower concentration of silicon coupled with Fe larger atomic radius compared to Si (Slater, 1964). This expansion persists through decompression to 1 bar suggesting that the expansion is unlikely due to hydrogenation as Fe metal, as it is known to dehydrogenate below 3.5 GPa (Badding *et al.*, 1991). This is in agreement with the findings of Fu *et al.* (2022b) who found that B2 FeSi in a pure H medium does not take on a significant amount of H like pure Fe does. The volume at 8 GPa and 1 bar are both in close agreement with the V/Z (volume per atom in the unit cell) of the

$Fe_{0.73}Si_{0.27}$ DO_3 phase (Fischer *et al.*, 2014), implying this phase may have a similar composition. At 1 bar after decompression, I still observed B2 Fe-Si alloy alongside the aforementioned dehydrated bcc Fe.

After heating all Mg remains oxidized as MgO periclase. Upon decompression to 1 bar, the unit-cell volume of MgO was 74.66 ± 0.07 Å^3, in line with the known value of 74.71 Å^3 (Utsumi *et al.*, 1998), indicating no iron is present in the structure after heating consistent with experiments on (Mg,Fe)O in a hydrogen medium (chapter 3. The full chemical reaction can be written as:

$$(Mg_{0.9}Fe_{0.1})_2SiO_4 \text{ (m)}+1.8Fe \text{ (m)}+2.7H_2 \text{ (f)} \rightarrow FeSi \text{ (m)}+1.8MgO \text{ (s)}+FeH \text{ (m)}+2.2H_2O \text{ (f)},$$

$$(4.3)$$
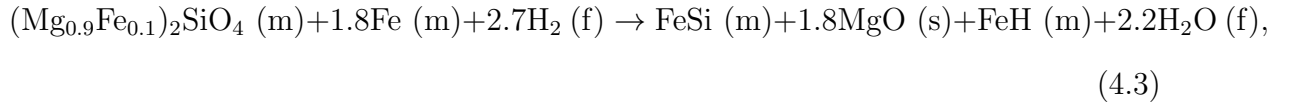
Where (m), (f), and (s) stand for melt, supercritical fluid, and solid respectively.

Spinel/Modified Spinel Stability Field

At 21 GPa after heating to 2550–3200 K (SCO-9), olivine again breaks down. As in the experiment at 5 GPa, all magnesium remains oxidized as MgO, while Si and Fe are reduced to metal to form an Fe-Si and Fe-H alloy. Like the experiment at 5 GPa FeH_x and FeSi form separate phases with the volume per iron atom of FeH_x consistent with $x = 1$ (Fig. 4.7). However, unlike at 5 GPa, FeSi is present not as the B2 structure, but rather hexagonal Fe_5Si_3 phase (Errandonea *et al.*, 2008). Fe_5Si_3 is known to decompose to FeSi and Fe_3Si above 18 GPa and 1300 K in the hydrogen free system (McGuire *et al.*, 2017). Therefore, it is possible H stabilizes this phase as found in (Fu *et al.*, 2022c). However, unlike Fu *et al.* (2022c) where hydrogenation of the hexagonal Fe_5Si_3 phase in a H medium results in significant volume expansion, the unit-cell volume of the Fe_5Si_3 phase in our study is very close to that expected from its equation of state predicted by Errandonea *et al.* (2008), implying a much much lower amount of hydrogen incorporation into the hexagonal structure of Fe_5Si_3
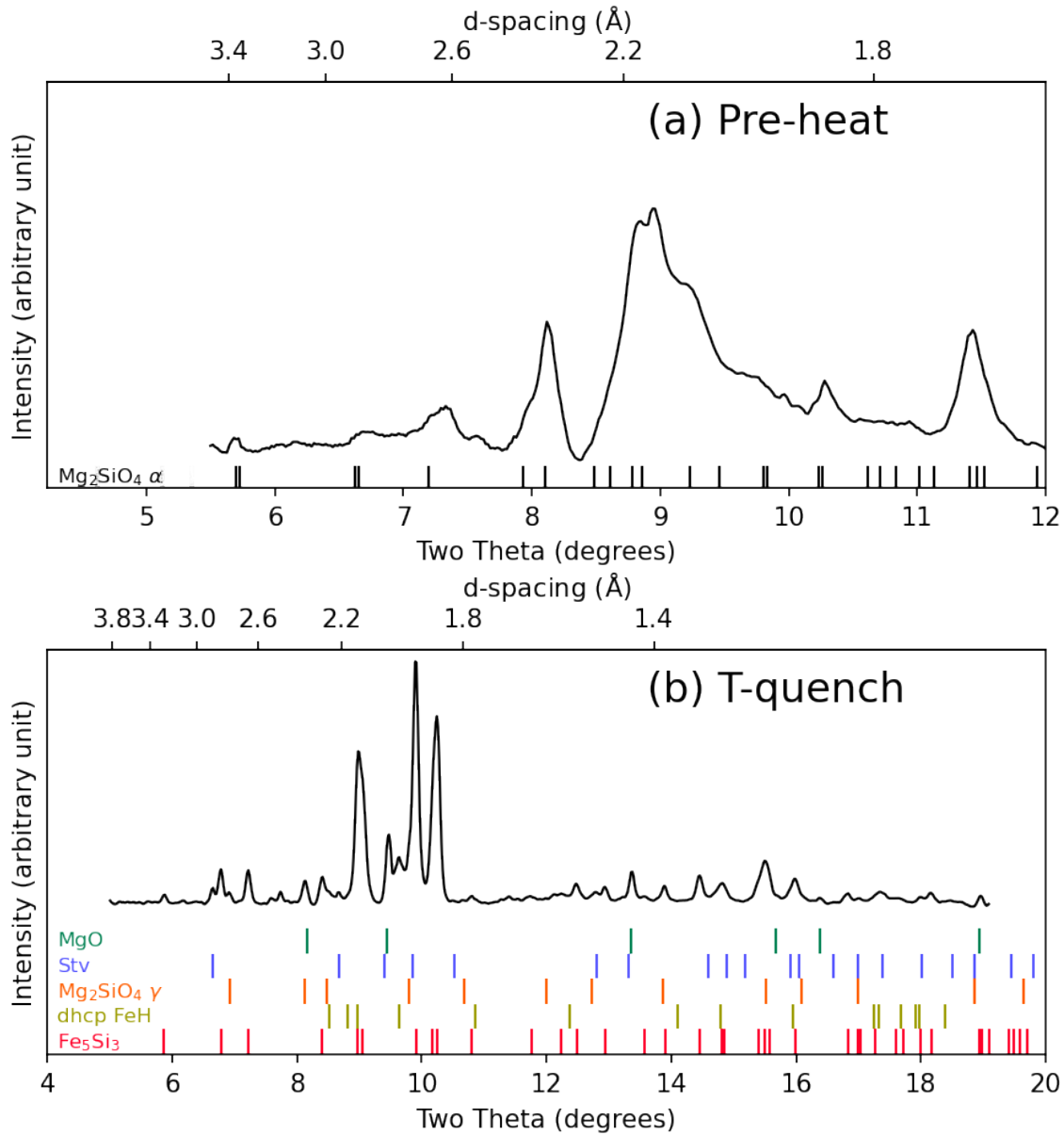
Figure 4.3: XRD patterns before and after heating a mixture of San Carlos Olivine and iron metal to 2550-3200K at 21 GPa.

when formed from the decomposition of silicates.

Some silicate remains as ringwoodite after heating (Fig. 4.3(b)), but these diffraction peaks are much weaker than Fe_5Si_3 and MgO. This observation is likely due to the fact that the temperature-quench diffraction patterns were measured away from the heating center as the diffraction intensity at the center was weak because the sam-
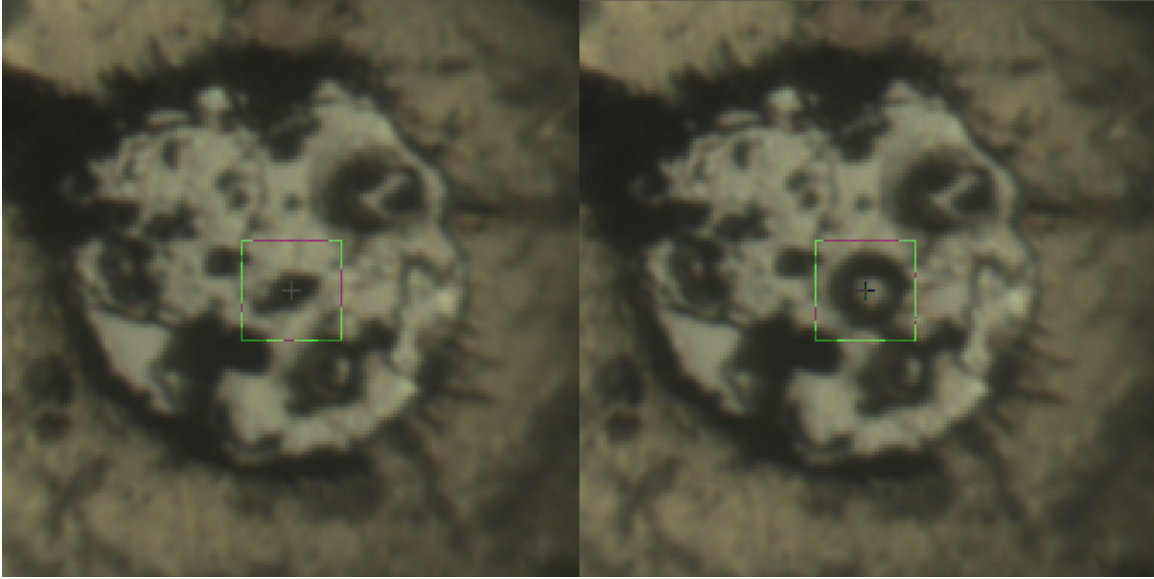
Figure 4.4: Images showing the sample before and after heating run SCO-9 to 3200K. Note the optical transparency in the center of the heated spot due to the molten sample being convected away by the melted H medium.

ple was molten and convected away by the hydrogen medium leaving little behind to measure (Fig. 4.4). The temperature during heating at the spot where diffraction patterns were measured was lower than the temperature at the heating center, which was the 2550–3200 K and therefore was not high enough for the melting olivine and subsequent decomposition of the silicate melt by hydrogen. However, the temperature at the off-centered spot may have been still high enough for the phase transition of olivine to ringwoodite.

Similarly, when heated to 2600–3500 K at 17 GPa, weak diffraction peaks of both ringwoodite and wadsleyite were observed after heating. In this case, the same products are seen as in the experiment at 21 GPa but with the addition of wadsleyite and fcc FeH_x, the latter likely due to excess mixed iron at the heating location. These results suggest the likely stable reaction between molten iron/silicate and H at intermediate pressures is:

$$3(Mg_{0.9}Fe_{0.1})_2SiO_4 \text{ (m)}+6.4Fe \text{ (m)}+7.6H_2 \text{ (f)} \rightarrow Fe_5Si_3 \text{ (m)}+5.4MgO \text{ (s)}+2FeH \text{ (m)}+6.6H_2O \text{ (f)},$$

$$(4.4)$$
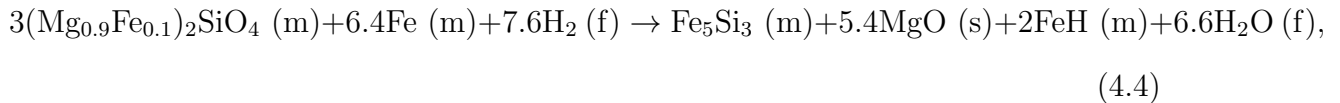
where m, f, and s stand for melt, fluid, and solid.

Perovskite Stability Field

When heated at 37 GPa (34 GPa after heating) and 2700 K, which is below the melting temperature of bridgmanite at this pressure, 4000 K (Shen and Lazor, 1995), the magnesium portion of the olivine transforms to bridgmanite and periclase similar to what is expected in the H-free system (Fig. 4.5b).

$$(Mg_{0.9}Fe_{0.1})_2SiO_4 \text{ (s)}+0.3H_2 \text{ (f)} \rightarrow MgSiO_3 \text{ (brd)}+0.8MgO \text{ (pc)}+0.2FeH \text{ (m)}+0.2H_2O \text{ (f)},$$

$$(4.5)$$
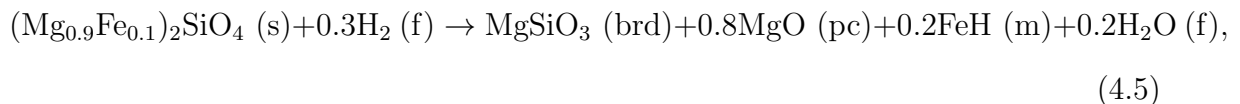
where brd and pc stand for bridgmanite and periclase (MgO). Bridgmanite has a unit-cell volume of $146.0 \pm 0.2 \text{Å}^3$ consistent with the expected volume of Mg-endmember silicate perovskite at this pressure, 146.1 Å^3 (Yeganeh-Haeri, 1994; Larson and Von Dreele, 1994), compared to the larger unit cell expected for iron containing $(Mg_{0.9}Fe_0.1)SiO_3$, 146.6 Å^3 (Mao *et al.*, 2015). Similarly, periclase has a unit-cell volume of 63.7 ± 0.3 Å^3, consistent with the expected volume of 64.0 Å^3 for endmember MgO (Dewaele *et al.*, 2000). Therefore, all Fe is removed from the silicate/oxide structures and reduced to FeH_x. The unit-cell volume of fcc FeH_x is 46.48 ± 0.06 Å^3, slightly higher than the expected value of 46.08 Å^3 for H/Fe = 1 (Narygina *et al.*, 2011b), indicating near stoichiometric alloying. It should be noted that when comparing unit cell volumes at high-pressure to glean compositional information, the error in the measured unit cell volume is not the only source of error. Our gold grains were placed at the edge of the sample chamber, tens of microns away from the heated

area of the sample. This was done to prevent heating of gold and subsequent alloying with H and sample materials. However, pressure gradients may exist across the sample chamber and the heating history of the medium may also lead to local pressure changes at the heating spot after heating which will not be measured by the pressure calibrant at the edge of the sample chamber. These discrepancies can be on the order of a GPa and introduce an additional error of approximately 0.2–0.5% when comparing unit cell volumes at a given pressure.

I then heated the synthesized bridgmanite to above melting temperature (4350 K) at 37 GPa. I found that bridgmanite dissociates upon melting in a hydrogen medium. At high-temperature, only diffraction peaks of MgO are visible because all other sample components were molten. While heating, the solid MgO component remains stable, but all other oxidized elements are reduced by H and decompose. The SiO_2 component reacts with iron and hydrogen to form B2 FeSi (Fig. 4.5c) releasing O into the H medium where it likely reacts to form H_2O. The anvils failed before Raman measurements could be conducted to confirm the presence of water. In order to isolate the impact of Si reduction on water formation, I conducted separate experiments where Raman was successfully conducted (see the next section). Some bridgmanite peaks were observed after melting, but their intensities are weak (Figs 4.5 (c) vs. 4.5 (b)). X-ray mapping (Fig. 4.6) shows the anti-correlation between B2 FeSi (reaction product) and silicate phases, showing that bridgmanite is mostly formed in lower temperature areas that have not experienced melting. Therefore, the observation above the melting temperature can be summarized as:

$$MgSiO_3 \text{ (m)} + Fe \text{ (m)} + 2H_2 \text{ (f)} \rightarrow MgO \text{ (s)} + FeSi \text{ (m)} + 2H_2O \text{ (f)}. \qquad (4.6)$$

The volume of B2 FeSi is consistent at high pressure and through decompression

with the volumes reported for the same phase for Si/Fe = 1 Fischer *et al.* (2014), suggesting that it is pure FeSi with little incorporation of H, consistent with the observations by Fu *et al.* (2022b) that this phase cannot take in large amounts of H like other metal phases can. At 1 bar, the unit-cell volume of B2 FeSi is 21.45 ± 0.02 Å^3, slightly expanded from the value of 21.30 Å^3 reported by Fischer *et al.* (2014). This is likely because there is a slight superabundance of Fe ($Fe_x Si_{1-x}$ $0.5 < x < 0.67$; see Fig. 4.8). By contrast, bcc Fe has a unit-cell parameter of 2.8666 ± 0.0001 Å^3 in agreement with the known value of pure Fe, 2.867 Å (Rotter and Smith, 1966), suggesting no Si incorporation in FeH_x at higher pressures.

The unit cell volumes of the remnant oxidized phases also tell an interesting story. MgO periclase has a unit cell volume of 74.70 ± 0.02Å^3, in agreement with the value of 74.71 for endmember MgO Fei and Mao (1994), demonstrating that the MgO formed in this experiment did not contain Fe in its crystal structure. By contrast, the unit cell volume of the remnant perovskite phase is 163.01 ± 0.05Å^3, expanded from the unit cell volume of endmember $MgSiO_3$ perovskite: 162.49Å^3 (Mao *et al.*, 1991). The volume is marginally larger than the expected volume for $(Mg_{0.9}, Fe0.1)SiO_3$ (the approximate Fe content of San Carlos Olivine, the starting material) of 162.79 Å^3. Utilizing a linear interpolation between the unit cell volumes for 10 and 20 mol% Fe from Mao *et al.* (1991) gives an approximate composition of $(Mg_{0.86}, Fe_{0.14})SiO_3$. The partitioning of all ferrous iron into bridgmanite and none into ferropericlase is in stark contrast to the H_2 free system where Fe preferentially partitions into ferropericlase (Kobayashi *et al.*, 2005; Narygina *et al.*, 2011a; Nakajima *et al.*, 2012) (and also the melt-free measurements above where both periclase and perovskite appear to be the Mg endmember).

4.4.2 SiO_2

In all experiments above, Mg has been a bystander forming MgO and never seeming to chemically interact with H or metals. For this reason, I hypothesized that the formation of Fe-Si alloys was a 2 step process. First, silicates break down to form silica and oxides, then the Si in silica is reduced to metal by H to form an alloy with Fe while the released O reacts with the H medium to form H_2O. To test this I conducted experiments on a mixture of silica and Fe in a H medium at similar pressures to the olivine experiments. In addition to in-situ XRD measurements, I also measured Raman spectra to confirm the presence of water after heating.

At 13 GPa after one heating event at 2500–3300 K (SIL-2), SiO_2 partially breaks down to alloy with the mixed Fe form B2 FeSi (Fig. 4.9), implying the following reaction:

$$SiO_2 \text{ (s)} + Fe \text{ (m)} + 2H_2 \text{ (f)} \rightarrow FeSi \text{ (m)} + 2H_2O \text{ (f)} \qquad (4.7)$$

Unreacted silica crystallizes to mainly form stishovite but a small amount of coesite is also present despite the pressure being slightly above its stability field. The O released by the reduction of Si^{4+} reacts with the H_2 medium to form H_2O which I detected via Raman spectroscopy (Fig. 4.10). The amount of unreacted silica is likely due to the fact that unlike most silicate samples, the temperature was not sufficiently high for significant melting for this sample. B2 FeSi was still observed, indicating that this reaction proceeds in the solid state, but the reaction is much slower than in melting experiments where all silica was consumed in one heating event. Although with a larger uncertainty because of very weak diffraction intensity of FeH_x in this case, excess Fe alloys with the H medium as fcc FeH_x with a unit-cell volume of 50.7±0.2 Å^3, 2–3% larger than expected for H/Fe = 1. In other experiments ranging from 14–39 GPa and 1900–3800 K, similar results were seen. Silica was never

fully eliminated but at higher pressures only stishovite was formed (and no coesite). The contrast between equations 4.2 and 4.4.2 should be noted. In the experiments by Shinozaki *et al.* (2014), no Fe was present and after the breakdown of SiO_2, Si maintained its oxidation state of 4^+ in SiH_4, whereas in this work Si was reduced to metal and alloyed with Fe to form FeSi.

4.5 Discussion

In all samples, when melting was induced (as measured by the temperature exceeding that of its respective known melting curve), the silicate phase breaks down in the presence of hydrogen. In one run, stable heating was achieved below the melting temperature of bridgmanite. In this case, bridgmanite remained stable (Fig. 4.5). However, bridgmanite broke down when heated again above its melting temperature. These results imply that molten iron-magnesium silicates are unstable in the presence of hot dense hydrogen fluid at pressures of 5–42 GPa, while it remains possible that solid silicates remain stable under a H atmosphere as observed by Shinozaki *et al.* (2012). This could imply that as a magma ocean cools and crystallization becomes dominant the reactions discussed in this work and their implications (such as Si loss from the mantle to the core) may halt.

When the silicate phases break down, the observed phases in XRD and Raman spectroscopy show the unique behavior of every element in the Mg-Fe-Si-O-H system, as well as the relative phase stability at a variety of *P-T* conditions. All Fe present in the starting material is likely reduced to metal (no remaining oxidized Fe is seen) while Mg remains oxidized as MgO periclase, consistent with the results of (Mg,Fe)O experiments conducted under H in Chapter 3. Si^{4+} originally present in the silicate phase also reduces to metal (Si^0). This Si metal alloys with Fe to form B2 FeSi with little to no hydrogen incorporation, consistent with the results of Fu *et al.* (2022b).

At pressures of 17–22 GPa an additional Fe-Si alloy was seen–hexagonal Fe_5Si_3–again with little to no incorporation of H (in contrast to Fu *et al.* (2022c) who found $\sim$27 mol% H in this crystal structure). The fact that separate phases form for Fe-Si alloys (hexagonal Fe_5Si_3 and B2 FeSi) and Fe-H alloys (dhcp FeH_x and fcc FeH_x) suggests that H and Si mutually inhibit each other in Fe alloys. However, for each alloy phase observed there is some deviation from the expected unit-cell volumes of pure stoichiometric phases, suggesting it is possible that there is a spectrum of compositions and the crystal structure for a given composition is determined by the relative quantities of Fe, Si, and H. The O that was originally bound to Fe^{2+} and Si^{4+} is released to the H-medium where it reacts with H to form H_2O with the reduction of Si creating twice as much H_2O as the reduction of Fe due to it releasing two O atoms.

For Earth-sized bodies, previous studies have estimated 0.03–0.05 GPa for the surface pressure of a nebular atmosphere (Stökl *et al.*, 2015; Ikoma and Genda, 2006), which is approximately two orders of magnitude lower than the pressures I studied here. The critical point for hydrogen is 0.0013 GPa and 33 K and hydrogen remains molecular supercritical fluid at least up to 100 GPa at planetary interior related temperatures ($\geq$ 1000 K) (Cheng *et al.*, 2020). At the conditions mentioned above for Earth-size planets, hydrogen would be a supercritical fluid which may remain the same to the *P-T* conditions I studied here. Although a Frenkel line–the line divides the stability field of a supercritical fluid into more and less "rigid" fluids– may exist between the condition expected for Earth-size body and the conditions covered in our study (Trachenko *et al.*, 2014), H will be still molecular fluid and thus may still interact with molten silicates in a similar way. However, an important difference is that FeH_x would unlikely form at such a low pressure for Earth and it is more likely that Fe metal forms. While this difference may limit the ingassing of H through Fe

65

reduction, H_2O would be still produced by the reduction of Fe and Si in the silicate magma and some will partition into the magma ocean. At 0.1 GPa, solubility of H_2O may be approximately 3 times higher than H_2 in magma (Moore *et al.*, 1995; Hirschmann *et al.*, 2012). Therefore, water produced by the reduction of Fe and Si by primordial hydrogen may play an important role for the ingassing of H in the case of Earth-size body (Hirschmann *et al.*, 2012). This production and ingassing of H_2O by H-magma interaction could also serve as an important deep reservoir of nebular hydrogen like is seen in Earth (Genda and Ikoma, 2008; Hallis *et al.*, 2015; Wu *et al.*, 2018). However, this does not rule out the possibility of H_2 at depth in a magma ocean (possibly through physical mixing) (Olson and Sharp, 2018) experiencing the the same *P-T* conditions as the experiments presented in this work.

The physical mixing and chemical reaction are especially pertinent for super-Earth's which may ingas at least $10\times$ more H than their Earth sized counterparts (Olson and Sharp, 2018). This difference in nebular H ingassing between Earth-sized planet's and super-Earth's may have profound effects on their respective chemical partitioning. While Earth-sized planets may have an Earth-like interior mineralogy, structure, and dynamics, super-Earth's may significantly differ in all aspects. They have cores with far more light elements such as ingassed H or Si from the reduction of mantle silicates. The mantle of super Earths mantles with significant quantities of endogenic nebular-H derived water, and be enriched in MgO due to the loss of Si to the core. The water produced by the reduction of oxidized phases may also enhance mantle convection because H_2O is known to decrease viscosity (Karato and Wu, 1993). If the endogenically produced water is outgassed it could form a long-lived H_2O dominated atmosphere (Kite and Schaefer, 2021) (or hydrosphere if the temperature is sufficiently low).

As planetary bodies grow larger than super-Earth's ($\sim 2.7_{\oplus}$), they will start to

rapidly accrete nebular gas into a thick H-dominated atmosphere. At the base of this atmosphere, there will exist a high P-T interface between the growing H-dominated envelope and the silicate magma ocean. At this interface, the reactions presented within this work could enhance the solubility of H in the magma ocean beyond what is possible through physical mixing and dissolution. Firstly, when olivine melt breaks down, the elements that had been bound to O reduce releasing and forming large amounts of water by chemical reaction with the surrounding O. H_2O is more soluble than H_2 in magma at this pressure (Hirschmann *et al.*, 2012) so this conversion will enhance the solubility of the atmosphere in the magma ocean. Secondly, H can be directly sequestered as an alloy component with existing and newly formed metallic iron. These chemical enhancements to the solubility of H in silicate melt support the hypothesis that the radius cliff is a result of growing planets preferentially partitioning additional acquired nebular gas into the interior rather than the atmosphere thus disrupting their radial growth (Kite *et al.*, 2019).

Beyond the enhanced solubility of H in the melt, the chemical reactions presented in this work could significantly alter the structure, chemical partitioning, and dynamics of growing sub-Neptunes. Not only does H alloy with existing Fe to form FeH_x, but it also reduces previously oxidized Fe to form additional metal. H reduces Fe in silicates (equations 4.3, 4.4, 4.6) and oxides (Chapter 3). This reduction of Fe could serve to raise the Mg/Fe ratio of the mantle and grow the core mass fraction (CMF). Similarly, the reduction of Si by H will raise the Mg/Si ratio of the mantle. The reduction of Si is particularly interesting as it shows an important shift in the behavior of Si from lithophilic to siderophilic if the conditions are sufficiently reducing. This lithophilic behavior and alloying with Fe provides an important mechanism for the reduction of mantle silicon and transport to the core along with the sinking metal alloys to enrich the cores of sub-Neptunes in Si (as well as in H from the alloying of

Fe with H (Badding *et al.*, 1991; Narygina *et al.*, 2011b; Pépin *et al.*, 2014)).

After losing Fe and Si, the remaining mantle will be enriched in both H_2O and MgO. MgO has a higher melting temperature than magnesium silicate by about 1000 K so after the loss of silicon, crystallization of MgO out of the magma ocean may be expedited relative to the magma ocean timescale with the original composition. However, H_2O is also known to lower the melting temperature (Litasov and Ohtani, 2002) and viscosity (Karato and Wu, 1993) thus prolonging the magma ocean phase and enhancing convection.

The endogenic production of H_2O in the mantle could also serve as an important deep reservoir of nebular hydrogen as is seen in Earth (Genda and Ikoma, 2008; Hallis *et al.*, 2015; Wu *et al.*, 2018). For each mole of magnesium silicate decomposed to water, metal, and periclase, 2 moles of H_2 are consumed to form H_2O (eq. 4.3). For each mole of Fe^{2+} reduced to metal, another mole of H_2 is converted to H_2O. Although H_2O and H_2 have been reported to be immiscible with each other up to 3 GPa and 1500 K (Bali *et al.*, 2013a), a density functional theory (DFT) study suggested miscibility between H_2 and H_2O at 2–70 GPa and 1000–6000 K (Soubiran and Militzer, 2015a). Therefore, H_2O may partition into both H envelope and magma ocean of a sub-Neptune. The partition coefficient of H_2O is important to measure in the future studies to understand the amount of hydrogen ingassed to the interiors of sub-Neptunes as H_2O. Water can partition between silicate melt and metallic iron liquid at high *P-T* and existing studies support strong partitioning of H to metallic Fe (Tagawa *et al.*, 2021; Li *et al.*, 2020a). Therefore, a significant fraction of H_2O can further ingas and be stored in the metallic part of sub-Neptunes' cores. The fraction of H_2O that partitions into H atmosphere will be important for on-going effort for measuring and analyzing the composition of sub-Neptunes' atmospheres.

It has also been shown that some super-Earths may be sub-Neptunes that lost

their primordial envelope, rather than overgrown terrestrial planets (Owen and Wu, 2013; Schlichting, 2014; Bean *et al.*, 2021). On these planets, the large amount of H_2O generated by the H-magma interface by the reactions presented in the work during their sub-Neptune magma ocean phase may outgas to form a detectable water-rich secondary atmosphere (Kite *et al.*, 2020). These long-lived water-rich atmospheres could give a detectable signature to distinguish between super-Earth planets that formed from sub-Neptunes that have undergone massive gas-loss versus ones that formed without significant nebular envelopes.

4.6 Acknowledgments

Figure 4.5: X-ray diffraction patterns showing San Carlos Olivine before (a) and after heating to 2700 K (b, solid) and 4350 K (c, melt) at 37 GPa in a hydrogen medium. After heating to 2700 K all bridgmanite remains intact, while after heating to 4350 K and melting bridgmanite it breaks down and silicon is reduced to form B2 FeSi.
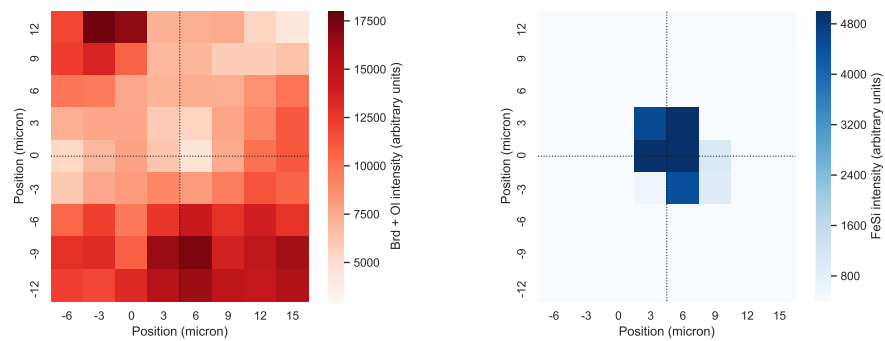
Figure 4.6: 2-D maps of integrated diffraction peak intensity around the heated spot after heating sample SCO-11 to 3300-4500 K. The left panel shows the integrated diffraction intensity of both unreacted San Carlos Olivine and Mg-perovskite. The right panel shows the integrated intensity of B2 FeSi. The anti-corrilation between the two at the heating spot center shows that when melted silicates break down and Si is reduced to form FeSi.
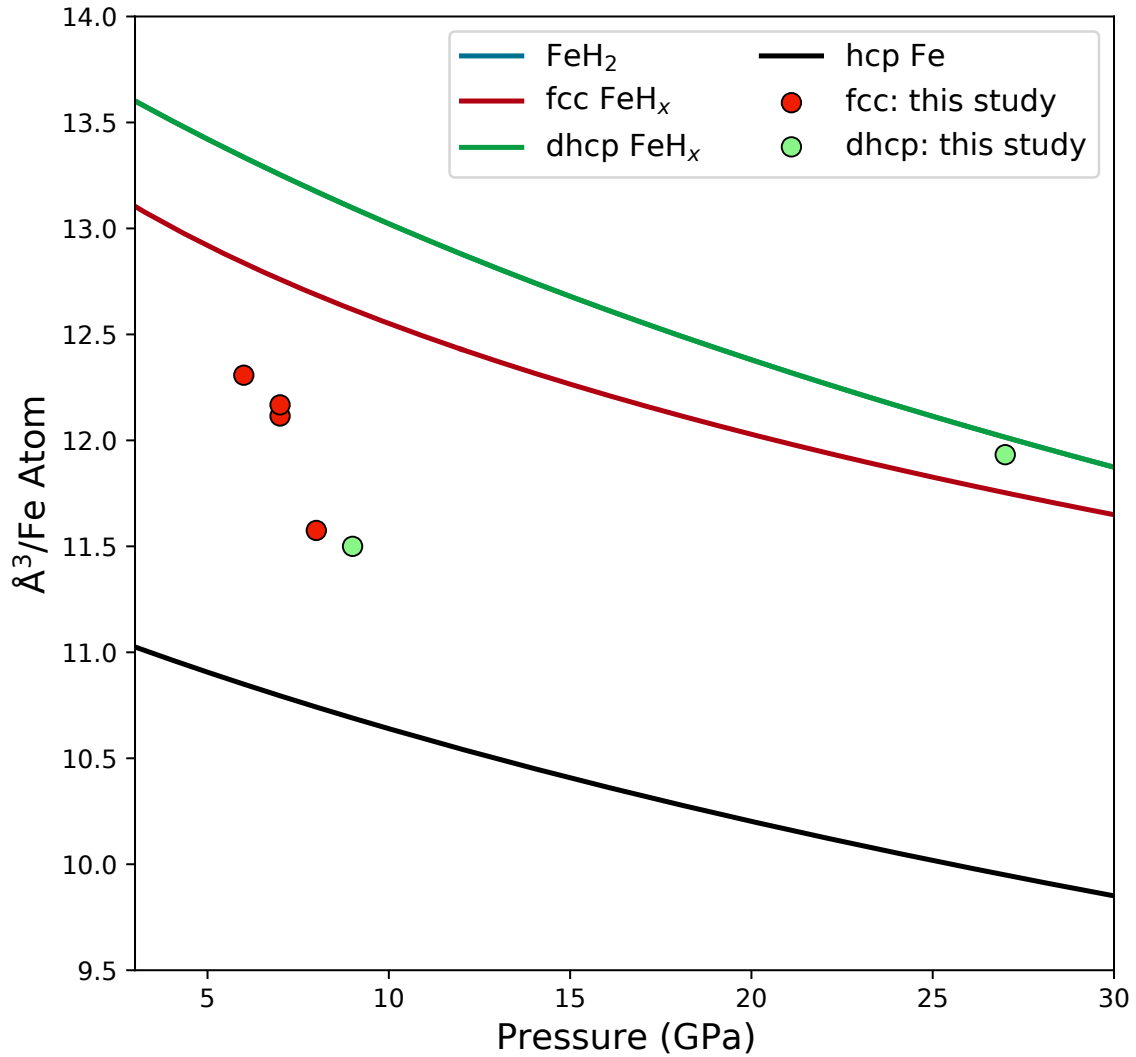
Figure 4.7: Pressure-volume data for Iron-hydrogen alloys formed in these experiments. At pressures above 10 GPa, the volumes of alloys appear to align well with stoichiometric fcc and dhcp FeH (Badding *et al.*, 1991; Narygina *et al.*, 2011b). However at lower pressures volumes deviate with some alloys showing lower H content (FeH$_x$ x<1) and some showing volumes near that of FeH$_2$ (Pépin *et al.*, 2014)
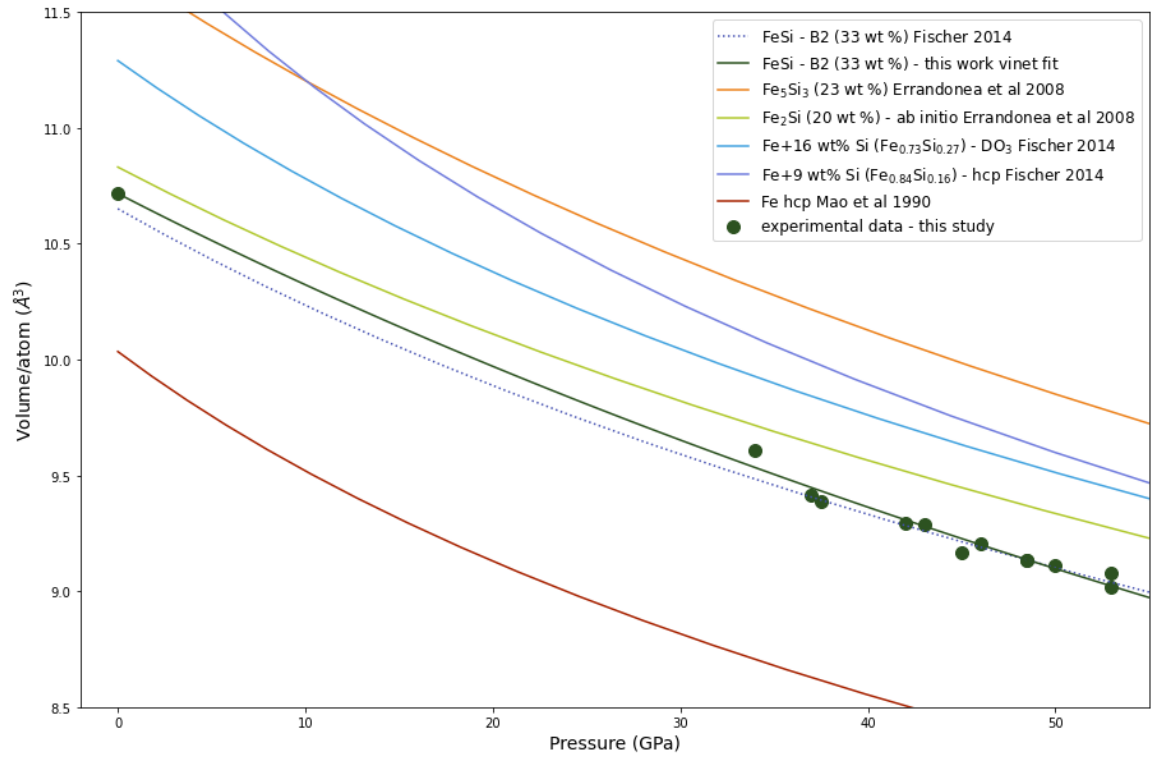
Figure 4.8: P-V data for FeSi synthesized from bridgmanite mixed with iron at 35 GPa and heated above 4000K. The volumes align well with the reported values from Fischer *et al.* (2014).
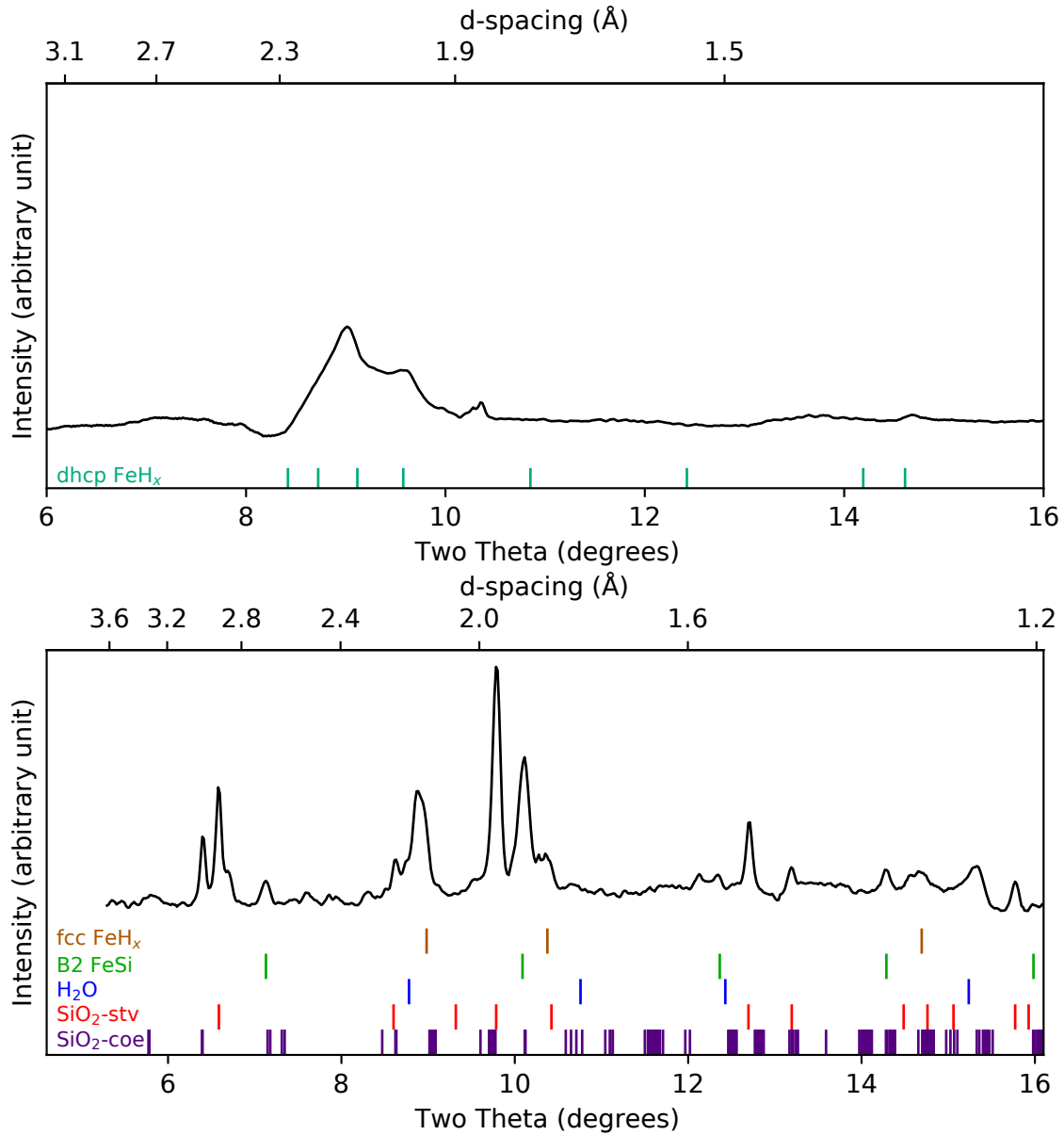
Figure 4.9: top: Pre-heating CRD pattern of Fe that has been hydrogenated in the DHCP structure and amorphous silica.
bottom: XRD diffraction pattern showing the formation of B2 FeSi (green) after heating to 2500-3300K (below the melting temperature) at 13 GPa.
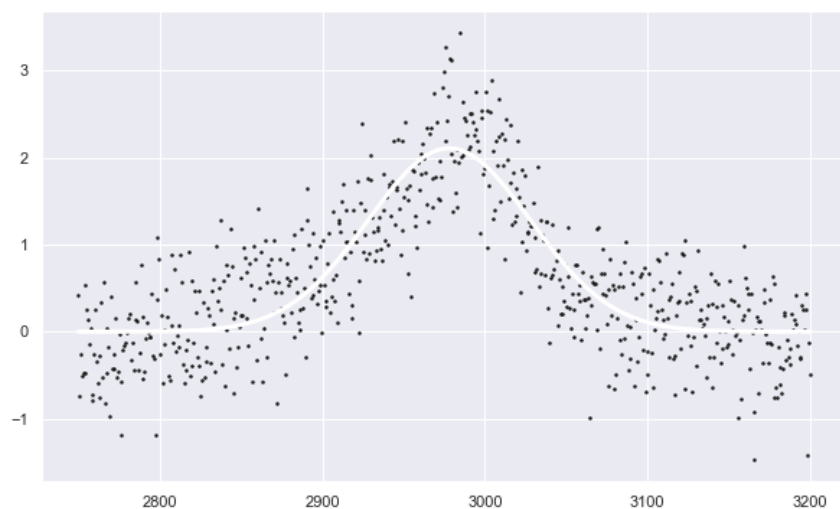
Figure 4.10: A raman spectrum showing OH stretching at high pressure after heating in sample SIL-2. The spectra were collected after laser heating with the Raman system at GSECARS (Holtgrewe *et al.*, 2019) utilizing the 532nm excitation laser.
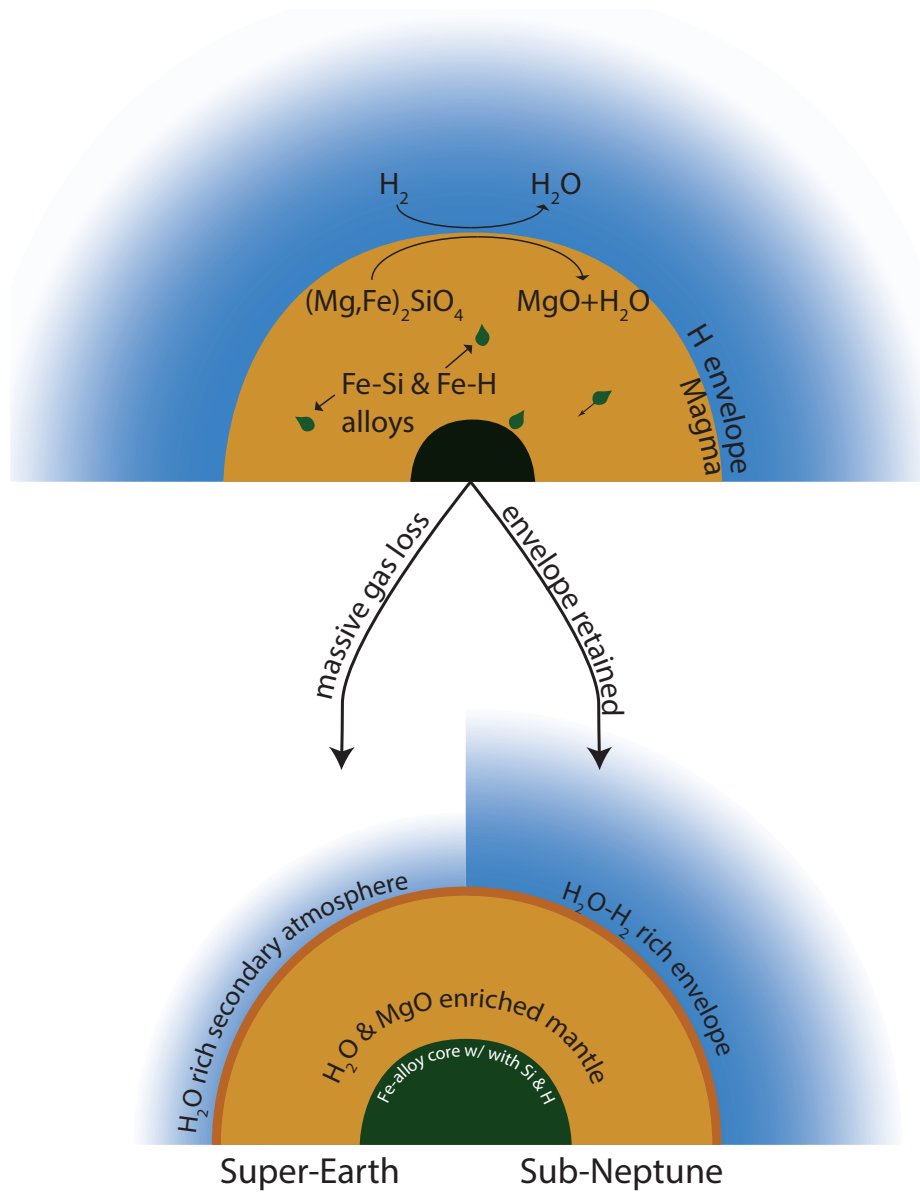
Figure 4.11: Illustration of how a high-pressure H-magma ocean interface may alter the evolution of the core, mantle, and atmosphere of a planet.

Chapter 5

PHASE STABILITY AND CHEMICAL REACTIONS OF FAYALITE UNDER A HYDROGEN ATMOSPHERE AT PRESSURES UP TO 21 GPA

5.1   Abstract

Hydrogen is the main constituant of stars, the disks from which planets accrete, and the atmospheres of large planets (R>1.75R$_\oplus$). In the previous chapters I have shown the interactions between hydrogen and iron/magnesium oxides and silicates along with metallic iron (chapters 3 and 4). In both of these works, Mg remains oxidized as MgO after laser-heating in a H medium. In this work I present experiments in the pulsed laser-heated diamond exploring the phase stability and chemical reactions of molten Fayalite (Fe$_2$SiO$_4$) in a medium of hot dense hydrogen. I find that when melted (2250-4500K) in a hydrogen medium fayalite completely breaks down. At pressures above 10 GPa, Si remains oxidized as SiO$_2$ and Fe reduces to form FeH$_x$ with x∼1. Below 10 GPa, Si appears to also be reduced to metal, and alloys with Fe to form B2 FeSi. This may be attributable to a change in the miscibility behavior in the H$_2$-H$_2$O system below 10 GPa. Additionally, below 10 GPa, FeH$_x$ appears to take in more than twice as much hydrogen ($\frac{H}{Fe}$)=2.2-2.4) than previously reported. This observation of superstoichiometric FeH$_x$ at low pressures could have implications for the atmosphere/magma ocean interactions on growing large planets.

5.2   Introduction

Hydrogen is the fundamental building block of the universe. Consisting of simply a proton and an electron (and occasionally a neutron) it is the main constituent

of stars around which planetary systems form. Planets are formed from the same disc of gas and dust that collapse to form stars which is thus also rich in hydrogen (Richter *et al.*, 2002). All planetary embryos are born in this hydrogen-rich disk, and some grow large enough to attract hydrogen-rich primary atmospheres (i.e. gas giants and sub-Neptunes) or ingas large amounts of hydrogen (such as super-Earths) (Olson and Sharp, 2018). Hydrogen is extremely reducing (Bergh, 1965; Luidold and Antrekowitsch, 2007) and may significantly alter the structure, composition, and mineralogy of planets where it interfaces with refractory planetary materials.

As planets grow in the protoplanetary disc, they may interface with nebular hydrogen gas. Smaller planets (Earth-sized and smaller) may attract some quantity of nebular gas, but as they grow beyond the scale of super-Earths into subneptunes (~ 1.75 R$_\oplus$–3.5 R$_\oplus$), they will begin to accrete large amounts of nebular gas (if they form before the dispersal of the gaseous disc at 10^6–10^7 years (Haisch Jr *et al.*, 2001; Jayawardhana *et al.*, 2006)). At the base of these thick H-dominated envelopes there will be a high-P interface with the rocky material below (Rogers *et al.*, 2011). At this high pressure-temperature interface interactions between the envelope and hot (possibly molten) silicate layer below may have a significant impact on the structure and evolution of the growing planet (Hirschmann *et al.*, 2012; Kite *et al.*, 2019, 2020; Kite and Schaefer, 2021)

Despite the importance of hydrogen in planetary processes, hydrogen has remained understudied in experimental mineral physics. Most previous studies have either utilized impure hydrogen sources (such as H_2O or paraffin) which contain other chemically active elements or were unable to be conducted at high temperature due to the experimental challanges associated with working with hydrogen (chapter 2.3). Some studies have circumvented these challenges by using a double capsule technique to supply molecular hydrogen while keeping other elements segregated (e.g.

Hirschmann *et al.*, 2012), while others have utilized recent technical advances to overcome the experimental challenges of working with pure H_2 in the diamond-anvil cell at high temperature (e.g. Pépin *et al.*, 2014). Experimental studies have found that at pressures up to 67 GPa Fe alloys with H to form FeH_x with $x \approx 1$ in the dhcp (double hexagonal close-packed) structure at low temperatures and the fcc (face-centered cubic) structure at higher temperatures (Badding *et al.*, 1991; Narygina *et al.*, 2011b; Pépin *et al.*, 2014). At pressures from 67–86 GPa, the solubility of H in Fe increases to FeH_x with x$\approx$2 and then increases again at 86 GPa to FeH_x with $x \approx 3$. These alloys may be important for planetary cores such as Earth's where H has been proposed as a possible light element alloy component (Kronig *et al.*, 1946; Stevenson, 1977; Fukai and Akimoto, 1983; Okuchi, 1997; Narygina *et al.*, 2011b).

Alloying behavior is not the only experimentally observed interaction between Fe and H. In chapter 3, it was shown that both Fe^{2+} and Fe^{3+} can be reduced by H forming FeH_x. Iron oxides (e.g. Fe_2O_3) were completely reduced to metal releasing water in the process. By contrast MgO was stable and unaffected by hydrogen (although it did react with the water produced by the reduction of Fe to form brucite). While these reactions show important chemical reactions and phase stability for the Mg-Fe-O-H system, real planets are dominated by silicates, not oxides.

A previous study found that magnesium silicate is stable when heated below its melting temperature in hydrogen (Shinozaki *et al.*, 2012). However, as shown in Chapter 4, when melted, San Carlos olivine breaks down to form MgO while Fe and Si are reduced to metal releasing water. San Carlos olivine has a composition of $(Mg_{0.88}, Fe_{0.12})_2SiO_4$, which should be enough Fe to achieve stable coupling with the near-IR laser utilized in pulsed laser-heating. However, in actuality this was not the case (see 2.3.2 for a more in depth discussion) so metal Fe was mixed to facilitate laser heating (as well as to represent free metallic Fe that may be present in a magma

Run ID	S.M.	P	T	H.E.	Method	Result
FAY-1	Fay+H_2	6	2900	1	XRD+Raman	FeH_x + FeSi + BCC Metal
FAY-2	Fay+H_2	6	2225	1	XRD+Raman	FeH_x + FeSi + BCC Metal
FAY-3	Fay+H_2	12	3000	1	XRD+Raman	FeH_x + SiO_2
FAY-4	Fay+H_2	11	2550-2750	2	XRD+Raman	FeH_x + SiO_2
FAY-5	Fay+H_2	21	2500-4500	2	XRD+Raman	FeH_x + SiO_2

Table 5.1: "result" - is after T-quench of final heating cycle for each heating spot. "S.M." - sample material. "H.E." - number of heating events (as defined in methods). Temperature errors are estimated to be ± 250 K and when a range is given it represents the change in measured temperature over time in a single heating event. Pressure errors are estimated to be ± 1 GPa.

ocean). Given that all oxidized Fe in silicates and oxides is stripped off and reduced by H but Mg seems to be unaffected (chapters 3 and 4), it is possible that Fe endmember olivine, fayalite, may be able to be completely reduced to metal (releasing water) by H.

In this work, I conduct experiments on the interactions between molten fayalite and pure molecular hydrogen utilizing the pulsed laser-heated diamond-anvil cell. Experiments were conducted in 3 pressure ranges, corresponding to the three phases in the H-free fayalite phase diagram. 6 GPa experiments fall within the stability field of fayalite, 11–12 GPa experiments within the spinel structure stability field, and 21 GPa experiments exceed the pressure where fayalite decomposes to FeO and SiO_2 (Ohtani, 1979). Samples were analyzed with in-situ X-ray diffraction, in-situ Raman spectroscopy, and electron microscopy to determine chemical reactions and phase stability. The observed phase relations and chemical reactions are discussed in the context of ongoing efforts in mineral physics and their implications for planetary science.

5.3 Materials and Methods

5.3.1 Sample Preparation

Natural fayalite (Smithsonian: R 3517 00: Rockport, Massachutes) was ground to a powder (grain size $< 10 \, \mu$m) using an alumina morter and pestel, then compressed into foils $\sim$10 μm thick using diamond anvils with a $500 \, \mu$m diameter culet. Rhenium was indented by diamond anvils with $200 \, \mu$m diameter culets and then a central circle with a diameter of $125 \, \mu$m was laser-milled out to form a chamber in which to place the sample foil. To prevent hydrogen diffusion into the gasket material, they were coated with $\sim$800 Å of gold before being placed back into the diamond anvil cells. The sample foils were placed in the center of the sample chamber, and pressure calibrants (ruby and gold) placed away from the foil at the edge of the sample chamber. The cells were then placed in a Sanchez GLS 1500 gas loading system, loaded with 1000–1500 bar of pure H_2, closed, and compressed to 10–20 GPa at 300 K. During the initial compression, I monitored the pressure using the ruby fluorescence pressure scale (Piermarini *et al.*, 1975).

5.3.2 Synchrotron Experiments

I performed X-ray diffraction (XRD) experiments in the double-sided pulsed laser-heated diamond-anvil cell (LHDAC) at the Advanced Photon Source (APS) GeoSoilEnviroConsortium for Advanced Radiation Sources (GSECARS) sector beamline 13-IDD. Monochromatic X-ray beams of wavelength 0.4133 Å or 0.3344 Å were coaxially aligned with near-infrared laser-beams and focused on the sample in the LHDAC for in-situ laser heating and XRD.

When standard continuous-wave laser heating is used in LHDACs loaded with H, diffusion of H into the anvils causes them to become brittle and fail (Deemyad *et al.*,

2005). This inherent issue to working with pure H in the LHDAC has prevented experiments exploring reactions between hydrogen and silicates and the pressure-temperature (P-T) conditions expected for the planetary interiors. To facilitate these experiments, I utilize a pulsed laser-heating system (Deemyad *et al.*, 2005; Goncharov *et al.*, 2010) to reduce the amount of time the H is molten and thus mitigate the amount of hydrogen diffusion into the anvils and the gasket material. Each pulsed heating event (H.E.) consisted of 10^5 pulses with a width of $1\,\mu s$ and frequency of $10\,kHz$. While the heating duration is short (0.1s of total exposure time to the near-IR lasers), I found hydrogen is extremely reactive with molten silicates at high temperatures allowing chemical reactions to complete. The synchrotron X-ray beams were time-gated and synchronized with the laser pulses to ensure that diffraction measurements can take place only when the sample reaches the highest temperature during heating. Additionally, the laser-heating spot size is an approximately 25 μm-diameter circle while the X-ray spot size is much smaller at 3×4 μm. This helps mitigate thermal gradients in the high-temperature diffraction patterns. The laser-heating system provides a flat top laser beam intensity profile which further reduces thermal gradients in the hot spot (Prakapenka *et al.*, 2008). During each heating event, 20 streak spectroradiometry measurements were collected. In our experiments, temperature varies within the order of hundres of Kelvin during pulsed heating events, sufficient for the purpose of this work – melting behavior of silicates in a H medium. The thermal emission spectra were fitted to the grey-body equation to estimate the temperatures of the double-sided laser-heating (Prakapenka *et al.*, 2008).

2-D diffraction images were collected utilizing a Dectris Pilatus 1M CdTe detector. These were then integrated to 1-D diffraction patterns using DIOPTAS (Prescher and Prakapenka, 2015). The CeO_2 and LaB_6 standards were used to determine the sample-to-detector distance and correct for tilt of the detector. I used PeakPo (Shim,

2019) to fit the diffraction peaks with pseudo-Voigt profile functions, then proceeded with unit-cell parameter fitting with the statistical approaches presented in Holland and Redfern (1997). Pressure was calculated by measuring the unit-cell volume of a gold grain at the edge of the sample chamber before heating and comparing said volume the with the equation of state of gold (Ye *et al.*, 2017). The gold grains were not mixed with the sample to prevent reactions/alloying with the sample material and were rather placed on the edge of the sample chamber. Thus, pressure could not be measured in-situ at high temperatures. Thermal pressure in a liquid Ar medium at temperatures of 1000–4000 K is $\sim$ 0.5–2.5 GPa (Dewaele *et al.*, 1998). All our experiments exceeded the melting temperature of our pressure medium, H (Fig. 5.1). However, liquid H is more compressible than liquid Ar, so our thermal pressure is likely smaller than the estimation from Dewaele *et al.* (1998) in our experiments. Note that thermal pressure is not of great significance for the purpose of this study, which is to explore chemical reactions between hydrogen and fayalite at high pressures.

Raman measurements were conducted utilizing the Raman spectroscopy system at GSECARS (Holtgrewe *et al.*, 2019) for the identification of OH vibrations after heating. The sample was illuminated with a monochromatic 532nm beam from a Coherent VERDI V2 laser. Spectra were collected over a wide range of wavenumbers (1400-3600 rel cm^{-1}) utilizing a Princeton Instruments Acton Series 2500 spectrograph. Pixel-to-pixel sensitivity differences in the CCD detector were calibrated using the spectrum of a glass with well-known fluorescence intensities at different wavenumbers.
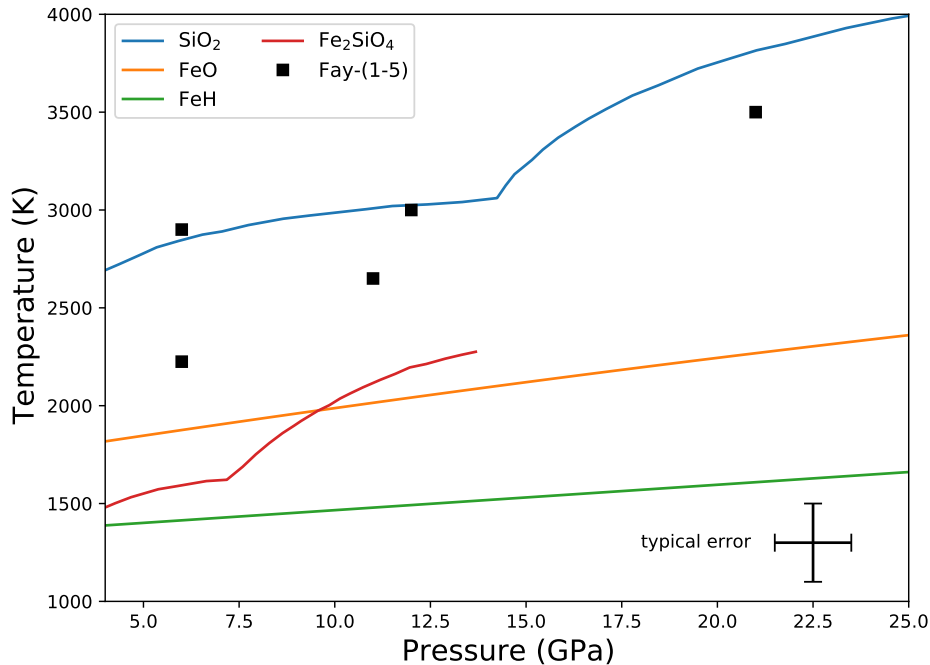
Figure 5.1: Pressure-temperature (P-T) conditions of the LHDAC experiments in this study (data points) shown with the melting curves of relevant materials: SiO_2: Andrault *et al.* (2020); Fe_2SiO_4: Ohtani (1979); FeO: Boehler *et al.* (1990); FeH_x: Sakamaki *et al.* (2009a). All experiments exceeded the melting temperature of H, FeH, FeO and Fe_2SiO_4 meaning all iron and hydrogen-bearing phases were molten.

5.4 Results

5.4.1 5-7 GPa: Fayalite Stability Field

Upon heating to 2900 K at 6 GPa, fayalite completely breaks down to form H_2O and multiple cubic metal phases as shown in the diffraction patterns in Fig. 5.2. One metal phase seen is in the fcc structure, the expected high-temperature phase for FeH_x at this pressure (Narygina *et al.*, 2011b). However, the volume of the fcc metal is 22.6% larger than the volume of stoichiometric FeH reported by Narygina *et al.* (2011b) at this pressure ($\sim$51.3 Å^3). It is so much larger, that the volume per Fe atom (15.9-16.4 Å^3) is actually approximately equal to that the expected volume of

84
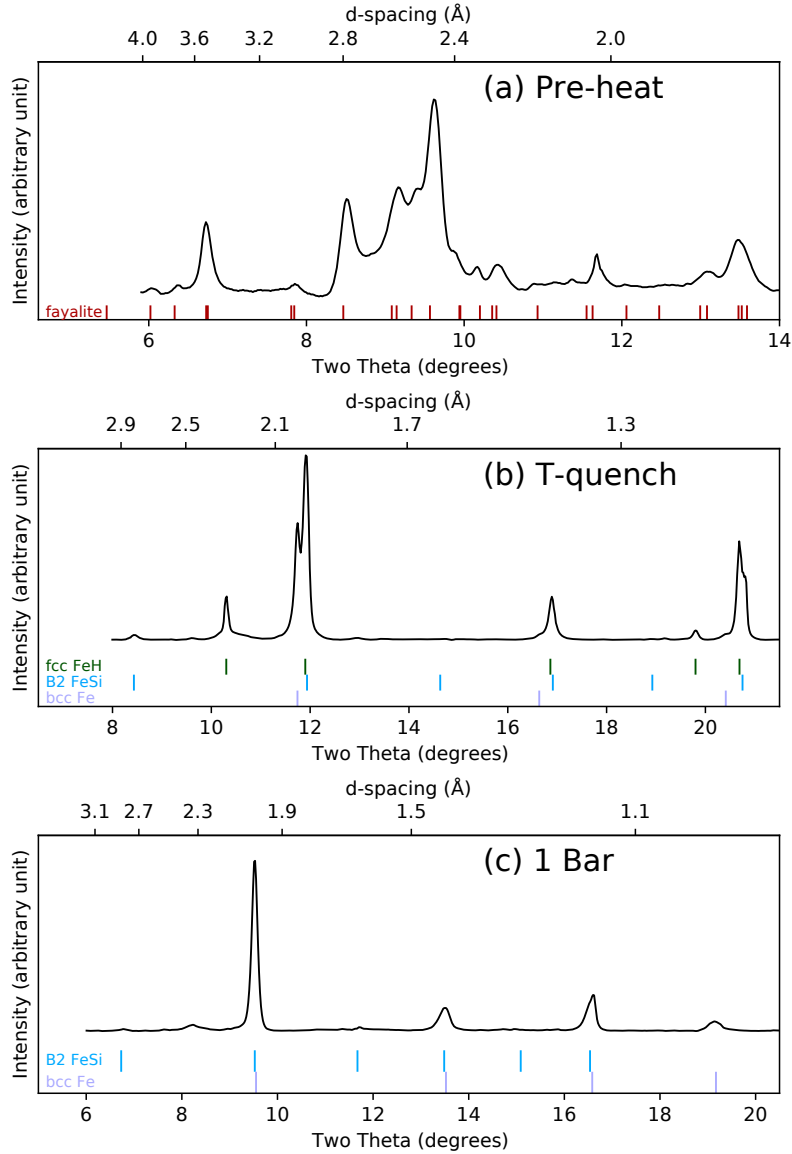
Figure 5.2: Natural fayalite at 5 GPa before heating (a), after heating to 2900 K (b), and after decompression to 1 bar (c). At a pressure where fayalite should be stable, after melting all Fe and Si are reduced to metal and O is released to the medium as H_2O. Tick marks show the expected positions of XRD peaks from various phases seen in the 1-D diffraction pattern.

tetragonal FeH_2 if its equation of state is extended to this pressure (Fig. 5.8) (Pépin *et al.*, 2014). Following the method of Antonov *et al.* (2019) (fcc FeH_x, $x = \frac{\Delta V \ \mathring{A}^3}{2.2}$) gives values of x=2.2, 2.4, and 2.2 for the FeH_x formed in runs FAY-1, FAY-1 (high and low volumes, see discussion in the second paragraph of section 5.4.2 and figure
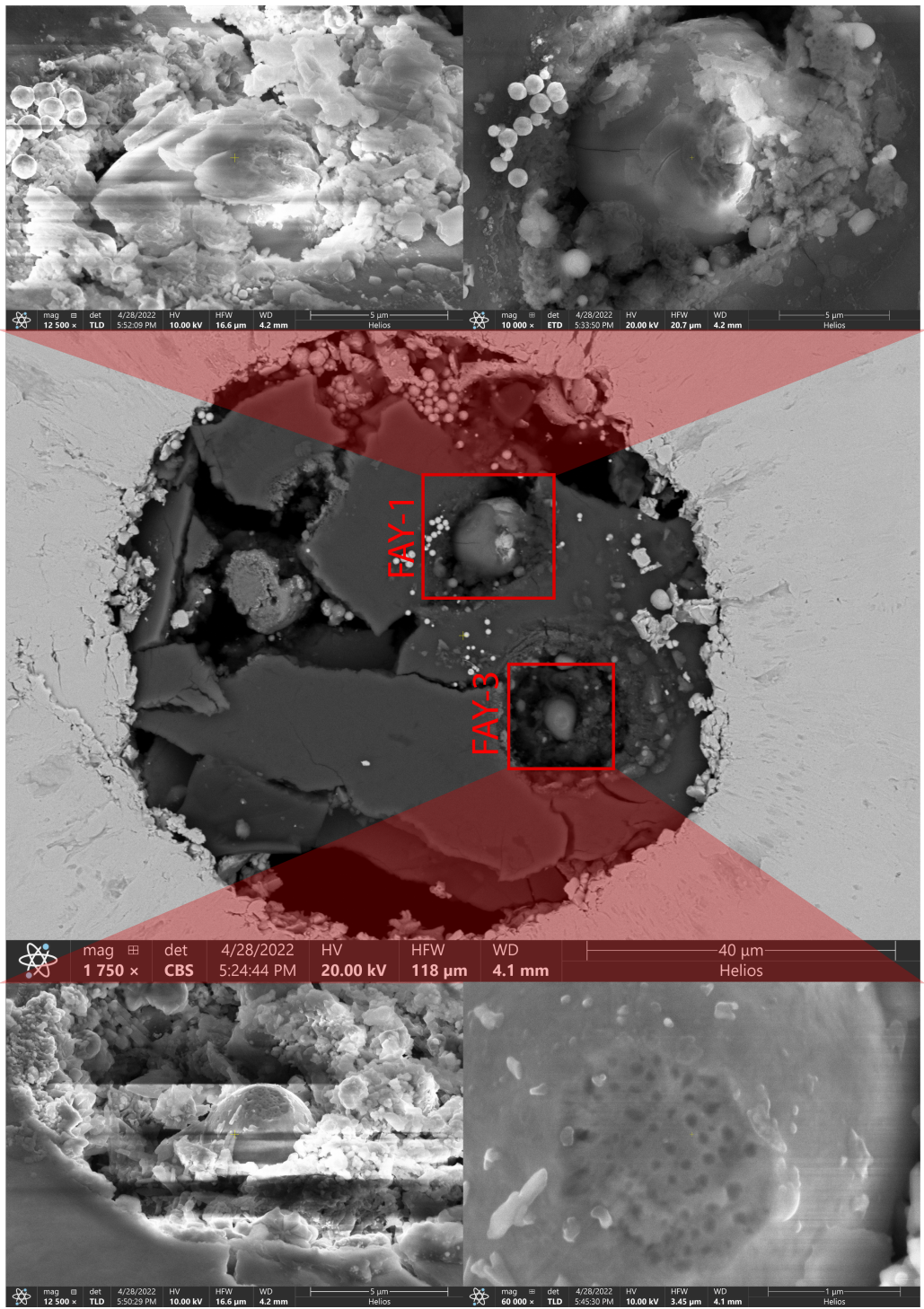
Figure 5.3: SEM images of heating spots FAY-1 and FAY-3. On the the images on the right are taken along the optical axis showing the heated area and the images on the left at a tilted angle to show post-heating sample topography.

5.5 for more information), and FAY-2 respectively.

Solid Fe is not known to take in this much H until pressures exceeding 67 GPa as tetragonal FeH_2 and cubic FeH_3 above 86 GPa (Pépin *et al.*, 2014). This observation of superstoichiotric alloying with H/Fe 2 at pressures below 10 GPa suggests that at low pressures (5–7 GPa), H-solubility in Fe melt exceeds that of the solubility of solid Fe by a factor of $\sim$2 and my observation is of the quenched molten FeH_x rather than a solid-fluid reaction between Fe and H.

Similarly, a B2 metal phase (presumably Fe-Si alloy) with a unit cell volume 7.2% larger than stoichiometric FeSi (Fischer *et al.*, 2014) is observed. This is likely due to a slight excess of Fe (i.e. Fe/Si>1) which has a higher atomic radius than Si, rather than hydrogenation of FeSi which has not been observed in previous experiments with Fe-Si alloys under a H atmosphere (Chapter 4 and (Fu *et al.*, 2022b)). The existence of Si in Fe is inferred for the reasons discussed above and the lack of a visible Si-bearing phase in the quenched XRD patterns (Fig. 5.2). Alternatively, experiments on SiO_2 in H at similar *P-T* conditions found that silica breaks down in H to form H_2O and SiH_4. While I do not observe SiH_4 in Raman spectroscopy, I cannot rule out its presence because there is a significant overlap in the Raman modes of SiH_4 and diamond fluorescence and Raman quality diamonds were not used in this work due to the rapid deterioration of diamond anvils when used with H.

A bcc metal phase with a unit cell volume 1.7% larger than pure bcc Fe metal was also observed. While bcc iron is not observed in the pure Fe-H system at pressures above 3.5 GPa (Badding *et al.*, 1991) and temperatures this high (Narygina *et al.*, 2011b), Lin *et al.* (2002) showed that a small amount of Si can stabilize bcc Fe beyond its standard stability field. It is likely our observation of bcc Fe is due to slight incorporation of Si. The volume expansion of 1.7% may be due to hydrogenation but is far smaller than the $\sim$20–25% volume expansion seen in 1:1 FeH structures

(Badding *et al.*, 1991; Narygina *et al.*, 2011b) consistent with previous observations that Si (which may be stabilizing this structure) inhibits the hydrogenation of cubic Fe (Chapter 4 and Fu *et al.* (2022b)).

Upon decompression to 1 bar, the fcc phase disappears, suggesting it was indeed FeH_x (which is known to lose hydrogen below $\sim$3.5 GPa (Badding *et al.*, 1991)), while the B2 and bcc phases remain stable to 1 bar.

The products observed along with the disappearance of fayalite suggest the following reaction:

$$Fe_2SiO_4 \text{ (m)} + 5H_2 \text{ (f)} \rightarrow FeH_2 \text{ (m)} + FeSi \text{ (m)} + 4H_2O \text{ (f)}, \qquad (5.1)$$
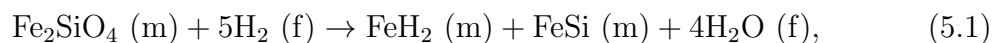
where (m) stands for melt and (f) stands for supercritical fluid. It should be noted that the stoichiometry of the alloys is approximate and not exact as their unit cell volumes are all expanded relative to their 1:1 stoichiometric expected volumes as noted above (FeH_x in particular shows variation from x=2.2-2.4). H_2O is observed using Raman spectroscopy at high-pressure after heating (Raman measurements are presented and discussed in section 5.4.3). It is interesting to note that while in the preceding experiments with Mg-bearing olivine MgO remained oxidized as MgO (Chapter 3, section 3.4.2). In this experiment with no Mg, all components of the fayalite are reduced to form metal alloys while the oxygen they release still reacts with H_2 to form H_2O.

5.4.2 10-11 GPa: Spinel Phase Stability Field

After heating to 3000 K at 10 GPa in a H medium–well above the melting temperature of $\sim$2000 K (Fig. 5.1)–fayalite breaks down to form silica and iron metal. Silica is present as both stishovite and coesite as during temperature quenching the silica melt crosses the phase transition line with coesite crystallizing at higher temper-
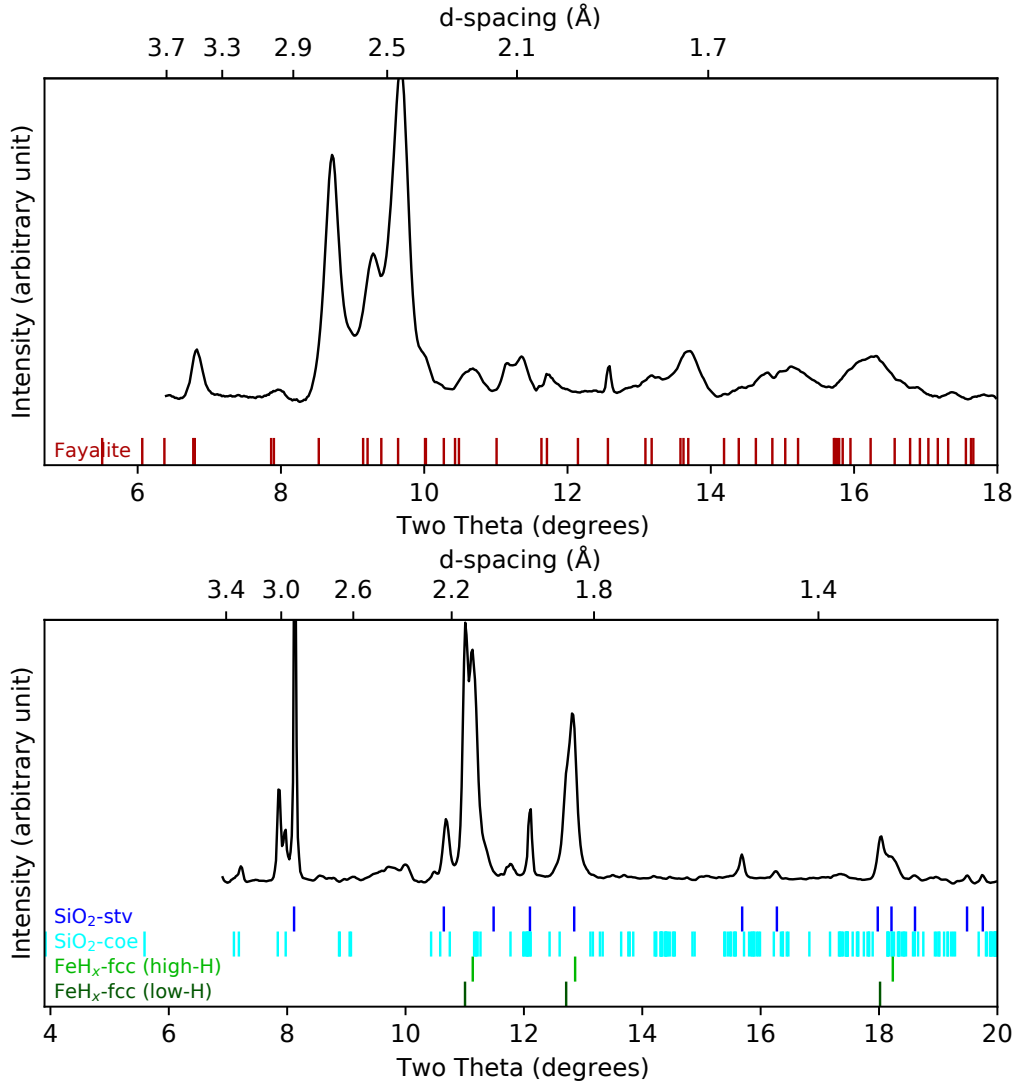
Figure 5.4: Natural fayalite at 10 GPa before heating (top), and 6μm away from the heating center after heating to 3000 K (bottom). Fayalite breaks down to form SiO_2 and FeH_x. Note the distinct peak splitting of the FeH_x peak at $2\theta=11$ due to the two distinct volumes for the phase.

atures and stishovite crystallizing after further cooling due to the positive Clapeyron slope of the phase boundary (Akimoto *et al.*, 1977). It is important to note the presence of silica and lack of Fe-Si alloy. In all the experiments in chapter 4 as well as the lower pressure experiment in this chapter, after the breakdown of the silicate phase, Si is reduced to metal and alloys with Fe (note also that FeSi and FeH_x form

separate phases as Si limits H in Fe (Fu *et al.*, 2022a)). It may be that the extra H_2O released by the reduction of the large amount of Fe^{2+} present in fayalite inhibits the formation of FeSi alloys (as seen by Kim et al (2022 *in review*)). The reason this was *not* seen in the experiment with the same composition at 5 GPa may be that at the lower pressures FeH_x (and other metal alloys) appeared to take in greater amounts of light elements expanding their unit cell (Fig. 5.8), possibly modifying the local oxygen fugacity such that it was lower than $FeO + \frac{3}{2}H_2 \rightarrow FeH + H_2O$ and $SiO_2 + H_2 \leftrightarrow Si^0 + H_2O$, while in the higher pressure experiments only the former holds true.
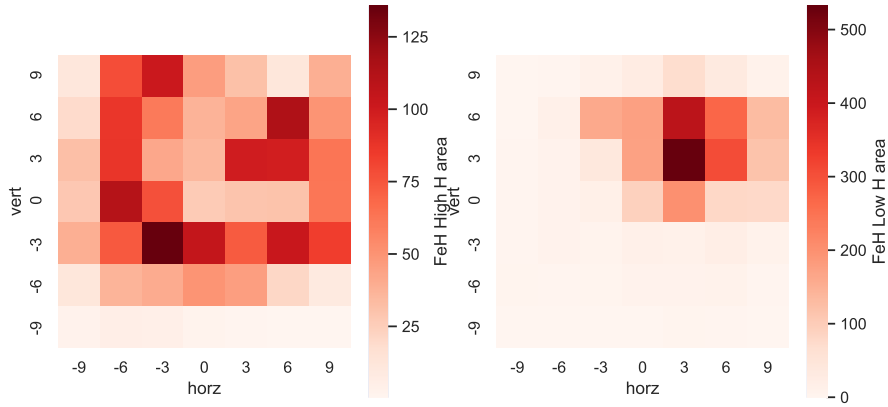
Figure 5.5: Map showing the distribution of high and low FeH_x volumes in sample FAY-3 at 300K and 12 GPa after quenching from one 3000K heating event. The heating center was at position (3,3).

Similarly to the experiments at 6 GPa, two distinct populations of fcc FeH_x exist with a high and low volume (Figure 5.4. One with a unit-cell volume of 50.40Å^3(corresponding to a value of $\frac{H}{Fe}$=0.81) and one with a unit cell volume of 51.98Å^3 (corresponding to a value of $\frac{H}{Fe}$=1.01). In the heating center the smaller (x=0.81) fcc FeH phase is dominant while just outside the hottest area the larger (x=1.01) suggesting that while melting enhances the solubility of H in Fe, higher

temperatures reduce the effect (Figure 5.5). A similar relationship was seen in the two volumes of super-stoichiometic FeH_x in runs FAY-1 and FAY-2. The observed decomposition of fayalite to form FeH_x and SiO_2 (detected via XRD) and H_2O (detected via Raman spectroscopy) implies the following chemical reaction:

$$Fe_2SiO_4 \; (l) + 3H_2 \; (f) \rightarrow 2FeH_x \; (l) + 2H_2O \; (f) + SiO_2 \; (s) \qquad (5.2)$$
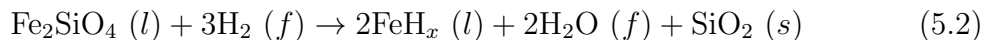
where $x \approx 1$ varies slightly, sensitive to the local temperature/thermal gradients. Upon decompression to 1 bar, both coesite and stishovite remain but fcc FeH_x reverts to bcc Fe. The unit-cell parameter of the bcc phase is 2.8677 ± 0.0003 Å, perfectly in-line with the expected value of pure Fe of 2.867 Å (Rotter and Smith, 1966) suggesting that all hydrogen has left the crystal structure of Fe upon decompression. Stishovite also maintains a slight volume expansion at 1 bar ($V = 46.67 \pm 0.08$ Å^3 compared to 46.50 Å^3 reported by Sinclair and Ringwood (1978) for anhydrous stishovite) implying that water released by the reduction of Fe is stored in the crystal structure of stishovite. Nisr $et\ al.$ (2017c) reported the relationship between unit-cell parameters and water content for hydrous stishovite. Utilizing that calibration, the change in unit-cell volumes implies $\sim$0.7 wt% H_2O in this stishovite. However, the minimal change in the axial ratio relative to anhydrous stishovite ($\frac{c}{a}$=0.640 compared to $\frac{c}{a}$=0.641 reported by (Andrault $et\ al.$, 1998)) does not align with the change in increase axial ratios reported in (Nisr $et\ al.$, 2017c) for hydrous stishovite due to the elongation of the a-axis, so the estimation given should be interpreted with caution.

5.4.3 21 GPa: Above the Stability Field of Fe_2SiO_4

Above $\sim$18 GPa fayalite is known to break down into wüstite and stishovite without H (Ohtani, 1979). This is still observed in our experiments in the presence

of hydrogen.

$$Fe_2SiO_4 \rightarrow 2FeO + SiO_2. \tag{5.3}$$

However, as shown in Chapter 3 FeO is known to react with hydrogen forming FeH_x and releasing H_2O (Chapter 3:

$$FeO\ (m) + 1.5H_2\ (f) \rightarrow FeH\ (m) + H_2O\ (f). \tag{5.4}$$
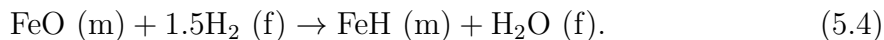
Combining these equations gives us the same reaction as shown in equation 5.2, which shows the complete breakdown of fayalite into stishovite, water, and iron-hydrogen alloy. This complete reaction can be seen in X-ray diffraction in figure 5.7. It is important to note that just as in the experiments in the spinel stability field, Si was not reduced to metal and instead remained as an oxide, supporting the hypothesis that the additional H_2O released via the reduction of iron (Eq. 5.4) inhibits the alloying of Fe and Si as also seen and discussed in section 5.4.2. The presence of H_2O is confirmed via in-situ Raman spectroscopy (Fig. 5.6).

5.5   Discussion

In the presence of H, molten Fe_2SiO_4 (pressures of 6–21 GPa and temperatures of 2225–4500 K, see figure 5.1) breaks down. Melting is inferred from three lines of evidence. First, the measured temperature (via grey-body spectroradiometry) of all runs exceeds the known melting curve of fayalite (Ohtani, 1979). Second, in-situ optical imaging shows textures consistent with samples that have undergone melting (e.g. Fig. 4.4). Lastly, SEM imaging of recovered samples shows clear signs of melting such as bubbles in the quenched heating spot (Fig. 5.3).

In all heating runs, all diffraction peaks of the starting Fe-silicate phase disappear (figures 5.2(b), 5.4, and 5.7(b)). All Fe originally present is reduced to metal, alloying with H and possibly Si at pressures below 10 GPa. Below 10 GPa, twice the amount of
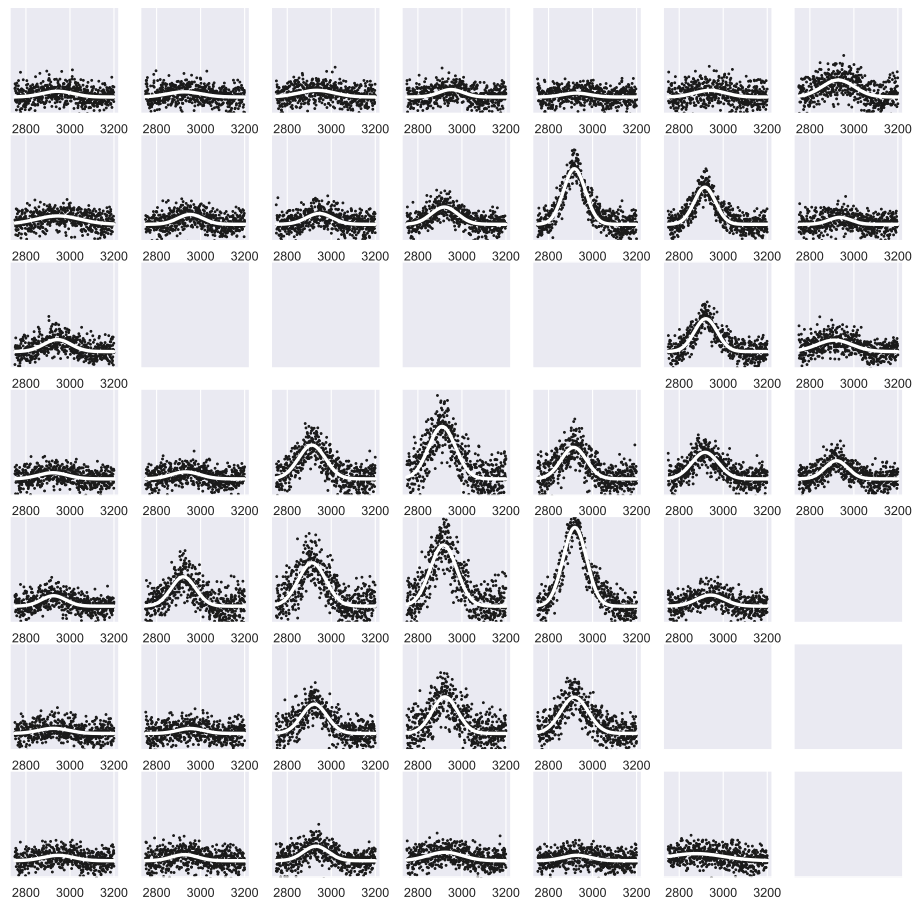
Figure 5.6: Map showing the distribution of water around the heated area in run FAY-5. The center is the center of the heated spot and the map spans $\pm 10\mu$m in each direction. The peak intensity distribution (OH stretch, plotted 2750–3100 cm^{-1} with intensity on the Y-axis) shows water is formed around the heated area with more being formed in the hotter heating center and less being formed in the cooler areas at the edge. The blank squares are failed spectra acquisitions.
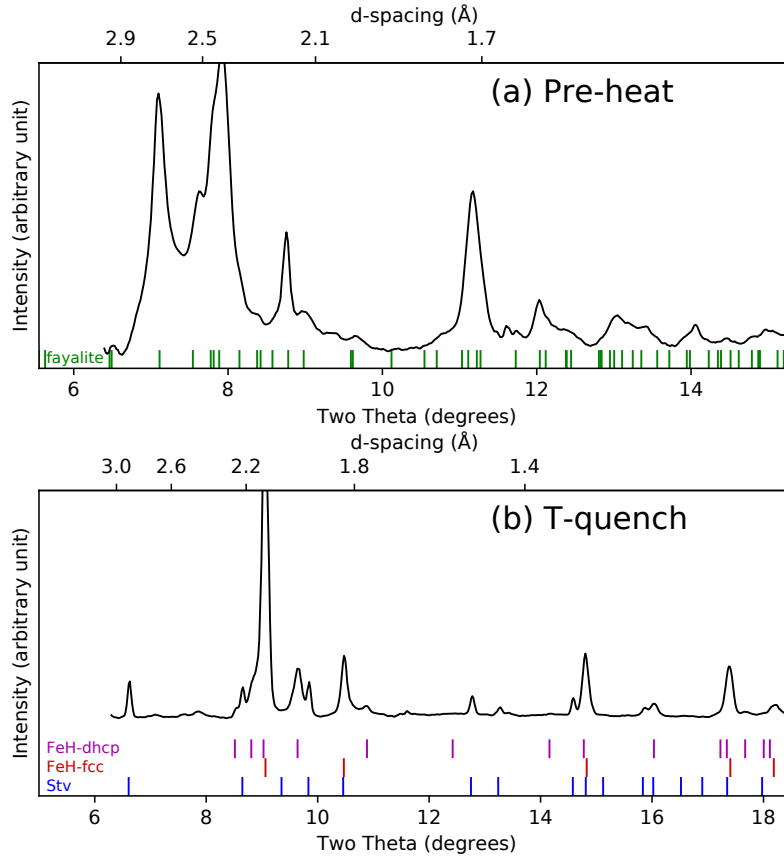
Figure 5.7: Fig 2. X-ray diffraction patterns showing natural fayalite before and after heating to 2500-4500 K at 21 GPa in a hydrogen medium. After heating the silicate phase has broken down form metal and stishovite (Eq. 5.2)

H is stored in Fe metal alloy than previously reported (Badding *et al.*, 1991; Narygina *et al.*, 2011b; Pépin *et al.*, 2014) and observed in chapters 3 and 4 at at pressures below 67 GPa: H/Fe≈2 vs. H/Fe≈1. Above 10 GPa, the unit-cell volumes of FeH_x are well aligned with $x = 1$ and no possible Fe-Si phases are seen. Instead, SiO_2-stishovite and coesite are observed. At these same *P-T* conditions, samples with olivine and silica mixed with Fe produced Fe-Si alloys in a hydrogen medium (chapter 4). This change in behavior may be due to the large production of H_2O by the reduction of Fe from the silicate phase: $\sim 10 \times$ more is present in these samples than San Carlos olivine and none is present in silica. When Fe^{2+} is reduced to Fe^0 by H, the released oxygen
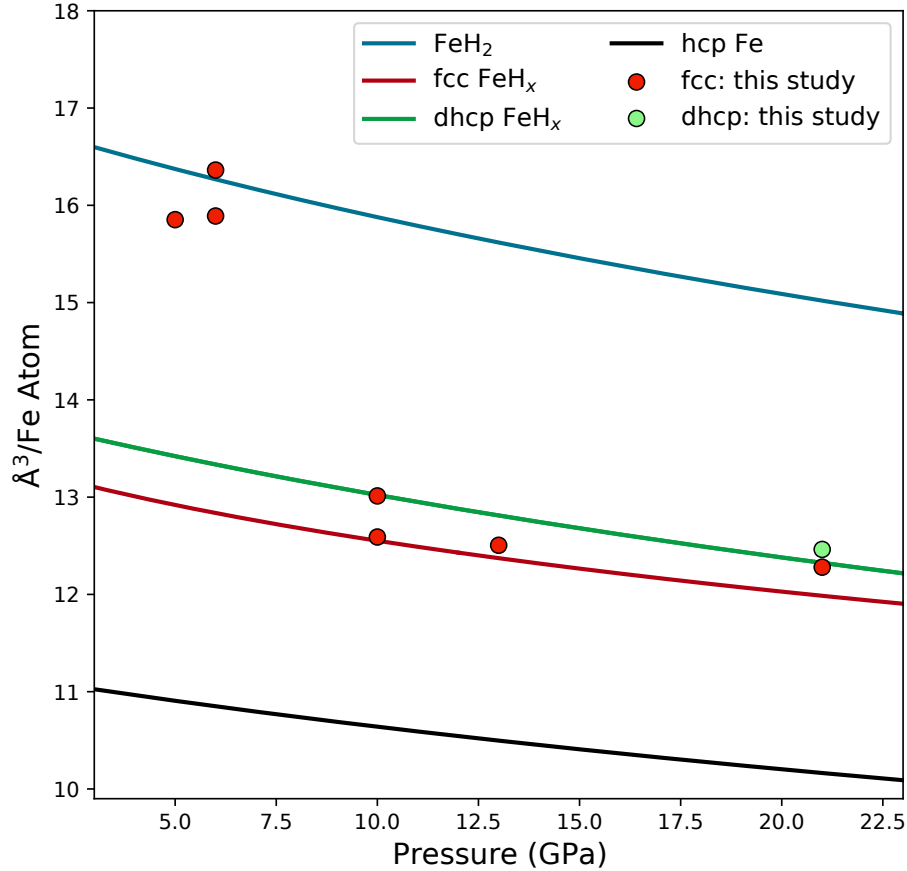
Figure 5.8: Pressure-volume data for Iron-hydrogen alloys formed in these experiments. All volumes greatly exceed that of pure Fe (Mao and Bell, 1979). At pressures above 10 GPa, the volumes of alloys appear to align well with stoichiometric fcc and dhcp FeH (Badding *et al.*, 1991; Narygina *et al.*, 2011b). However at lower pressures volumes imply a much higher H content close to FeH_x x=2 (Pépin *et al.*, 2014).

reacts with the H medium to form H_2O. H_2O is known to inhibit the formation of FeSi alloys (Kim et al, 2022 *in review*).

This production of H_2O could play a major role in systems where significant quantities of oxidized Fe are present. For example, in sub-Neptune sized planets there may exist a high-pressure interface between H_2 and a silicate magma ocean. H reactions with the oxidized magma may produce large quantities of H_2O which will then partition into the atmosphere and mantle. H_2O partitioned into the atmosphere (or interior and outgassed to the atmosphere) may form a long-lived H_2O dominated

atmosphere or hydrosphere (Kite et $al.$, 2020; Kite and Schaefer, 2021). Such long lived water-rich secondary atmospheres may also be an important observable diagnostic to distinguish super-Earth sized planets that formed as sub-Neptunes before losing their primary H-dominated atmospheres (Owen and Wu, 2013). While H_2O may be an important atmospheric species, H_2O may preferentially partition into the mantle at low pressures (Moore et $al.$, 1995; Hirschmann et $al.$, 2012). As shown in this work, the balance between the amount of H_2 and H_2O in silicate melt may play an important role in the control of how much Si is reduced to metal alloys. As more water is partitioned to the interior, more silica may remain oxidized thus increasing the viscosity of the magma (Urbain et $al.$, 1982) and inhibiting convection and possibly hindering the ingassing of additional H. However, H_2O is known to decrease the viscosity of magma (Karato and Wu, 1993) which may at least partially offset this dynamical change allowing additional H to be ingassed, reducing Fe and Si and sequestering H and Si in the metallic core.

H has been proposed as a possible light element for planetary cores (Kronig et $al.$, 1946) and the alloying behavior of Fe-H alloys has been studied extensively at high pressure (Badding et $al.$, 1991; Yagi and Hishinuma, 1995; Hirao et $al.$, 2004; Narygina et $al.$, 2011b; Pépin et $al.$, 2014). To this point, all studies have found that at pressures below 67 GPa, stoichiometric alloying (1:1 alloying of Fe and H) was the maximum storage capacity for H in Fe synthesized at subsolidus conditions. Pépin et $al.$ (2014) found FeH_x undergoes phase transitions at 67 and 86 GPa to new structures with H/Fe = 2 and H/Fe = 3, respectively. However, in this study, I observe fcc metal with a unit cell volume corresponding to FeH_x x≈2 (Fig. 5.8). This observation is roughly 60 GPa lower than the previously measured threshold for FeH_2 (although Hirao et $al.$ (2004) interpreted an anomalous change in compressability behavior above 50 GPa as an increase in H solubility, which is still ~44 GPa higher

than our conditions).

This superstoichiometric alloying behavior may be due to increased solubility of H in lower-pressure Fe melts. Previous experiments at this pressure have not achieved melting, whereas both of the runs at 6 GPa (prior to heating) exceeded the melting temperature of FeH (Table 5.1, Fig. 5.1, Sakamaki *et al.*, 2009a). Thus the superstoichiometric alloying may be H dissolved in Fe melt, which is then captured upon temperature quench rather than migration of H into the Fe crystal structure in the solid state. This is supported by the fact that after heating sample FAY-4, XRD mapping was conducted. This map showed two distinct populations of volumes for FeH$_x$ with the lower volume (less H; $x \approx 0.81$) found in the hottest heating center and the lower volume (more H; $x \approx 1.01$) suggesting a negative correlation between temperature and hydrogenation of Fe melt (Fig. 5.5).

However, there seems to be a pressure effect on this phenomenon. Experiments above 10 GPa still showed two populations of FeH$_x$ (as shown in figure 5.5). However, the unit-cell volumes of FeH$_x$ are quite near $x = 1$ as seen in previous work, rather than $x = 2$ as seen in our lower-pressure experiments. It is also possible that Fe melt at higher pressures also maintains the expanded solubility for H, but it is not quenchable. In figure 5.3 at heating spot FAY-3 (bottom) one can see bubbles in the quenched sphere of metal at the center of the heating spot. I interpret this as bubbles of H escaping the metallic melt as the temperature quenches. This may imply that above 10 GPa FeH$_x$ melt maintains its expanded capacity for H but it is not quenchable (thus bubbles form as H escapes the rapidly cooling melt). No such bubbles appear in the heating spot of FAY-1 where the expanded unit-cell volume of fcc FeH$_x$ was seen at high pressure after temperature quenching implying the superstoichiometric melt was quenchable at this pressure. However, both samples lose all H and revert to pure bcc Fe at ambient pressure as is expected for FeH$_x$ (Badding *et al.*, 1991).

Additional insights can be gleaned from the texture of the two heating spots in figure 5.3. Around the smaller ball of metal in spot FAY-3 there exists a large amount of granular oxide rich material (inferred by the charging seen in the lower-left panel). This was seen in XRD as SiO_2 stishovite and coesite. In sample FAY-1, no Si oxide phase was seen in XRD, implying possibly dissolution of Si in an Fe phase (B2 FeSi). This may be seen in the metallic ball at the heating center which appears to have two distinct components shown by Z-contrast (contrast is sensitive to atomic number rather than surface texture) in the BSE image (upper right). This may also imply that not only is superstoichiometric FeH_x quenchable at lower pressures, there may be a change in the miscibility of H_2 and H_2O between 7 and 10 GPa since water inhibits the formation of FeSi (as it does in the higher pressure experiments). This hypothesis may reconcile the experimental observations of the immiscibility of H_2 and H_2O at pressures below 3 GPa (Bali *et al.*, 2013b) with the ab initio simulations that found the two were miscible up to 70 GPa (Soubiran and Militzer, 2015b).

This twofold increase in the solubility of H in Fe melt at low pressures could have broad ranging implications for planetary science. For example, in sub-Neptune planets where an interface between a H envelope and magma ocean may exist at pressures below 10 GPa, this enhanced solubility of H may aid in the ingassing of H to the interior. Along with the high solubility of H in Fe melt, H is also consumed to form H_2O by the reduction of Fe (and possibly Si). All in all, for each mole of fayalite decomposed by H, 5 moles of H_2 are consumed at pressures below 10 GPa (Eq. 5.1) while at higher pressures 3 moles are consumed (Eq. 5.2).

5.6   Acknowledgments

Chapter 6

OXIDATION OF THE INTERIORS OF CARBIDE EXOPLANETS

6.1 Abstract

Astrophysical measurements have shown that some stars have sufficiently high carbon-to-oxygen ratios such that the planets they host would be mainly composed of carbides instead of silicates. I studied the behavior of silicon carbide in the presence of water under the high pressure–temperature conditions relevant to planetary interiors in the laser-heated diamond-anvil cell (LHDAC). When reacting with water, silicon carbide converts to silica (stishovite) and diamond at pressures up to 50 GPa and temperatures up to 2500 K: $SiC + 2H_2O \rightarrow SiO_2 + C + 2H_2$. Therefore, if water can be incorporated into carbide planets during their formation or through later delivery, they could be oxidized and have mineralogy dominated by silicates and diamond in their interiors. The reaction could produce CH_4 at shallower depths and H_2 at greater depths which could be degassed from the interior, causing the atmospheres of the converted carbon planets to be rich in reducing gases. Excess water after the reaction can be stored in dense silica polymorphs in the interiors of the converted carbon planets. Such conversion of mineralogy to diamond and silicates would decrease the density of carbon-rich planet, making the converted planets distinct from silicate planets in mass-radius relations for the 2–8 Earth mass range.

6.2 Introduction

Carbon-rich planets could exist in extra-solar systems containing either stars with high C/O ratios (Bond *et al.*, 2010) or proto-planetary discs of Sun-like stars with

locally elevated C/O ratios (Kuchner and Seager, 2005). Bond *et al.* (2010) suggested a significant population of planet-hosting stars have C/O ratios well over 1; however, recent studies have called into question the abundance of those stars (Fortney, 2012; Nissen, 2013; Teske *et al.*, 2014; Suárez-Andrés *et al.*, 2018; Nissen and Gustafsson, 2018). While they seem to comprise no more than 12–17% of planetary systems (Wilson *et al.*, 2016; Stonkutė *et al.*, 2020), some systems with C/O > 0.8 likely exist (Young *et al.*, 2014). Because our solar system does not host carbon-dominated planets, relatively little is known about the type of structure and dynamics that make up the surface and interior of these planets.

In those carbon-rich planets, silicon carbide (SiC) can be the major mantle phase (Larimer, 1975). Therefore, high-pressure polymorphs of SiC have been studied extensively at high pressure-temperature ($P-T$) in recent years (Nisr *et al.*, 2017b; Daviau and Lee, 2017a; Miozzi *et al.*, 2018; Daviau *et al.*, 2019; Kidokoro *et al.*, 2017) to understand the interiors of carbon-rich planets. On the other hand, the oxidation of SiC under hydrothermal conditions has been known in the materials science literature for many decades. For example, SiC oxidizes in the presence of water at temperatures as low as 700 K and pressures as low as 0.01 GPa to form silica and gasses (Yoshimura *et al.*, 1986). The well-known reaction at very low pressure conditions raises an important question on the stability of SiC in the interior of carbon-rich planets when water exists or is delivered. Recent studies have found that SiC could react with oxides in carbon rich bulk compositions and form graphite at high temperature and under 2 GPa (Hakim *et al.*, 2018, 2019). However, these studies were conducted at low pressures and did not consider the effect of water. Therefore, it is important to further investigate if SiC would remain the main phase at the high $P-T$ conditions of the interiors of carbide planets in the presence of water. Here, I report experimental investigation on SiC + H_2O mixtures at high $P-T$ in the laser-heated diamond-anvil

cell (LHDAC) combined with synchrotron X-ray diffraction (XRD) and micro-Raman spectroscopy.

6.3 Materials and Methods

Starting materials were pure synthetic SiC (Alfa, purity 99.8%) of the hexagonal α phase (SiC-6H) or cubic β phase (SiC-3C). For LHDAC experiments, the SiC powder was mixed with gold powder (10 wt%) as a laser coupler and pressure calibrant. The SiC + gold powder mixture was cold-pressed into foils with approximately $10\,\mu$m of thickness. The foils were loaded into $125\,\mu$m and $260\,\mu$m holes drilled in a rhenium gasket which had been indented by diamond anvils with $200\,\mu$m and $400\,\mu$m diameter culets, respectively. The holes were then filled with deionized water. Samples were compressed to pressures between 20 and $40\,$GPa at 300 K before laser heating. A total of 18 LHDAC runs were performed (Table 6.1).

XRD patterns were collected at high $P-T$ in double-sided laser-heated DAC (diamond-anvil cell) at the 13-IDD of the GeoSoilEnviroConsortium for Advanced Radiation Sources (GSECARS) sector at the Advanced Photon Source (APS). Monochromatic X-ray beams of wavelength $0.4133\,$Å or $0.3344\,$Å were focused on the sample in LHDAC. Near-infrared laser beams were coaxially aligned and focused with the X-ray beams for in situ laser heating. Temperatures were estimated by fitting thermal spectra from both sides to the gray-body equation (Prakapenka *et al.*, 2008). 2-D diffraction images, collected from a Dectris Pilatus detector, were integrated into 1-D diffraction patterns using DIOPTAS (Prescher and Prakapenka, 2015). Using the CeO_2 and LaB_6 standards, I corrected for tilt of the detector and sample-to-detector distance. The diffraction peaks were fitted with a pseudo-Voigt profile function to determine the unit-cell parameters in PeakPo (Shim, 2019). The unit-cell parameter fitting was conducted based on the statistical approaches presented in Holland and

Redfern (1997). Pressure was calculated by combining the measured unit-cell volume of gold with its equation of state (Ye *et al.*, 2017) using Pytheos (Shim, 2018). In some DAC runs, pressure was estimated from ruby spectra at 300 K (Piermarini and Block, 1975).

Micro-Raman measurements were conducted for the phase identification of the recovered samples from DAC runs 14–17 at Arizona State University (ASU). I used a solid-state (frequency doubled Nd:YAG) laser with a 532 nm monochromatic beam, set to a laser power of 50–100 mW (5–10 mW at the sample), as an excitation source. Measurements were conducted using an 1800 grooves/mm grating. The spectrometer was calibrated using the neon emission spectra. I calibrated pixel-to-pixel sensitivity differences in the CCD detector using the spectrum of a glass with well-known fluorescence intensities at different wavenumbers. Spectra were measured at different wavenumber ranges: 100–1000 cm^{-1} for SiC and SiO$_2$, 1000–1500 cm^{-1} for diamond, and 2000–4000 cm^{-1} for H$_2$O, CH$_4$, and H$_2$. The typical acquisition time was 50–100 seconds.

I calculated the mass-radius relations of planets composed of relevant materials. In the models, planets are composed of a single homogeneous layer. The equations-of-state parameters used for these calculations were from: Dewaele *et al.* (2008) for diamond, Miozzi *et al.* (2018) for silicon carbide in B1 structure, Dewaele *et al.* (2006) for iron metal, Stixrude and Lithgow-Bertelloni (2011) for silica (seifertite) and MgSiO$_3$ (bridgmanite), and Hemley *et al.* (1987) for ice. I chose the B1 phase of SiC and seifertite because they would be the dominant phases in 2–8 Earth mass planets (Daviau and Lee, 2017b; Miozzi *et al.*, 2018; Kidokoro *et al.*, 2017; Grocholski *et al.*, 2013). The equations of state were calculated using the Burnman package (Cottaar *et al.*, 2016). I did not include thermal effects, because internal temperatures of the exoplanets are not well known and the thermal effects are much smaller than pressure

effects on density of minerals for the mass range I consider.
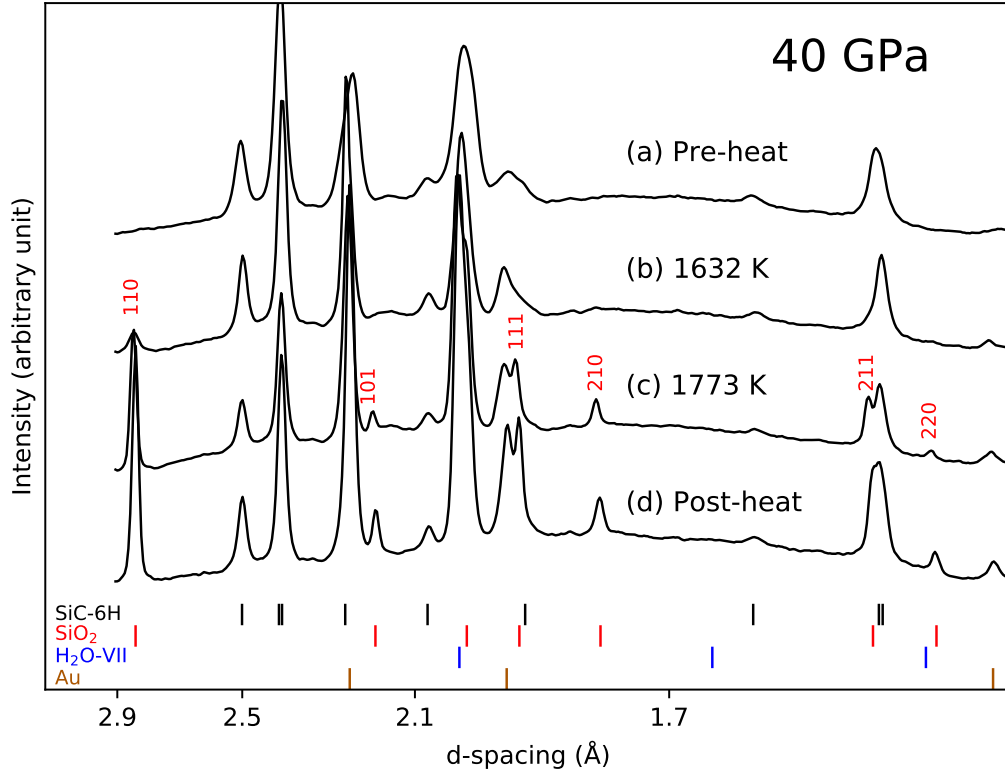
Figure 6.1: X-ray powder diffraction patterns measured at in-situ high pressures and high temperatures: (a) the starting material before heating, (b) the sample just after heating began, (c) the sample 10 min later, and (d) the sample after heating. The energy of X-ray beam was 37 keV. The colored vertical bars show the expected diffraction peak positions of phases. The Miller indices of main stishovite lines are shown to highlight the appearance of those lines during heating.

6.4 Results

X-ray diffraction (XRD) patterns showed the conversion of SiC into SiO_2 stishovite from every run across our entire $P-T$ range regardless of the polymorphs of SiC. For example, at 40 GPa before heating, the only peaks observed were from SiC-6H and H_2O ice VII (starting mixture) together with Au (pressure standard) (Figure 6.1). As soon as the heating began, the 110_{stv} diffraction peak at 2.8 Å was immediately visible (the numbers are the Miller index and the subscript notes the phase). The

110_{stv} line is diagnostic of stishovite in our diffraction patterns for the identification of the phase because it does not overlap with lines from any other phases and it is the most intense peak for stishovite. After about 5 minutes of heating, other stishovite diffraction lines—such as the 101, 111, 210, 211, and 220 peaks—were all visible. All SiO_2 peaks continued to grow as heating continued, and they persisted after quench to room temperature at high pressure.
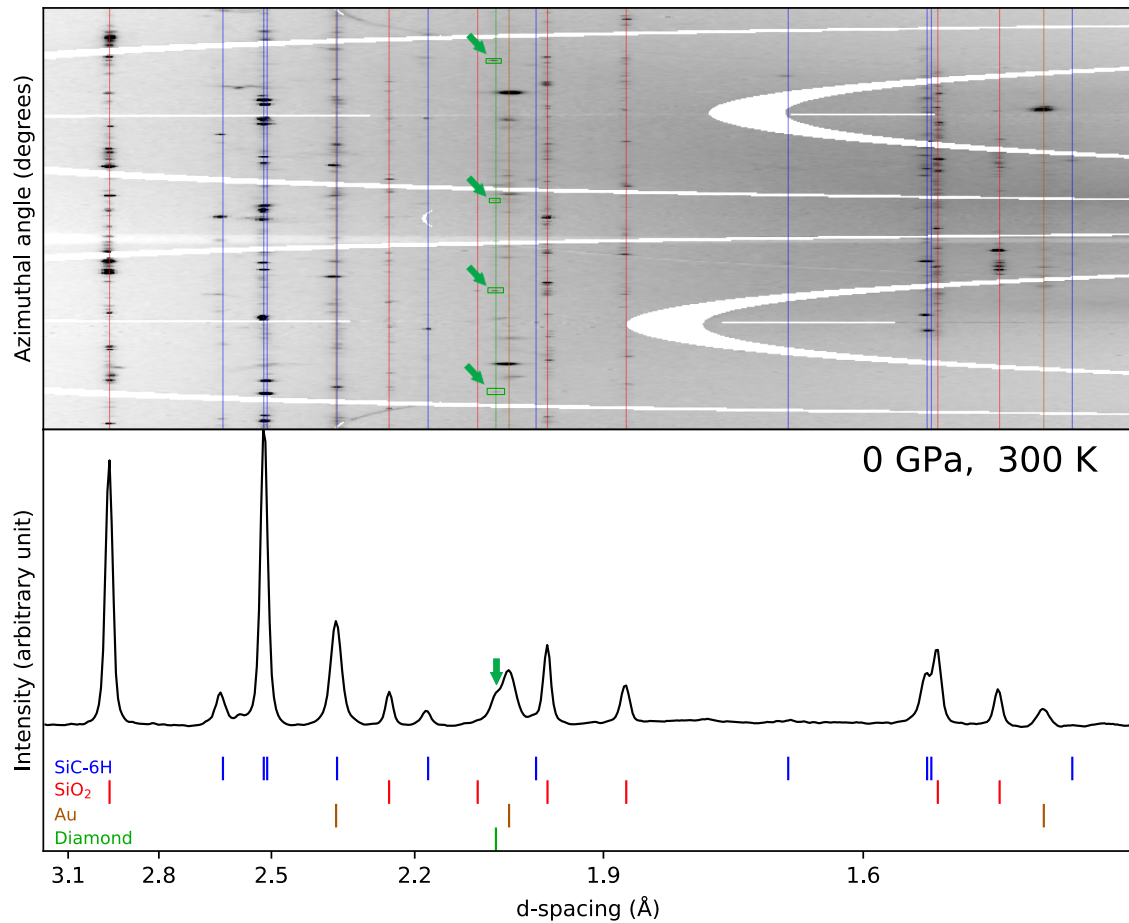
Figure 6.2: Diffraction pattern (bottom) of a sample heated to 1800 K at 40 GPa then recovered to room temperature at 1 bar. Diamond diffraction spots can be seen highlighted by the green rectangles and arrows in the unrolled 2-D diffraction image (top). These spots were only present in heated regions of the sample. The colored bars in the 1-D integrated pattern and the vertical lines in the 2-D unrolled image show the expected peak positions of phases.

In majority of our runs, temperatures were higher than the melting of H_2O ice.

In run DAC2, temperatures were lower than the melting temperature of H_2O ice reported in Schwager and Boehler (2008). The melting could be also inferred from a plateau in laser power and temperature relations as previous studies have found (Walter *et al.*, 2015). In this run, stishovite lines still appeared. Therefore, the reaction occurs in both solid and liquid regimes of H_2O; however, there is uncertainty in the melting curve of water. If melting temperature of water is low at high pressure as some other studies suggested (Goncharov *et al.*, 2005; Lin *et al.*, 2005), all of our temperatures would fall in the liquid water regime.

In all the LHDAC experiments, the stishovite peaks continued to grow until the end of the run, which I limited to 30 min for the mechanical stability of the DAC. The continuous growth of the peak intensity indicates that stishovite is stable over SiC in the presence of H_2O. The continued presence of SiC is likely related to kinetics due to the short heating duration. I expect that SiC would convert completely to stishovite with sufficiently long heating.

After heating to 1800 K at 42 GPa, I decompressed the sample to 1 bar and measured XRD patters of the recovered sample (run DAC4). I opened the DAC to remove liquid water through evaportion, and then closed the sample chamber again (but still at 1 Bar) for XRD measurements of the recovered samples. All the phases observed at high pressure remained at 1 bar, including stishovite. The lattice constants of the recovered samples were obtained by fitting the XRD patterns: $a = 4.1829(2)$ Å, $c = 2.6659(3)$ Å, and $V = 46.646(8)$ Å^3 in stishovite and $a = 3.081(8)$ Å, $c = 15.127(7)$ Å, and $V = 124.4(3)$ Å^3 in SiC (a and c are axial lengths and V is unit-cell volume). In those patterns, I also found some diffraction spots that indexed well with the diamond 111 line (Figure 6.2). This observation indicates that diamond exists as a few small single crystal grains likely grown in an H_2O medium. The line can also be clearly identified in the integrated 1D diffraction patterns. At in-situ high

106

pressure, it was difficult to unambiguously identify the diffraction lines of diamond formed through the reaction, because the most intense diffraction peak of diamond exists at the same 2θ angle range as the main diffraction line of H_2O ice VII.

Although phase fractions can be calculated from the diffraction intensities from randomly oriented crystallites in powder, it was difficult to apply the method for our diffraction patterns. As explained above, the diamond diffraction is from a small number of single crystals. In this case, the diffraction intensity can be highly sensitive to the preferred orientations of these grains and therefore cannot be used for estimating the phase fraction. The intensity of the diamond peak can be affected by other factors. Low-pressure experiments on this system showed the production of methane (Yoshimura *et al.*, 1986). Hirai *et al.* (2009) showed that the conversion of methane to diamond requires heating to elevated temperatures at high pressures. If the relatively low temperature in this work could not have supplied enough heat to overcome the slow kinetics of the transformation of CH_4 to diamond, some C may exist in fluid CH_4 which could be convected away in the liquid H_2O medium.

Micro-Raman spectroscopy of the recovered samples confirmed the presence of stishovite. In runs DAC 14–18 (Table 6.1), I conducted Raman measurements at in-situ high pressure at 40 GPa in a DAC after laser heating to 1500 K for 20 min (Figure 6.3). In order to reduce the Raman scattering from thick diamond anvils, I used a confocal setup. The black spectrum in Figure 6.3 was measured at an unheated area of the sample. The observed broad feature is from parts of diamond anvils with different stress conditions along pressure gradients. The depth resolution achieved in the confocal setup is approximately 30 μm, which is still somewhat greater than the thickness of the sample in DAC, 5–10 μm. Therefore, even if the focal plane is set on the surface of the sample in DAC, some intensity from the tip of the diamond anvils is expected to be detected. Indeed, the small increase in intensities near the
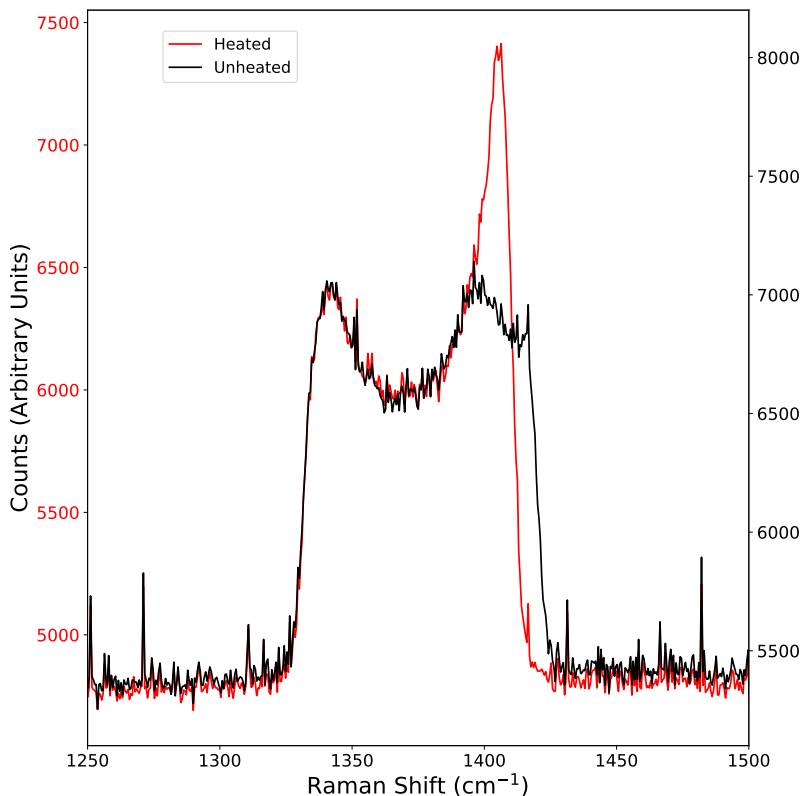
Figure 6.3: High-pressure Raman spectra of the sample synthesized at 40 GPa and 1500 K. The black spectrum was measured at an unheated portion of the sample and the red spectrum was measured at a heated portion. The sharp peak at 1400 cm^{-1} in the red spectrum is from pressurized diamond crystals formed from reaction 6.1.

highest wavenumber ($\sim$1400 cm^{-1}) should be from the tip of the diamond anvil which is under the highest stress. In a heated area, I observed a much more pronounced phonon peak intensity at $\sim$1400 cm^{-1}. This suggests that a majority of the intensity should come from the compressed diamond crystals in the sample chamber (Boppart *et al.*, 1985) formed from the SiC + H$_2$O reaction, rather than from the diamond anvil.

Both the XRD and Raman observations reported above indicate reaction between SiC and H$_2$O:

$$\text{SiC} + 2\text{H}_2\text{O} \rightarrow \text{SiO}_2 \text{ (stishovite)} + \text{C (diamond)} + 2\text{H}_2. \tag{6.1}$$
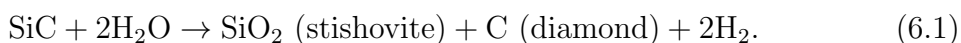
The reaction also predicts the formation of hydrogen. While I observed SiO$_2$ stishovite

108

and diamond, I did not directly observe hydrogen. Hydrogen is difficult to detect in XRD because of its extremely small scattering cross section compared with other materials in the sample chamber of our experiments. Molecular hydrogen has a Raman mode at 4100–4300 cm^{-1} at the pressure range of this study (Goncharov *et al.*, 2001; Gregoryanz *et al.*, 2003). However, I could not find the hydrogen peak in our Raman measurements. Hydrogen likely diffused out from the heated spot to the water medium and therefore can be diluted to a smaller fraction at any given spot. In this case, the hydrogen peak would be very difficult to detect.

Spektor *et al.* (2011) reported that stishovite can be hydrated and store up to 1.3 wt% H_2O in the crystal structure. Even greater H_2O storage capacities of dense silica polymophs were reported in recent LHDAC experiments, up to 8–13 wt% (Nisr *et al.*, 2020). Studies have shown that such significant hydration can expand the unit-cell volume of stishovite and alter the axial ratio (c/a) (Nisr *et al.*, 2017d; Spektor *et al.*, 2016; Nisr *et al.*, 2020). The diffraction patterns of our recovered LHDAC samples at 1 bar showed unit-cell volumes larger than those reported for anhydrous stishovite (Andrault *et al.*, 2003; Grocholski *et al.*, 2013). For example, stishovite in the recovered sample from run DAC6, heated to 1800 K at 40 GPa, was expanded by 0.28% compared to the anhydrous unit-cell volume (Andrault *et al.*, 2003). Based on the relationship between the unit-cell volume expansion and H_2O content reported by Nisr *et al.* (2017d), I obtained 0.5–0.6 wt% H_2O in the stishovite phase. Therefore, the stishovite formed from the SiC + H_2O reaction contains some amount of H_2O in the crystal structure.

6.5   Discussion

Some population (12–17%) of stars may have C/O ratios greater than 0.8 (Bond *et al.*, 2010; Petigura and Marcy, 2011; Wilson *et al.*, 2016; Stonkutė *et al.*, 2020), and
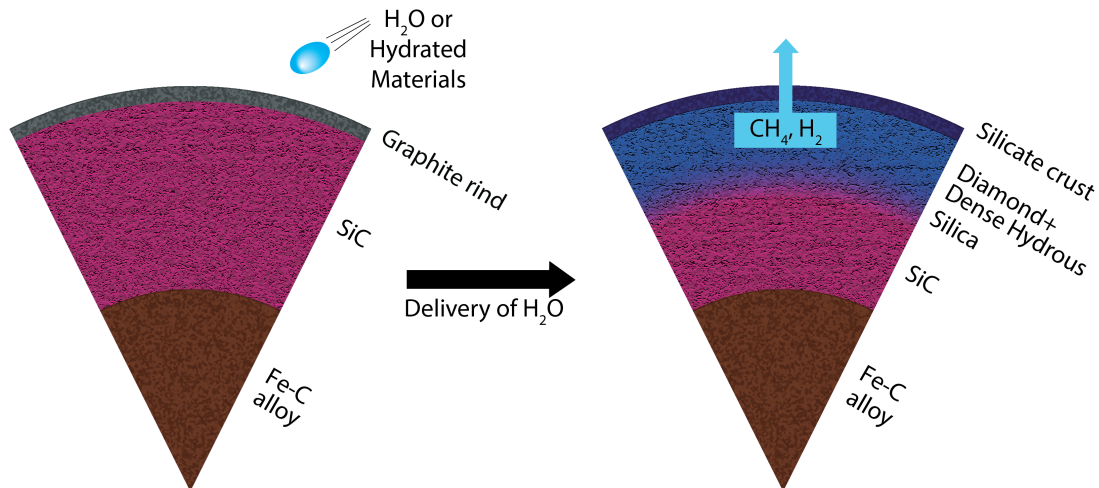
Figure 6.4: An example of a carbon planet with SiC as the major mantle phase (left). After bombardment with water-rich materials, the upper portion of the mantle, which was exposed to water, transforms from carbide to silicate and diamond (right). The reaction will also produce CH_4 at shallower depths and H_2 at greater depths. The reducing volatiles may be degassed from the interior and incorporated into the atmosphere. The dense silica polymorphs in the mantle could then store a large amount of H_2O in their crystal structures.

the mineralogy of planets hosted around these stars would be dominated by carbides (Kuchner and Seager, 2005; Bond *et al.*, 2010; Madhusudhan *et al.*, 2011b; Fortney, 2012; Petigura and Marcy, 2011; Duffy *et al.*, 2015). Therefore, a planet formed under these conditions could have an exotic internal structure and dynamics compared with the planet types observed in the solar system. Sleep (2018) suggests that instead of a rocky crust, carbon-rich planets would form a graphite rind as shown in Figure 6.4. This rind could react with hydrogen or water to form a methane-rich atmosphere. In the mantles of carbon-rich planets, SiC would be the major phase (Larimer, 1975). The core would likely incorporate some carbon as well due to the abundance of carbon in the system and its solubility in iron at high pressure-temperature (Wood, 1993; Nakajima *et al.*, 2009; Mashino *et al.*, 2019).

While there is an inverse relationship between C/O ratios (and consequently carbide abundance) and water abundance (Madhusudhan *et al.*, 2011b; Pekmezci

et al., 2019), carbides and water could exist in the same planetary system in significant quantities depending on the C/O ratio, redox conditions, and proportion of available carbon in the solid phase as discussed in Pekmezci *et al.* (2019). In addition, carbide planets can form at a zone with locally elevated C/O ratios relative to the host star due to inherent disk inhomogeneities (Kuchner and Seager, 2005; Bond *et al.*, 2010). In this case, the C/O ratio of the system would be lower like our solar system and therefore could contain a significant amount of water.

Our experiments show that water can react with SiC and convert it to silica + diamond at high $P{-}T$. Because a similar conversion of SiC by water to silica has also been reported at very low pressure (Yoshimura *et al.*, 1986), the oxidation reaction can likely occur from the shallow depths of the carbide planets. Two cases can be considered for reaction 6.1 at a planetary scale: either existence of water during the formation of carbide planets or the delivery of water rich materials at later stages of carbide planet formation, such as late veneer discussed for the Earth (Dreibus *et al.*, 1987; Morbidelli *et al.*, 2000; Wang and Becker, 2013).

If water is delivered to carbide planets, the impact will produce high pressure and high temperature locally and induce the reaction. In regions of the mantle where water reaches SiC, the reaction shown in eq. 6.1 would produce diamond and silica. In this case, a carbide planet would experience a chemical change from the outside in. This process could cause the surface to be covered with silica, while at sufficiently greater depths diamond and silica would exist together as shown in Figure 6.4. Diamond and stishovite have high viscosity and diamond has extremely high thermal conductivity (Weidner *et al.*, 1982; McSkimin and Andreatch Jr, 1972). Because of the physical properties, it is unlikely that the diamond + silica-rich mantle would have vigorous convection. In the converted planet, the secular cooling would likely be dominated by conduction, differing from Earth-like planets (Unterborn *et al.*, 2014; Nisr *et al.*,

2017b). Water can alter the rheology of mineral phases (Hirth and Kohlstedt, 1996). Therefore, if the silica phase contains a large amount of water in the converted planets (Nisr *et al.*, 2017a, 2020), it could have a different rheology from anhydrous case. Therefore, it is important to address the impact of water on silica's rheology in future studies.

The hydrogen formed in reaction 6.1 at high pressure would be degassed from the interior and incorporated in the atmosphere. At pressures below the stability of diamond, the reaction likely produces methane as shown by Yoshimura *et al.* (1986):

$$SiC + 2H_2O \rightarrow SiO_2 + CH_4. \tag{6.2}$$
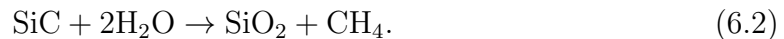
This reaction leads us to believe that at shallower depths and lower temperatures, methane may be produced in hydrated carbon-rich planets. As temperature and pressure increase with depth, it is possible that methane can polymerize to form ethane and higher-order hydrocarbons (Hirai *et al.*, 2009). Therefore, it is feasible that depending on the depths of the chemical alteration by water, the interior of a carbide planet can produce different reducing volatiles (such as methane and hydrogen). If they are degassed and incorporated into the atmosphere, the converted carbon-rich planets would have an even more reduced atmosphere.

It is important to note that stishovite can store a large amount of H_2O in the crystal structure at high pressure. A recent study showed that the solubility in dense silica polymorphs increases with pressure, at least up to 100 GPa, and reaches 8–13 wt% H_2O in silica (Nisr *et al.*, 2020). Therefore, a once-carbide planet that has undergone the conversion from SiC to silicate + diamond could store a large amount of water in its mantle.

An important consideration is how different mineralogy would affect astrophysical observables such as mass, radius, and atmosphere. While the atmospheric com-
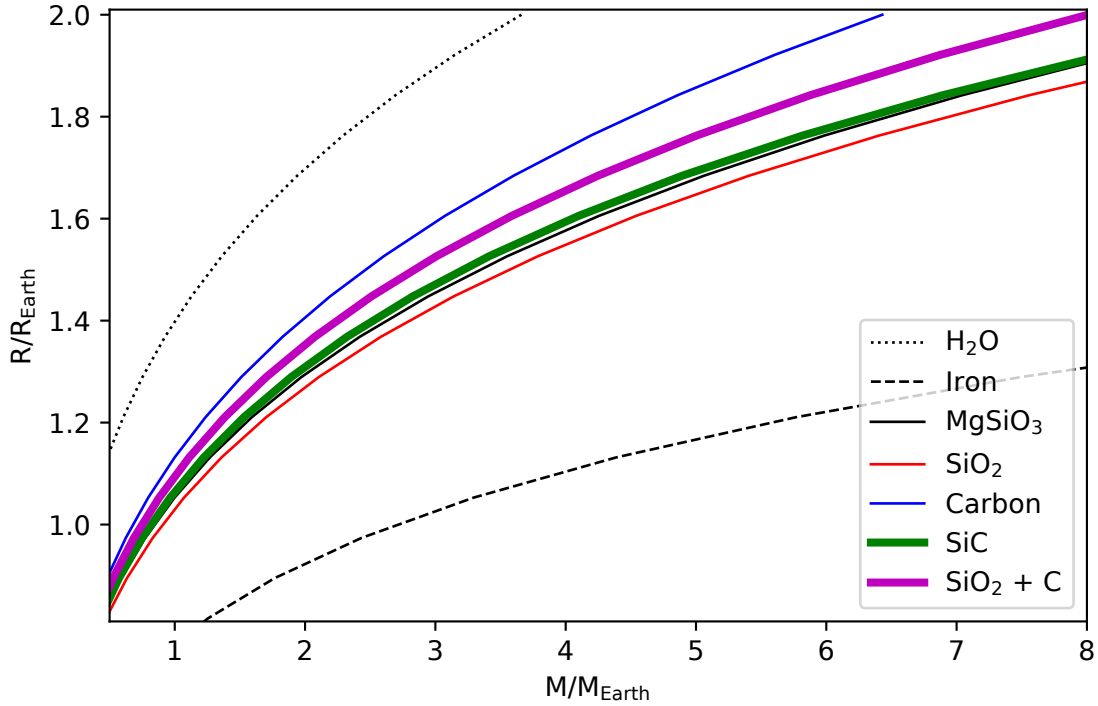
Figure 6.5: Mass-radius relations of planets composed of different materials. A planet composed of SiC (the thick green curve) is indistinguishable from one composed of $MgSiO_3$ (the thin black curve) because of the stability of the dense B1 phase at high pressure. However, a planet composed of diamond + silica (SiO_2 + C; the thick purple curve) would be less dense.

position is already reducing and depleted in water in carbide planets (Madhusudhan *et al.*, 2011a), the chemical reaction presented here would likely push it further in that direction by sequestering oxygen in the mantle and producing carbon- and hydrogen-rich volatile species in the atmosphere during conversion to silicate + diamond planets. As shown in Figure 6.5, a planet composed of SiC would be indistinguishable from a planet composed of magnesium silicates ($MgSiO_3$). The main reason for the similarity is that the dense B1 phase of SiC becomes stable and therefore dominant in the 2–8 Earth mass planets. However, if a carbide planet undergoes alteration by H_2O, the mineralogy would change to SiO_2 + diamond while the bulk chemical composition remains the same. Because of highly incompressible diamond, the converted

carbon-rich planet with diamond and silica would become significantly less dense as shown in Figure 6.5. The difference may not be sufficiently large compared with the level of uncertainties in the existing data for the mass and radius of exoplanets and the degeneracy in the mass–radius parameteral space but the difference in the mass-radius relations combined with the predicted interior–atmosphere relations for the converted carbon-rich planets provide improved constraints for the future investigations for carbon-rich worlds.

Silicon carbide would be the main constituent of carbide planets. However, other elements may exist in the planet. For example, Mg carbides could become important as the Mg/Si ratio increases. Some Mg carbides are known to react with water and form oxides and hydroxides at low pressures (Rueggeberg, 1943; Lauren, 1968; Hájek et al., 1980), similar to the case for Si carbide. Therefore, it is possible that Mg-rich carbides convert to Mg-oxides and diamond, contributing to the conversion of carbide planets. If a carbide planet is large enough to exceed 52–75 GPa in the mantle, SiC will undergo a phase transition (Yoshida et al., 1993; Sekine and Kobayashi, 1997; Daviau and Lee, 2017b; Miozzi et al., 2018; Kidokoro et al., 2017). However, the polymorphic phase transition would likely not make a significant impact on our implications on chemical reactions in the carbon-rich planets, due to the outward-in nature of the transformation (Figure 6.4). Future works on high-pressure polymorphs of SiC with water would address the question of how deep the reaction presented here can occur in carbon-rich planets.

6.6   Conclusion

Combined with the existing experiments at low pressures, our new experiments at high pressures show that water can convert silicon carbide to silica and diamond. With our finding that carbide planets will readily convert to silicate planets in the presence

of water, the number of carbide planets in existence may be even lower than current predictions. Furthermore, a carbide planet could convert to a type of planet which to our knowledge has never been considered before: a planet rich in both diamond and silicates. The unique mineralogy of the converted carbon-rich planets would make the planets un-Earth-like. For example, the mantle of the converted planets would be much more viscous than the Earth-like silicate mantle, because of the physical properties of silica and diamond. Because diamond is a main mineral in those these converted, the secular cooling of the planets could be dominated by conduction from high thermal conductivity of diamond. The atmosphere of the converted planets could be very reducing from the methane and hydrogen degassed from the hydration of the interiors. In contrast, a significant amount of water could remain and be stored in the deep mantle of the converted planet because of the large water storage capacity of dense silica polymorphs at high pressures. During the conversion of a carbon-rich planet, the mineralogy change from carbide to silica + diamond would reduce the density of the planet, because of highly incompressible diamond. Such a conversion would not change the bulk chemical composition significantly. Instead, the mineralogy change alone can shift in the mass-radius relations substantially for the carbon-rich world.

6.7 Acknowledgments

Table 6.1: Experimental runs performed in this study. The temperatures of the LHDAC runs were obtained from the gray-body radiation from the samples except for the DAC13 run. For DAC13 I estimated from the intensity of thermal radiation. The estimated uncertainties for the temperatures are 100–150 K. The estimated uncertainty for pressure is approximately 2–5 GPa. S.M.: starting material, XRD: X-ray diffraction, Raman: micro-Raman spectroscopy, T: temperature, P: pressure or pressure range, t: time duration of heating, and P scale: pressure scale calibrant.

Run	S.M.	t (min)	T (K)	P (GPa)	P scale	Analysis
DAC2	SiC-6H	10	1050–1600	34.5–44.5	Au	XRD
DAC3	SiC-6H	10	1450–1950	39–43.5	Au	XRD
DAC4	SiC-6H	6	1550–1850	41.5–48	Au	XRD
DAC5	SiC-6H	7	1450–2100	42–49	Au	XRD
DAC6	SiC-6H	9	1575–1975	41–47	Au	XRD
DAC7	SiC-6H	4	1700–2675	43–47	Au	XRD
DAC8	SiC-6H	9	1525–2200	42–47	Au	XRD
DAC9	SiC-6H	9	1125–1600	28	Au	XRD
DAC10	SiC-6H	7	1075–1450	26	Au	XRD
DAC11	SiC-6H	7	1150–1600	24.5–28.5	Au	XRD
DAC12	SiC-6H	9	1125–1625	26	Au	XRD
DAC13	SiC-6H	7	1350–1650	28–29	Au	XRD
DAC14	SiC-6H	20	1325–1600	38	Ruby	Raman
DAC15	SiC-6H	20	1275–1675	38	Ruby	Raman
DAC16	SiC-6H	20	1350–1550	38	Ruby	Raman
DAC17	SiC-6H	21	1350-1550	38	Ruby	Raman
DAC18	SiC-3C	15	1400	20	Au	XRD

Chapter 7

CONCLUSION

In this work I have explored various chemical reactions between planetary materials. I have found that under a hydrogen atmosphere:

- Oxidized Fe contained in iron-bearing oxides and silicates is reduced to metal

- Oxidized Si from silicate melts can also be reduced to metal by hydrogen, but this reaction is sensitive to the local water content

- Fe metal alloys with H to form FeH_x where the value of x can exceed 2 at pressures below 10 GPa

- Si metal alloys with Fe but little to no H can exist in these alloys

- The oxygen released by the reduction of Fe and Si reacts with H to form H_2O

- MgO does not react with hydrogen and remains stable at temperatures up to 4200 K

My experimental observations of the phase stability and chemical interactions between Mg, Fe, Si, and O bearing planetary materials (which together make up more than 90% of the rocky planets in our solar system (Morgan and Anders, 1980)) under a hydrogen atmosphere will be of particular value to models of the formation and evolution of large planets with thick H-dominated atmospheres. At the interface between the atmosphere and a silicate magma ocean the reactions presented within this work could drastically alter the mineralogy, structure, and chemical partitioning between the core mantle and atmosphere of a planet. The breakdown of silicates and

oxides will alter the mineralogical makeup of the mantle (enriching it in Mg dominated minerals due to Mg's stability under hydrogen) while removing Fe and Si to the core. The water produced by these reactions could partition to the interior lowering the melting temperature and viscosity of the magma postponing crystallization while convection allows for even greater amounts of ingassing. Water released to the atmosphere may create a long lasting secondary atmosphere (or hydrosphere once the planet cools).

While H_2O can be made from H_2 by the reduction of silicates and oxides, H_2 can be made from H_2O by the oxidation of carbides. In oxygen-poor planetary systems planets may have a far more reduced mineralogy dominated by carbides. If silicon carbide is exposed to water at high temperature (such as by an impact from a water rich object like a comet) they react to form silica (a silicate) and hydrogen. Consider the following two reactions observed in this work:

$$2H_2O + SiC \rightarrow SiO_2 + C + 2H_2 \tag{7.1}$$

$$2H_2 + SiO_2 + Fe \rightarrow 2H_2O + FeSi \tag{7.2}$$

In one, silica and H are produced via reaction with water. In the other, silica is destroyed and water created via reaction with hydrogen. This illustrates the importance of considering the relative quantities volatile species present in planets undergoing diferentiation and equillibration, and the impact the redox conditions they impose may have on the system chemistry. I am excited to see how this work can help inform new models of planet formation and evolution for planets with diverse sizes, structures, and compositions.

REFERENCES

Akimoto, S., T. Yagi and K. Inoue, "High temperature-pressure phase boundaries in silicate systems using in situ x-ray diffraction", in "High-Pressure Research", pp. 585–602 (Elsevier, 1977).

Andrault, D., R. J. Angel, J. L. Mosenfelder and T. Le Bihan, "Equation of state of stishovite to lower mantle pressures", American Mineralogist **88**, 2-3, 301–307 (2003).

Andrault, D., G. Fiquet, F. Guyot and M. Hanfland, "Pressure-induced landau-type transition in stishovite", Science **282**, 5389, 720–724 (1998).

Andrault, D., G. Morard, G. Garbarino, M. Mezouar, M. A. Bouhifd and T. Kawamoto, "Melting behavior of sio 2 up to 120 gpa", Physics and Chemistry of Minerals **47**, 2, 1–9 (2020).

Antonov, V. E., V. M. Gurev, V. I. Kulakov, M. A. Kuzovnikov, I. A. Sholin and V. Y. Zuykova, "Solubility of deuterium and hydrogen in fcc iron at high pressures and temperatures", Physical Review Materials **3**, 11, 113604 (2019).

Badding, J., R. Hemley and H. Mao, "High-pressure chemistry of hydrogen in metals: In situ study of iron hydride", Science **253**, 5018, 421–424 (1991).

Bali, E., A. Audétat and H. Keppler, "Water and hydrogen are immiscible in Earth's mantle", Nature **495**, 7440, 220–222 (2013a).

Bali, E., A. Audétat and H. Keppler, "Water and hydrogen are immiscible in earth's mantle", Nature **495**, 7440, 220–222 (2013b).

Bean, J. L., S. N. Raymond and J. E. Owen, "The nature and origins of sub-neptune size planets", Journal of Geophysical Research: Planets **126**, 1, e2020JE006639 (2021).

Bergh, A., "Atomic hydrogen as a reducing agent", The Bell System Technical Journal **44**, 2, 261–271 (1965).

Birch, F., "Elasticity and constitution of the earth's interior", Journal of Geophysical Research **57**, 2, 227–286 (1952).

Birch, F., "Density and composition of mantle and core", Journal of geophysical research **69**, 20, 4377–4388 (1964).

Boehler, R., "Melting of the fefeo and the fefes systems at high pressure: constraints on core temperatures", Earth and Planetary Science Letters **111**, 2-4, 217–227 (1992).

Boehler, R., N. Von Bargen and A. Chopelas, "Melting, thermal expansion, and phase transitions of iron at high pressures", Journal of Geophysical Research: Solid Earth **95**, B13, 21731–21736 (1990).

Bond, J. C., D. P. O'Brien and D. S. Lauretta, "The compositional diversity of extrasolar terrestrial planets. i. in situ simulations", The Astrophysical Journal **715**, 2, 1050 (2010).

Boppart, H., J. Van Straaten and I. F. Silvera, "Raman spectra of diamond at high pressures", Physical Review B **32**, 2, 1423 (1985).

Bragg, W. H. and W. L. Bragg, "The reflection of x-rays by crystals", Proceedings of the Royal Society of London. Series A, Containing Papers of a Mathematical and Physical Character **88**, 605, 428–438 (1913).

Brett, R., "The current status of speculations on the composition of the core of the earth", Reviews of Geophysics **14**, 3, 375–383 (1976).

Cheng, B., G. Mazzola, C. J. Pickard and M. Ceriotti, "Evidence for supercritical behaviour of high-pressure liquid hydrogen", Nature **585**, 7824, 217–220 (2020).

Cherniak, D. and E. Watson, "Diffusion of helium in olivine at 1 atm and 2.7 gpa", Geochimica et Cosmochimica Acta **84**, 269–279 (2012).

Chipman, J. and S. Marshall, "The Equilibrium $FeO + H_2 = Fe + H_2O$ at Temperatures up to the Melting Point of Iron", Journal of the American Chemical Society **62**, 2, 299–305 (1940).

Copernicus, N., "De revolutionibus orbium coelestium", Norimbergae, Apud J. Petreium (1543).

Cottaar, S., T. Heister, R. Myhill, I. Rose and C. Unterborn, "Burnman v0.9.0", URL `https://doi.org/10.5281/zenodo.546210` (2016).

Daly, R. A., "Origin of the moon and its topography", Proceedings of the American Philosophical Society **90**, 2, 104–119 (1946).

Daviau, K. and K. K. Lee, "Decomposition of silicon carbide at high pressures and temperatures", Physical Review B **96**, 17, 174102 (2017a).

Daviau, K. and K. K. Lee, "Zinc-blende to rocksalt transition in SiC in a laser-heated diamond-anvil cell", Physical Review B **95**, 13, 134108 (2017b).

Daviau, K., Y. Meng and K. K. Lee, "SiO_2 – SiC mixtures at high pressures and temperatures: Implications for planetary bodies containing sic", Journal of Geophysical Research: Planets **0**, ja (2019).

Deemyad, S., E. Sterer, C. Barthel, S. Rekhi, J. Tempere and I. F. Silvera, "Pulsed laser heating and temperature determination in a diamond anvil cell", Review of scientific instruments **76**, 12, 125104 (2005).

Dewaele, A., F. Datchi, P. Loubeyre and M. Mezouar, "High pressure–high temperature equations of state of neon and diamond", Physical Review B **77**, 9, 094106 (2008).

121

Dewaele, A., G. Fiquet, D. Andrault and D. Hausermann, "P-v-t equation of state of periclase from synchrotron radiation measurements", Journal of Geophysical Research: Solid Earth **105**, B2, 2869–2877 (2000).

Dewaele, A., G. Fiquet and P. Gillet, "Temperature and pressure distribution in the laser-heated diamond–anvil cell", Review of scientific instruments **69**, 6, 2421–2426 (1998).

Dewaele, A., P. Loubeyre, F. Occelli, M. Mezouar, P. I. Dorogokupets and M. Torrent, "Quasihydrostatic equation of state of iron above 2 mbar", Physical Review Letters **97**, 21, 215504 (2006).

Dreibus, G., H. Wa *et al.*, "Volatiles on earth and mars: A comparison", Icarus **71**, 2, 225–240 (1987).

Duffy, T., N. Madhusudhan and K. Lee, "2.07 mineralogy of super-earth planets", Treatise on Geophysics p. 149 (2015).

Dziewonski, A. M. and D. L. Anderson, "Preliminary reference earth model", Physics of the earth and planetary interiors **25**, 4, 297–356 (1981).

Errandonea, D., D. Santamaria-Perez, A. Vegas, J. Nuss, M. Jansen, P. Rodríguez-Hernandez and A. Muñoz, "Structural stability of fe 5 si 3 and ni 2 si studied by high-pressure x-ray diffraction and ab initio total-energy calculations", Physical Review B **77**, 9, 094113 (2008).

Fei, Y. and H.-K. Mao, "Static compression of mg (oh) 2 to 78 gpa at high temperature and constraints on the equation of state of fluid h2o", Journal of Geophysical Research: Solid Earth **98**, B7, 11875–11884 (1993).

Fei, Y. and H.-k. Mao, "In situ determination of the nias phase of feo at high pressure and temperature", Science **266**, 5191, 1678–1680 (1994).

Fiquet, G., D. Andrault, J. Itie, P. Gillet and P. Richet, "X-ray diffraction of periclase in a laser-heated diamond-anvil cell", Physics of the Earth and Planetary Interiors **95**, 1-2, 1–17 (1996).

Fischer, R. A., A. J. Campbell, R. Caracas, D. M. Reaman, D. L. Heinz, P. Dera and V. B. Prakapenka, "Equations of state in the fe-fesi system at high pressures and temperatures", Journal of Geophysical Research: Solid Earth **119**, 4, 2810–2827 (2014).

Fortney, J. J., "On the carbon-to-oxygen ratio measurement in nearby sun-like stars: Implications for planet formation and the determination of stellar abundances", The Astrophysical Journal Letters **747**, 2, L27 (2012).

Fu, S., S. Chariton, V. Prakapenka, A. Chizmeshya and S.-H. Shim, "Hydrogen solubility in fesi alloy phases at high pressures and temperatures", American Mineralogist p. in press (2022a).

Fu, S., S. Chariton, V. B. Prakapenka, A. Chizmeshya and S.-H. Shim, "Hydrogen solubility in fesi alloy phases at high pressures and temperatures", American Minerologist **in press** (2022b).

Fu, S., S. Chariton, V. B. Prakapenka, A. Chizmeshya and S.-H. Shim, "Stable hexagonal ternary alloy phase in fe-si-h at 28.6–42.2 gpa and 3000 k", Physical Review B **105**, 10, 104111 (2022c).

Fu, S., J. Yang, Y. Zhang, J. Liu, E. Greenberg, V. B. Prakapenka, T. Okuchi and J.-F. Lin, "Melting behavior of the lower-mantle ferropericlase across the spin crossover: Implication for the ultra-low velocity zones at the lowermost mantle", Earth and Planetary Science Letters **503**, 1–9 (2018).

Fukai, Y. and S.-I. Akimoto, "Hydrogen in the earth's core experimental approach", Proceedings of the Japan Academy, Series B **59**, 6, 158–162 (1983).

Fulton, B. J. and E. A. Petigura, "The california-kepler survey. vii. precise planet radii leveraging gaia dr2 reveal the stellar mass dependence of the planet radius gap", The Astronomical Journal **156**, 6, 264 (2018).

Fulton, B. J., E. A. Petigura, A. W. Howard, H. Isaacson, G. W. Marcy, P. A. Cargile, L. Hebb, L. M. Weiss, J. A. Johnson, T. D. Morton *et al.*, "The california-kepler survey. iii. a gap in the radius distribution of small planets", The Astronomical Journal **154**, 3, 109 (2017).

Futera, Z., X. Yong, Y. Pan, S. T. John and N. J. English, "Formation and properties of water from quartz and hydrogen at high pressure and temperature", Earth and Planetary Science Letters **461**, 54–60 (2017).

Gabriel, T. S. and H. Allen-Sutter, "Dependencies of mantle shock heating in pairwise accretion", The Astrophysical Journal Letters **915**, 2, L32 (2021).

Galilei, G., *Sidereus Nuncius* (Thomas Baglioni, 1610).

Genda, H. and M. Ikoma, "Origin of the ocean on the earth: early evolution of water d/h in a hydrogen-rich atmosphere", Icarus **194**, 1, 42–52 (2008).

Gilbert, F. and A. M. Dziewonski, "An application of normal mode theory to the retrieval of structural parameters and source mechanisms from seismic spectra", Philosophical Transactions of the Royal Society of London. Series A, Mathematical and Physical Sciences **278**, 1280, 187–269 (1975).

Goldreich, P., Y. Lithwick and R. Sari, "Planet formation by coagulation: A focus on uranus and neptune", Annu. Rev. Astron. Astrophys. **42**, 549–601 (2004).

Goncharov, A. F., J. C. Crowhurst, J. K. Dewhurst, S. Sharma, C. Sanloup, E. Gregoryanz, N. Guignot and M. Mezouar, "Thermal equation of state of cubic boron nitride: Implications for a high-temperature pressure scale", Physical Review B **75**, 22, 224114 (2007).

Goncharov, A. F., N. Goldman, L. E. Fried, J. C. Crowhurst, I.-F. W. Kuo, C. J. Mundy and J. M. Zaug, "Dynamic ionization of water under extreme conditions", Physical review letters **94**, 12, 125508 (2005).

Goncharov, A. F., E. Gregoryanz, R. J. Hemley and H.-k. Mao, "Spectroscopic studies of the vibrational and electronic properties of solid hydrogen to 285 GPa", Proceedings of the National Academy of Sciences **98**, 25, 14234–14237 (2001).

Goncharov, A. F., V. B. Prakapenka, V. V. Struzhkin, I. Kantor, M. L. Rivers and D. A. Dalton, "X-ray diffraction in the pulsed laser heated diamond anvil cell", Review of Scientific Instruments **81**, 11, 113902 (2010).

Gregoryanz, E., A. F. Goncharov, K. Matsuishi, H.-k. Mao and R. J. Hemley, "Raman spectroscopy of hot dense hydrogen", Physical Review Letters **90**, 17, 175701 (2003).

Grocholski, B., S.-H. Shim and V. Prakapenka, "Stability, metastability, and elastic properties of a dense silica polymorph, seifertite", Journal of Geophysical Research: Solid Earth **118**, 9, 4745–4757 (2013).

Haisch Jr, K. E., E. A. Lada and C. J. Lada, "Disk frequencies and lifetimes in young clusters", The Astrophysical Journal Letters **553**, 2, L153 (2001).

Hájek, B., P. Karen and V. Brožek, "Hydrolysis of magnesium sesquicarbide Mg_2C_3", Collection of Czechoslovak Chemical Communications **45**, 12, 3408–3416 (1980).

Hakim, K., R. Spaargaren, D. S. Grewal, A. Rohrbach, J. Berndt, C. Dominik and W. van Westrenen, "Mineralogy, structure, and habitability of carbon-enriched rocky exoplanets: A laboratory approach", Astrobiology **19**, 7, 867–884 (2019).

Hakim, K., W. Van Westrenen and C. Dominik, "Capturing the oxidation of silicon carbide in rocky exoplanetary interiors", Astronomy & Astrophysics **618**, L6 (2018).

Hallis, L. J., G. R. Huss, K. Nagashima, G. J. Taylor, S. A. Halldórsson, D. R. Hilton, M. J. Mottl and K. J. Meech, "Evidence for primordial water in earth's deep mantle", Science **350**, 6262, 795–797 (2015).

Hartmann, W. K. and D. R. Davis, "Satellite-sized planetesimals and lunar origin", Icarus **24**, 4, 504–515 (1975).

Hayashi, S. and Y. Iguchi, "Hydrogen reduction of liquid iron oxide fines in gas-conveyed systems", ISIJ international **34**, 7, 555–561 (1994).

Hemley, R., A. Jephcoat, H. Mao, C. Zha, L. Finger and D. Cox, "Static compression of h2o-ice to 128 gpa (1.28 mbar)", Nature **330**, 6150, 737–740 (1987).

Hirai, H., K. Konagai, T. Kawamura, Y. Yamamoto and T. Yagi, "Polymerization and diamond formation from melting methane and their implications in ice layer of giant planets", Physics of the Earth and Planetary Interiors **174**, 1-4, 242–246 (2009).

Hirao, N., T. Kondo, E. Ohtani, K. Takemura and T. Kikegawa, "Compression of iron hydride to 80 gpa and hydrogen in the earth's inner core", Geophysical Research Letters **31**, 6 (2004).

Hirose, K., S. Labrosse and J. Hernlund, "Composition and state of the core", Annual Review of Earth and Planetary Sciences **41**, 657–691 (2013).

Hirose, K., B. Wood and L. Vočadlo, "Light elements in the earth's core", Nature Reviews Earth & Environment **2**, 9, 645–658 (2021).

Hirschmann, M. M., A. Withers, P. Ardia and N. Foley, "Solubility of molecular hydrogen in silicate melts and consequences for volatile evolution of terrestrial planets", Earth and Planetary Science Letters **345**, 38–48 (2012).

Hirth, G. and D. L. Kohlstedt, "Water in the oceanic upper mantle: implications for rheology, melt extraction and the evolution of the lithosphere", Earth and Planetary Science Letters **144**, 1-2, 93–108 (1996).

Holland, T. and S. Redfern, "Unit cell refinement from powder diffraction data: the use of regression diagnostics", Mineralogical Magazine **61**, 404, 65–77 (1997).

Holtgrewe, N., E. Greenberg, C. Prescher, V. B. Prakapenka and A. F. Goncharov, "Advanced integrated optical spectroscopy system for diamond anvil cell studies at gsecars", High Pressure Research **39**, 3, 457–470 (2019).

Hsu, D. C., E. B. Ford, D. Ragozzine and K. Ashby, "Occurrence rates of planets orbiting fgk stars: Combining kepler dr25, gaia dr2, and bayesian inference", The Astronomical Journal **158**, 3, 109 (2019).

Hydrargyrum, "File:bragg diffraction 2.svg", URL \url{https://commons.wikimedia.org/wiki/File:Bragg_diffraction_2.svg} (2011).

Ikoma, M. and H. Genda, "Constraints on the mass of a habitable planet with water of nebular origin", The Astrophysical Journal **648**, 1, 696 (2006).

Jain, A., S. P. Ong, G. Hautier, W. Chen, W. D. Richards, S. Dacek, S. Cholia, D. Gunter, D. Skinner, G. Ceder and K. a. Persson, "The Materials Project: A materials genome approach to accelerating materials innovation", APL Materials **1**, 1, 011002, URL http://link.aip.org/link/AMPADS/v1/i1/p011002/s1\&Agg=doi (2013).

Jamieson, J. C., A. Lawson and N. Nachtrieb, "New device for obtaining x-ray diffraction patterns from substances exposed to high pressure", Review of Scientific instruments **30**, 11, 1016–1019 (1959).

Jayaraman, A., "Diamond anvil cell and high-pressure physical investigations", Reviews of Modern Physics **55**, 1, 65 (1983).

Jayawardhana, R., J. Coffey, A. Scholz, A. Brandeker and M. H. van Kerkwijk, "Accretion disks around young stars: Lifetimes, disk locking, and variability", The Astrophysical Journal **648**, 2, 1206 (2006).

Jeanloz, R., "Properties of iron at high pressures and the state of the core", Journal of Geophysical Research: Solid Earth **84**, B11, 6059–6069 (1979).

Karato, S.-i. and P. Wu, "Rheology of the upper mantle: A synthesis", Science **260**, 5109, 771–778 (1993).

Kidokoro, Y., K. Umemoto, K. Hirose and Y. Ohishi, "Phase transition in SiC from zinc-blende to rock-salt structure and implications for carbon-rich extrasolar planets", American Mineralogist **102**, 11, 2230–2234, URL https://doi.org/10.2138/am-2017-6033 (2017).

Kim, T., S. Chariton, V. Prakapenka, A. Pakhomova, H.-P. Liermann, Z. Liu, S. Speziale, S.-H. Shim and Y. Lee, "Atomic-scale mixing between mgo and h 2 o in the deep interiors of water-rich planets", Nature Astronomy pp. 1–7 (2021).

Kimura, T., H. Ohfuji, M. Nishi and T. Irifune, "Melting temperatures of mgo under high pressure by micro-texture analysis", Nature communications **8**, 1, 1–7 (2017).

Kite, E. S., B. Fegley Jr, L. Schaefer and E. B. Ford, "Superabundance of exoplanet sub-neptunes explained by fugacity crisis", The Astrophysical Journal Letters **887**, 2, L33 (2019).

Kite, E. S., B. Fegley Jr, L. Schaefer and E. B. Ford, "Atmosphere origins for exoplanet sub-neptunes", The Astrophysical Journal **891**, 2, 111 (2020).

Kite, E. S. and E. B. Ford, "Habitability of exoplanet waterworlds", The Astrophysical Journal **864**, 1, 75 (2018).

Kite, E. S. and L. Schaefer, "Water on hot rocky exoplanets", The Astrophysical Journal Letters **909**, 2, L22 (2021).

Kleine, T., C. Münker, K. Mezger and H. Palme, "Rapid accretion and early core formation on asteroids and the terrestrial planets from hf–w chronometry", Nature **418**, 6901, 952–955 (2002).

Kobayashi, Y., T. Kondo, E. Ohtani, N. Hirao, N. Miyajima, T. Yagi, T. Nagase and T. Kikegawa, "Fe-mg partitioning between (mg, fe) sio3 post-perovskite, perovskite, and magnesiowüstite in the earth's lower mantle", Geophysical Research Letters **32**, 19 (2005).

Kohlhaas, R., P. Dunner and S. N, "Über die temperaturabhängigkeit der gitterparameter von eisen kobalt und nickel im bereich hoher temperaturen", Zeitschrift fur Angewandte Physik **23**, 4, 245 (1967).

Kronig, R., J. De Boer and J. Korringa, "On the internal constitution of the earth", Physica **12**, 5, 245–256 (1946).

Kuchner, M. J. and S. Seager, "Extrasolar carbon planets", arXiv preprint astro-ph/0504214 (2005).

Kumari, L., W. Li, C. H. Vannoy, R. M. Leblanc and D. Wang, "Synthesis, characterization and optical properties of mg (oh) 2 micro-/nanostructure and its conversion to mgo", Ceramics International **35**, 8, 3355–3364 (2009).

Lambrechts, M. and A. Johansen, "Rapid growth of gas-giant cores by pebble accretion", Astronomy & Astrophysics **544**, A32 (2012).

Lammer, H., J. Bredehöft, A. Coustenis, M. Khodachenko, L. Kaltenegger, O. Grasset, D. Prieur, F. Raulin, P. Ehrenfreund, M. Yamauchi *et al.*, "What makes a planet habitable?", The Astronomy and Astrophysics Review **17**, 2, 181–249 (2009).

Larimer, J. W., "The effect of C/O ratio on the condensation of planetary material", Geochimica et Cosmochimica Acta **39**, 3, 389–392 (1975).

Larson, A. C. and R. B. Von Dreele, "Gsas", Report lAUR pp. 86–748 (1994).

Lauren, P. M., "A novel synthesis of magnesium carbide", Journal of Chemical Education **45**, 7, A569 (1968).

Lee, D.-C. and A. N. Halliday, "Hafnium–tungsten chronometry and the timing of terrestrial core formation", Nature **378**, 6559, 771–774 (1995).

Lehmann, I., "P"', Publications du Bureau Central Séismologique International. A14 (3): 87–115. **A14**, 3, 87–115 (1936).

Li, C., A. Ingersoll, S. Bolton, S. Levin, M. Janssen, S. Atreya, J. Lunine, P. Steffes, S. Brown, T. Guillot *et al.*, "The water abundance in jupiter's equatorial zone", Nature Astronomy pp. 1–8 (2020a).

Li, Y., L. Vočadlo, T. Sun and J. P. Brodholt, "The earth's core as a reservoir of water", Nature Geoscience pp. 1–6 (2020b).

Lichtenberg, T., "Redox hysteresis of super-earth exoplanets from magma ocean circulation", The Astrophysical Journal Letters **914**, 1, L4 (2021).

Lin, J.-F., E. Gregoryanz, V. V. Struzhkin, M. Somayazulu, H.-k. Mao and R. J. Hemley, "Melting behavior of h2o at high pressures and temperatures", Geophysical research letters **32**, 11 (2005).

Lin, J.-F., D. L. Heinz, A. J. Campbell, J. M. Devine and G. Shen, "Iron-silicon alloy in earth's core?", Science **295**, 5553, 313–315 (2002).

Lissauer, J. J., "Timescales for planetary accretion and the structure of the protoplanetary disk", Icarus **69**, 2, 249–265 (1987).

Lissauer, J. J., "Planet formation", Annual review of astronomy and astrophysics **31**, 1, 129–172 (1993).

Litasov, K. and E. Ohtani, "Phase relations and melt compositions in CMAS–pyrolite–H_2O system up to 25 GPa", Physics of the Earth and Planetary Interiors **134**, 1-2, 105–127 (2002).

Lowell, P., *Mars* (Houghton, Mittlin, 1895).

Luidold, S. and H. Antrekowitsch, "Hydrogen as a reducing agent: Thermodynamic possibilities", Jom **59**, 10, 58–62 (2007).

Madhusudhan, N., J. Harrington, K. B. Stevenson, S. Nymeyer, C. J. Campo, P. J. Wheatley, D. Deming, J. Blecic, R. A. Hardy, N. B. Lust *et al.*, "A high c/o ratio and weak thermal inversion in the atmosphere of exoplanet wasp-12b", Nature **469**, 7328, 64–67 (2011a).

Madhusudhan, N., O. Mousis, T. V. Johnson and J. I. Lunine, "Carbon-rich giant planets: Atmospheric chemistry, thermal inversions, spectra, and formation conditions", The Astrophysical Journal **743**, 2, 191 (2011b).

Mao, H. and P. Bell, "Equations of state of mgo and ε fe under static pressure conditions", Journal of Geophysical Research: Solid Earth **84**, B9, 4533–4536 (1979).

Mao, H., R. Hemley, Y. Fei, J. Shu, L. Chen, A. Jephcoat, Y. Wu and W. Bassett, "Effect of pressure, temperature, and composition on lattice parameters and density of (fe, mg) sio3-perovskites to 30 gpa", Journal of Geophysical Research: Solid Earth **96**, B5, 8069–8079 (1991).

Mao, H., Y. Wu, L. Chen, J. Shu and A. P. Jephcoat, "Static compression of iron to 300 gpa and fe0. 8ni0. 2 alloy to 260 gpa: Implications for composition of the core", Journal of Geophysical Research: Solid Earth **95**, B13, 21737–21742 (1990).

Mao, Z., J.-F. Lin, J. Yang, T. Inoue and V. B. Prakapenka, "Effects of the fe3+ spin transition on the equation of state of bridgmanite", Geophysical Research Letters **42**, 11, 4335–4342 (2015).

Marchi, C. S. and B. P. Somerday, "Effects of high-pressure gaseous hydrogen on structural metals", SAE Transactions **116**, 94–109, URL `http://www.jstor.org/stable/44723846` (2007).

Mashino, I., F. Miozzi, K. Hirose, G. Morard and R. Sinmyo, "Melting experiments on the Fe–C binary system up to 255 GPa: Constraints on the carbon content in the earth's core", Earth and Planetary Science Letters **515**, 135–144 (2019).

McGuire, C., D. Santamaria-Pérez, A. Makhluf and A. Kavner, "Isothermal equation of state and phase stability of fe5si3 up to 96 gpa and 3000 k", Journal of Geophysical Research: Solid Earth **122**, 6, 4328–4335 (2017).

McKenzie, D. P., J. M. Roberts and N. O. Weiss, "Convection in the earth's mantle: towards a numerical simulation", Journal of Fluid Mechanics **62**, 3, 465–538 (1974).

McSkimin, H. and P. Andreatch Jr, "Elastic moduli of diamond as a function of pressure and temperature", Journal of Applied Physics **43**, 7, 2944–2948 (1972).

Millot, M., F. Coppari, J. R. Rygg, A. Correa Barrios, S. Hamel, D. C. Swift and J. H. Eggert, "Nanosecond X-ray diffraction of shock-compressed superionic water ice", Nature **569**, 7755, 251–255 (2019).

Miozzi, F., G. Morard, D. Antonangeli, A. Clark, M. Mezouar, C. Dorn, A. Rozel and G. Fiquet, "Equation of state of SiC at extreme conditions: New insight into the interior of carbon-rich exoplanets", Journal of Geophysical Research: Planets **123**, 9, 2295–2309 (2018).

Moore, G., T. Vennemann and I. Carmichael, "Solubility of water in magmas to 2 kbar", Geology **23**, 12, 1099–1102 (1995).

Morbidelli, A., J. Chambers, J. Lunine, J.-M. Petit, F. Robert, G. Valsecchi and K. Cyr, "Source regions and timescales for the delivery of water to the earth", Meteoritics & Planetary Science **35**, 6, 1309–1320 (2000).

Morbidelli, A., J. I. Lunine, D. P. O'Brien, S. N. Raymond and K. J. Walsh, "Building terrestrial planets", Annual Review of Earth and Planetary Sciences **40**, 251–275 (2012).

Mordasini, C., P. Mollière, K.-M. Dittkrist, S. Jin and Y. Alibert, "Global models of planet formation and evolution", International Journal of Astrobiology **14**, 2, 201–232 (2015).

Morgan, J. W. and E. Anders, "Chemical composition of earth, venus, and mercury", Proceedings of the National Academy of Sciences **77**, 12, 6973–6977 (1980).

Mosenfelder, J. L., P. D. Asimow and T. J. Ahrens, "Thermodynamic properties of mg2sio4 liquid at ultra-high pressures from shock measurements to 200 gpa on forsterite and wadsleyite", Journal of Geophysical Research: Solid Earth **112**, B6 (2007).

Moxfyre, "File:raman energy levels.svg", URL \url{https://en.wikipedia.org/wiki/File:Raman_energy_levels.svg} (2009).

Muso, "File:edx-scheme.svg", URL \url{https://commons.wikimedia.org/wiki/File:EDX-scheme.svg} (2007).

Nakajima, Y., D. J. Frost and D. C. Rubie, "Ferrous iron partitioning between magnesium silicate perovskite and ferropericlase and the composition of perovskite in the earth's lower mantle", Journal of Geophysical Research: Solid Earth **117**, B8 (2012).

Nakajima, Y., E. Takahashi, T. Suzuki and K.-i. Funakoshi, ""carbon in the core" revisited", Physics of the Earth and Planetary Interiors **174**, 1-4, 202–211 (2009).

Narygina, O., L. Dubrovinsky, H. Samuel, C. McCammon, I. Y. Kantor, K. Glazyrin, S. Pascarelli, G. Aquilanti and V. Prakapenka, "Chemically homogeneous spin transition zone in earth's lower mantle", Physics of the Earth and Planetary Interiors **185**, 3-4, 107–111 (2011a).

Narygina, O., L. S. Dubrovinsky, C. A. McCammon, A. Kurnosov, I. Y. Kantor, V. B. Prakapenka and N. A. Dubrovinskaia, "X-ray diffraction and mössbauer spectroscopy study of fcc iron hydride feh at high pressures and implications for

the composition of the earth's core", Earth and Planetary Science Letters **307**, 3-4, 409–414 (2011b).

NASA Exoplanet Archive, "Confirmed planets table", (2019).

Nisr, C., H. Chen, K. Leinenweber, A. Chizmeshya, V. B. Prakapenka, C. Prescher, S. N. Tkachev, Y. Meng, Z. Liu and S.-H. Shim, "Large h2o solubility in dense silica and its implications for the interiors of water-rich planets", Proceedings of the National Academy of Sciences **117**, 18, 9747–9754 (2020).

Nisr, C., K. Leinenweber, V. Prakapenka, C. Prescher, S. Tkachev and S.-H. D. Shim, "Phase transition and equation of state of dense hydrous silica up to 63 gpa", Journal of Geophysical Research: Solid Earth **122**, 9, 6972–6983 (2017a).

Nisr, C., Y. Meng, A. MacDowell, J. Yan, V. Prakapenka and S.-H. Shim, "Thermal expansion of SiC at high pressure-temperature and implications for thermal convection in the deep interiors of carbide exoplanets", Journal of Geophysical Research: Planets **122**, 1, 124–133 (2017b).

Nisr, C., S.-H. Shim, K. Leinenweber and A. Chizmeshya, "Raman spectroscopy of water-rich stishovite and dense high-pressure silica up to 55 gpa", American Mineralogist **102**, 11, 2180–2189 (2017c).

Nisr, C., S.-H. Shim, K. Leinenweber and A. Chizmeshya, "Raman spectroscopy of water-rich stishovite and dense high-pressure silica up to 55 GPa", American Mineralogist **102**, 11, 2180–2189 (2017d).

Nissen, P. E., "The carbon-to-oxygen ratio in stars with planets", Astronomy & Astrophysics **552**, A73 (2013).

Nissen, P. E. and B. Gustafsson, "High-precision stellar abundances of the elements: methods and applications", The Astronomy and Astrophysics Review **26**, 1, 6 (2018).

Ohtani, E., "Melting relation of fe2sio4 up to about 20okbar", Journal of Physics of the Earth **27**, 3, 189–208 (1979).

Okuchi, T., "Hydrogen partitioning into molten iron at high pressure: implications for earth's core", Science **278**, 5344, 1781–1784 (1997).

Oldham, R. D., "The constitution of the interior of the earth, as revealed by earthquakes", Quarterly Journal of the Geological Society **62**, 1-4, 456–475 (1906).

Olson, P. and Z. D. Sharp, "Hydrogen and helium ingassing during terrestrial planet accretion", Earth and Planetary Science Letters **498**, 418–426 (2018).

Ono, S., Y. Ohishi and T. Kikegawa, "High-pressure study of rhombohedral iron oxide, feo, at pressures between 41 and 142 gpa", Journal of Physics: Condensed Matter **19**, 3, 036205 (2007).

Owen, J. E. and Y. Wu, "Kepler planets: a tale of evaporation", The Astrophysical Journal **775**, 2, 105 (2013).

Pekmezci, G., T. Johnson, J. Lunine and O. Mousis, "A statistical approach to planetesimal condensate composition beyond the snowline based on the carbon-to-oxygen ratio", The Astrophysical Journal **887**, 1, 3 (2019).

Pépin, C. M., A. Dewaele, G. Geneste, P. Loubeyre and M. Mezouar, "New iron hydrides under high pressure", Physical review letters **113**, 26, 265504 (2014).

Pépin, C. M., G. Geneste, A. Dewaele, M. Mezouar and P. Loubeyre, "Synthesis of FeH$_5$: A layered structure with atomic hydrogen slabs", Science **357**, 6349, 382–385 (2017).

Petigura, E. A. and G. W. Marcy, "CARBON AND OXYGEN IN NEARBY STARS: KEYS TO PROTOPLANETARY DISK CHEMISTRY", The Astrophysical Journal **735**, 1, 41 (2011).

Piermarini, G. and S. Block, "Ultrahigh pressure diamond-anvil cell and several semiconductor phase transition pressures in relation to the fixed point pressure scale", Review of Scientific Instruments **46**, 8, 973–979 (1975).

Piermarini, G. J., S. Block, J. Barnett and R. Forman, "Calibration of the pressure dependence of the r 1 ruby fluorescence line to 195 kbar", Journal of Applied Physics **46**, 6, 2774–2780 (1975).

Piet, H., A. V. Chizmeshya, B. Chen, S. Chariton, E. Greenberg, V. B. Prakapenka and S.-H. Shim, "Effect of nickel on the high-pressure phases in FeH", Physical Review B **104**, 22, 224106 (2021).

Poirier, J.-P., "Light elements in the earth's outer core: a critical review", Physics of the earth and planetary interiors **85**, 3-4, 319–337 (1994).

Pollack, J. B., O. Hubickyj, P. Bodenheimer, J. J. Lissauer, M. Podolak and Y. Greenzweig, "Formation of the giant planets by concurrent accretion of solids and gas", icarus **124**, 1, 62–85 (1996).

Prakapenka, V., A. Kubo, A. Kuznetsov, A. Laskin, O. Shkurikhin, P. Dera, M. Rivers and S. Sutton, "Advanced flat top laser heating system for high pressure research at GSECARS: application to the melting behavior of germanium", High Pressure Research **28**, 3, 225–235 (2008).

Prakapenka, V. B., N. Holtgrewe, S. S. Lobanov and A. F. Goncharov, "Structure and properties of two superionic ice phases", Nature Physics **17**, 11, 1233–1238 (2021).

Prescher, C. and V. B. Prakapenka, "Dioptas: a program for reduction of two-dimensional x-ray diffraction data and data exploration", High Pressure Research **35**, 3, 223–230 (2015).

Richter, M. J., D. T. Jaffe, G. A. Blake and J. H. Lacy, "Looking for pure rotational h2 emission from protoplanetary disks", The Astrophysical Journal **572**, 2, L161 (2002).

Ringwood, A., "Composition of the core and implications for origin of the earth", Geochemical Journal **11**, 3, 111–135 (1977).

Ringwood, A. E., "Chemical evolution of the terrestrial planets", Geochimica et Cosmochimica Acta **30**, 1, 41–104 (1966).

Rogers, J. G. and J. E. Owen, "Unveiling the planet population at birth", Monthly Notices of the Royal Astronomical Society **503**, 1, 1526–1542 (2021).

Rogers, L. A., P. Bodenheimer, J. J. Lissauer and S. Seager, "Formation and structure of low-density exo-neptunes", The Astrophysical Journal **738**, 1, 59 (2011).

Rotter, C. A. and C. S. Smith, "Ultrasonic equation of state of iron: I. low pressure, room temperature", J. Phys. Chem. Solids **27**, 267-276, 197 (1966).

Rubie, D., F. Nimmo and H. Melosh, "Formation of earth's core", Evolution of the Earth **9**, 51–90 (2007).

Rubie, D. C., D. J. Frost, U. Mann, Y. Asahara, F. Nimmo, K. Tsuno, P. Kegler, A. Holzheid and H. Palme, "Heterogeneous accretion, composition and core–mantle differentiation of the earth", Earth and Planetary Science Letters **301**, 1-2, 31–42 (2011).

Rueggeberg, W. H., "The carbides of magnesium", Journal of the American Chemical Society **65**, 4, 602–607 (1943).

Sabat, K. C., P. Rajput, R. K. Paramguru, B. Bhoi and B. K. Mishra, "Reduction of Oxide Minerals by Hydrogen Plasma: An Overview", Plasma Chemistry and Plasma Processing **34**, 1, 1–23 (2014).

Sakamaki, K., E. Takahashi, Y. Nakajima, Y. Nishihara, K. Funakoshi, T. Suzuki and Y. Fukai, "Melting phase relation of fehx up to 20 gpa: Implication for the temperature of the earth's core", Physics of the Earth and Planetary Interiors **174**, 1-4, 192–201 (2009a).

Sakamaki, K., E. Takahashi, Y. Nakajima, Y. Nishihara, K. Funakoshi, T. Suzuki and Y. Fukai, "Melting phase relation of fehx up to 20 gpa: Implication for the temperature of the earth's core", Physics of the Earth and Planetary Interiors **174**, 1-4, 192–201 (2009b).

Schiaparelli, G. V., *Astronomical and physical observations on the rotation axis and on the topography of the planet Mars made in the Reale specola di Brera in Milan with the equatorial of Merz during the opposition of 1877*, vol. 1 (With Salviucci's Types, 1878).

Schlichting, H. E., "Formation of close in super-earths and mini-neptunes: Required disk masses and their implications", The Astrophysical Journal Letters **795**, 1, L15 (2014).

Schwager, B. and R. Boehler, "H_2O: Another ice phase and its melting curve", High Pressure Research, v.28, 431-433 (2008) **28** (2008).

Sekine, T. and T. Kobayashi, "Shock compression of 6H polytype SiC to 160 GPa", Physical Review B **55**, 13, 8034 (1997).

Shen, G. and P. Lazor, "Melting of minerals under the lower mantle conditions: experimental results", J. Geophys. Res **100**, 17699–17713 (1995).

Shen, G., H.-k. Mao, R. J. Hemley, T. S. Duffy and M. L. Rivers, "Melting and crystal structure of iron at high pressures and temperatures", Geophysical Research Letters **25**, 3, 373–376 (1998).

Shim, S.-H., "Pytheos - a python tool set for equations of state", (2018).

Shim, S.-H., "Peakpo - a python software for x-ray diffraction analysis at high pressure and high temperature", (2019).

Shinozaki, A., H. Hirai, H. Kagi, T. Kondo, T. Okada, D. Nishio-Hamane, S.-i. Machida, T. Irifune, T. Kikegawa and T. Yagi, "Reaction of forsterite with hydrogen molecules at high pressure and temperature", Physics and Chemistry of Minerals **39**, 2, 123–129 (2012).

Shinozaki, A., H. Kagi, N. Noguchi, H. Hirai, H. Ohfuji, T. Okada, S. Nakano and T. Yagi, "Formation of sih4 and h2o by the dissolution of quartz in h2 fluid under high pressure and temperature", American Mineralogist **99**, 7, 1265–1269 (2014).

Siebert, J., A. Corgne and F. J. Ryerson, "Systematics of metal–silicate partitioning for many siderophile elements applied to earth's core formation", Geochimica et Cosmochimica Acta **75**, 6, 1451–1489 (2011).

Sinclair, W. and A. Ringwood, "Single crystal analysis of the structure of stishovite", Nature **272**, 5655, 714–715 (1978).

Sinmyo, R. and K. Hirose, "The soret diffusion in laser-heated diamond-anvil cell", Physics of the Earth and Planetary Interiors **180**, 3-4, 172–178 (2010).

Slater, J. C., "Atomic radii in crystals", The Journal of Chemical Physics **41**, 10, 3199–3204 (1964).

Sleep, N. H., *Planetary Interior-Atmosphere Interaction and Habitability*, pp. 1–22 (Springer International Publishing, Cham, 2018).

Soubiran, F. and B. Militzer, "Miscibility calculations for water and hydrogen in giant planets", The Astrophysical Journal **806**, 2, 228 (2015a).

Soubiran, F. and B. Militzer, "Miscibility calculations for water and hydrogen in giant planets", The Astrophysical Journal **806**, 2, 228 (2015b).

Spektor, K., J. Nylen, R. Mathew, M. Edén, E. Stoyanov, A. Navrotsky, K. Leinenweber and U. Häussermann, "Formation of hydrous stishovite from coesite in high-pressure hydrothermal environments", American Mineralogist **101**, 11, 2514–2524 (2016).

Spektor, K., J. Nylen, E. Stoyanov, A. Navrotsky, R. L. Hervig, K. Leinenweber, G. P. Holland and U. Häussermann, "Ultrahydrous stishovite from high-pressure hydrothermal treatment of SiO_2", Proceedings of the National Academy of Sciences **108**, 52, 20918–20922 (2011).

Stähler, S. C., A. Khan, W. B. Banerdt, P. Lognonné, D. Giardini, S. Ceylan, M. Drilleau, A. C. Duran, R. F. Garcia, Q. Huang *et al.*, "Seismic detection of the martian core", Science **373**, 6553, 443–448 (2021).

Stevenson, D., "Hydrogen in the earth's core", Nature **268**, 5616, 130–131 (1977).

Stixrude, L. and C. Lithgow-Bertelloni, "Thermodynamics of mantle minerals-ii. phase equilibria", Geophysical Journal International **184**, 3, 1180–1213 (2011).

Stökl, A., E. Dorfi and H. Lammer, "Hydrodynamic simulations of captured protoatmospheres around Earth-like planets", Astronomy & Astrophysics **576**, A87 (2015).

Stonkutė, E., Y. Chorniy, G. Tautvaišienė, A. Drazdauskas, R. Minkevičiūtė, Š. Mikolaitis, H. Kjeldsen, C. von Essen, E. Pakštienė and V. Bagdonas, "High-resolution spectroscopic study of dwarf stars in the northern sky: Lithium, carbon, and oxygen abundances", The Astronomical Journal **159**, 3, 90 (2020).

Suárez-Andrés, L., G. Israelian, J. G. Hernández, V. Z. Adibekyan, E. D. Mena, N. Santos and S. Sousa, "C/o vs. mg/si ratios in solar type stars: The harps sample", Astronomy & Astrophysics **614**, A84 (2018).

Tagawa, S., N. Sakamoto, K. Hirose, S. Yokoo, J. Hernlund, Y. Ohishi and H. Yurimoto, "Experimental evidence for hydrogen incorporation into earth's core", Nature communications **12**, 1, 1–8 (2021).

Teske, J. K., K. Cunha, V. V. Smith, S. C. Schuler and C. A. Griffith, "C/o ratios of stars with transiting hot jupiter exoplanets", The Astrophysical Journal **788**, 1, 39 (2014).

Tonks, W. B. and H. J. Melosh, "Magma ocean formation due to giant impacts", Journal of Geophysical Research: Planets **98**, E3, 5319–5333 (1993).

Trachenko, K., V. V. Brazhkin and D. Bolmatov, "Dynamic transition of supercritical hydrogen: Defining the boundary between interior and atmosphere in gas giants", Physical Review E **89**, 3, 032126 (2014).

Umemoto, K. and K. Hirose, "Liquid iron-hydrogen alloys at outer core conditions by first-principles calculations", Geophysical Research Letters **42**, 18, 7513–7520 (2015).

Unterborn, C. T., J. E. Kabbes, J. S. Pigott, D. M. Reaman and W. R. Panero, "THE ROLE OF CARBON IN EXTRASOLAR PLANETARY GEODYNAMICS AND HABITABILITY", The Astrophysical Journal **793**, 2, 124 (2014).

Urbain, G., Y. Bottinga and P. Richet, "Viscosity of liquid silica, silicates and alumino-silicates", Geochimica et cosmochimica acta **46**, 6, 1061–1072 (1982).

Utsumi, W., D. J. Weidner and R. C. Liebermann, "Volume measurement of mgo at high pressures and high temperatures", GEOPHYSICAL MONOGRAPH-AMERICAN GEOPHYSICAL UNION **101**, 327–334 (1998).

Valdez, J., *The Snow Cone Diaries: A Philosopher's Guide to the Information Age* (AuthorHouse, 2014).

Van Valkenburg, A., "Visual observations of high pressure transitions", Review of Scientific Instruments **33**, 12, 1462–1462 (1962).

Walter, M., A. Thomson, W. Wang, O. Lord, J. Ross, S. McMahon, M. Baron, E. Melekhova, A. Kleppe and S. Kohn, "The stability of hydrous silicates in earth's lower mantle: Experimental constraints from the systems MgO–SiO_2–H_2O and MgO–Al_2O_3–SiO_2–H_2O", Chemical Geology **418**, 16–29 (2015).

Wang, X. and L. Andrews, "Gold is noble but gold hydride anions are stable", Angewandte Chemie **115**, 42, 5359–5364 (2003).

Wang, Z. and H. Becker, "Ratios of S, Se and Te in the silicate earth require a volatile-rich late veneer", Nature **499**, 7458, 328–331 (2013).

Weidenschilling, S., "The distribution of mass in the planetary system and solar nebula", Astrophysics and Space Science **51**, 1, 153–158 (1977).

Weidner, D. J., J. D. Bass, A. Ringwood and W. Sinclair, "The single-crystal elastic moduli of stishovite", Journal of Geophysical Research: Solid Earth **87**, B6, 4740–4746 (1982).

Williams, C. D. and S. Mukhopadhyay, "Capture of nebular gases during earth's accretion is preserved in deep-mantle neon", Nature **565**, 7737, 78–81 (2019).

Wilson, D. J., B. T. Gänsicke, J. Farihi and D. Koester, "Carbon to oxygen ratios in extrasolar planetesimals", Monthly Notices of the Royal Astronomical Society **459**, 3, 3282–3286 (2016).

Wolszczan, A. and D. A. Frail, "A planetary system around the millisecond pulsar psr1257+ 12", Nature **355**, 6356, 145–147 (1992).

Wood, B. J., "Carbon in the core", Earth and Planetary Science Letters **117**, 3-4, 593–607 (1993).

Wu, J., S. J. Desch, L. Schaefer, L. T. Elkins-Tanton, K. Pahlevan and P. R. Buseck, "Origin of earth's water: chondritic inheritance plus nebular ingassing and storage of hydrogen in the core", Journal of Geophysical Research: Planets **123**, 10, 2691–2712 (2018).

Yagi, T. and T. Hishinuma, "Iron hydride formed by the reaction of iron, silicate, and water: Implications for the light element of the earth's core", Geophysical Research Letters **22**, 14, 1933–1936 (1995).

Yagi, T., T. Suzuki and S.-I. Akimoto, "Static compression of wüstite (fe0. 98o) to 120 gpa", Journal of Geophysical Research: Solid Earth **90**, B10, 8784–8788 (1985).

Ye, Y., V. Prakapenka, Y. Meng and S.-H. Shim, "Intercomparison of the gold, platinum, and MgO pressure scales up to 140 GPa and 2500 K", Journal of Geophysical Research: Solid Earth **122**, 5, 3450–3464 (2017).

Yeganeh-Haeri, A., "Synthesis and re-investigation of the elastic properties of single-crystal magnesium silicate perovskite", Physics of the Earth and Planetary Interiors **87**, 1-2, 111–121 (1994).

Yoshida, M., A. Onodera, M. Ueno, K. Takemura and O. Shimomura, "Pressure-induced phase transition in SiC", Physical Review B **48**, 14, 10587 (1993).

Yoshimura, M., J.-i. Kase and S. Sōmiya, "Oxidation of SiC powder by high-temperature, high-pressure H_2O", Journal of Materials Research **1**, 1, 100–103 (1986).

Young, P. A., S. J. Desch, A. D. Anbar, R. Barnes, N. R. Hinkel, R. Kopparapu, N. Madhusudhan, N. Monga, M. D. Pagano, M. A. Riner *et al.*, "Astrobiological stoichiometry", Astrobiology **14**, 7, 603–626 (2014).

Zigan, F. and R. Rothbauer, "Neutronenbeugungsmessungen am brucit", Neues Jahrbuch für Mineralogie Monatshefte **1967**, 137À143 (1967).